2 (mix)

NASA CR-134387

NAS9-12077
T-638
Line Item No. 7
MA-129T
R-9353

FINAL REPORT

ANALYSIS OF COMBUSTION INSTABILITY IN LIQUID PROPELLANT ENGINES WITH OR WITHOUT ACOUSTIC CAVITIES

June 1974

by

C. L. Oberg, R. C. Kesselring, C. Warner, III & M. D. Schuman

Rocketdyne Division, Rockwell International
6633 Canoga Avenue, Canoga Park, California

Prepared For

National Aeronautics and Space Administration

Lyndon B. Johnson Space Center

Contract NAS9-12077

R. C. Kahl, Technical Monitor

FOREWORD

The technology program described herein was sponsored by the National Aeronautics and Space Administration, Lyndon B. Johnson Space Center, Houston, Texas, under Contract NAS9-12077. The study was conducted during the 15-month period from 29 June 1972 to 28 September 1973. The NASA technical monitor was Mr. R. C. Kahl. At Rocketdyne, Mr. L. P. Combs was program manager and Dr. C. L. Oberg was project engineer.

The literature review, Priem-type stability analysis, and steady-state combustion model analysis were done primarily by Dr. R. C. Kesselring. The NREC model analysis was done by Mr. M. D. Schuman. The generalized cavity analysis was done by Dr. C. Warner III. Overall technical direction was provided by Dr. C. L. Oberg.

ABSTRACT

Analytical studies have been made of the relative combustion stability of various propellant combinations of interest to NASA-JSC when used with hardware configurations representative of current design practices and with or without acoustic cavities. Available literature was reviewed to locate and summarize available experimental results relating to stability. Two combustion instability models, a Priem-type model and a modification of the Northern Research and Engineering (NREC) instability model, were used to predict the variation in engine stability with changes in operating conditions, hardware characteristics or propellant combination, exclusive of acoustic cavity effects. The NREC model was developed for turbojet engines but is applicable to liquid propellant engines. A steady-state combustion model was used to predict the needed input for the instability models. In addition, preliminary development was completed on a new model to predict the influence of an acoustic cavity with specific allowance for the effects the nozzle, steady flow and combustion.

CONTENTS

Introduction and Summary 1
Stability Experience Review 3
Priem Model Instability Analysis 9
  Description of the Model 9
  Steady-State Combustion Model Calculations 16
  Results From Priem-Type Analysis 18
Quasi-Linear Stability Analyses 25
  NREC Instability Model 26
  NREC Model Calculations 33
  Generalized Cavity Damping Model 42
  Integral Equation Formulation 43
  Iterative-Variational Solution Technique 44
  "Least-Squares" Derivation of Eigenvalue Equation 47
  Formulation in Terms of $a_{\ell q}^{(i)}$ 48
  Computer Results 51
Concluding Remarks 61
References 63

Appendix A

Dropsize Correlations 67

Appendix B

Results From Priem-Type Stability Analysis 71

ILLUSTRATIONS

1. Priem-Type Stability Map Showing Effect of $\Delta V'$ 10
2. Priem-Type Stability Map Showing Effect of K_1 Parameter 12
3. Effect of MAP Parameter on Predicted Stability Limits 13
4. Effect of K_2 and K_3 Parameters on Predicted Stability Limits . . . 14
5. Local Stability Index as a Function of Dropsize for $p_c = 125$ psia, $\Delta p_{inj} = 0.2\ p_c$, CR = 2 19
6. Local Stability Index as a Function of Dropsize for $p_c = 125$ psia, $\Delta p_{inj} = 0.2\ p_c$, CR = 2 20
7. Predicted Nozzle Admittance for First Tangential and Longitudinally Coupled Modes 34
8. Predicted Oscillatory Decay Rates Showing the Effect of Droplet Temperature Oscillation 35
9. Predicted Oscillatory Decay Rates for $\overline{D}_F$ = 100 Microns 37
10. Predicted Oscillatory Decay Rates for $\overline{D}_F$ = 400 Microns 38
11. Predicted Stability Limit Amplitudes for R = 2.0 Inches 39
12. Predicted Stability Limit Amplitudes for R = 4.0 Inches 40
13. Predicted Stability Limit Amplitudes for R = 6.0 Inches 41
14. Predicted Cavity Damping Without Combustion or Steady Flow 52
15. Predicted Effects of Uniform Combustion Source on Cavity Damping 55
16. Predicted Effect of Nozzle on Phase Angle of Oscillating Pressure 58

TABLES

1. Summary of Results from Stability Experience Review 4
2. Predicted Effect of Parameter Variations on Stability 23

NOMENCLATURE

ARABIC SYMBOLS

A = specific acoustic admittance of nozzle

A_c = cross-sectional area of chamber

A_p = Priem stability index (critical disturbance amplitude)

A_t = cross-sectional area of nozzle throat

$a_{\ell q}^{(i)}$ = iterative expansion coefficient, defined by Eq. 66

C_D = orifice discharge coefficient

C_d = droplet drag coefficient

C_F = thrust coefficient

C_p = heat capacity--constant pressure

C_v = heat capacity--constant volume

CR = contraction ratio

C_i = NREC combustion coefficients ($i = 1, 2z, 2r, 2\theta, 3, 4, 5, 6$)

c = isentropic sound velocity

c^* = characteristic exhaust velocity

D = chamber diameter; with subscript, droplet diameter

$\overline{D}_f$ = mass median diameter of fuel spray

$\overline{D}_{ox}$ = mass median diameter of oxidizer spray

$\mathscr{D}$ = mass diffusivity

E = energy content used in NREC model

e_s = total internal energy (thermal only) of spray

$\dot{e}_v$ = energy release rate (see Eq. 37)

$\vec{F}$ = force of interaction between spray and gas

F = thrust

F_e = thrust per element

$G(r|r_o)$ = Green's function

$G_N(r|r_o)$ = modified Green's function defined by Eq. 68

g_c = gravitational constant (32.2 lbm-ft/lbf-sec^2)

ΔH_{comb} = heat of combustion

ΔH_{vap} = heat of vaporization

h_o = source coefficient for generalized cavity damping model, Eq. 57

i = $-\sqrt{-1}$

$J_m(\ )$ = Bessel function of first kind and order m

j = $\sqrt{-1}$

$K_{1,2,3}$ = parameters used in Priem-type model, Eq. 4, 5, and 6

k = β/c

k_g = thermal conductivity of gas

L = chamber length

L_s = depth of acoustic cavity

$\mathscr{L}$ = Priem burning rate parameter, Eq. 1

M = Mach number

M_{vap} = defined by Eq. 8

MAP = mass accumulation parameter, Eq. 3

MR = mixture ratio

MW = molecular weight

m = derivative of burning rate, $\Delta\varepsilon/\Delta z$

$\vec{N}$ = unit normal vector directed out of volume

Nu_H = Nusselt number for heat transfer

Nu_M = Nusselt number for mass transfer

$\tilde{\mathscr{P}}$ = oscillatory source term, Eq. 16

Pr = Prandtl number, $\mu C_p/k_g$
p = pressure
$\tilde{p}$ = oscillatory pressure
p_c = steady-state chamber pressure
p_v = vapor pressure
Q = heat release per unit volume from homogeneous reactions
Q_s = heat release per unit volume of chamber from spray combustion
R = gas constant; also, chamber radius
Re = Reynold's number
$\mathcal{R}_{Nu}$ = response factor from Nusselt number, Eq. 48
$\mathcal{R}_s$ = response factor, $\mathcal{R}_s = \mathcal{R}_{Nu} + \mathcal{R}_z$
$\mathcal{R}_z$ = response factor from heat blockage term, Eq. 53
r = radial position
r_w = chamber radius
$\vec{r}$ = position vector
S = area
$S(\vec{r};\tilde{p})$ = source term defined by Eq. 64
T = temperature
T_f = flame temperature
$T_{\ell q,\ell' q'}$ = expansion coefficient defined by Eq. 80
t = time
t_w = Priem wave time, $2\pi R/c$.
u = velocity
$\tilde{u}$ = oscillatory velocity
u_s = spray velocity
V = volume

V_{gas} = axial gas velocity

V_{drops} = axial spray velocity

$\Delta V'$ = Priem parameter, $(V_{gas} - V_{drops})/c$

V_{inj} = liquid injection velocity

$w(r)$ = weight factor, Eq. 77

w_s = mass generation of gas per unit chamber volume from spray combustion

w_{inj} = injected mass flowrate

w_{vap} = mass generation of gas per unit chamber volume from spray combustion

X_F = burned fraction of fuel

X_{OX} = burned fraction of oxidizer

y = specific acoustic admittance, defined by Eq. 59

z = axial coordinate

GREEK SYMBOLS

α = damping coefficient, imarginary part of β

β = complex angular frequency,

γ = heat capacity ratio, C_p/C_v

$\delta(\vec{r}-\vec{r}')$ = Dirac delta function

δ_{ij} = Kronecker delta ($\delta_{ij} = 1$ if $i = j$, $= 0$ if $i \neq j$)

$\delta(\;)$ = variational operator

ε = overall burned fraction of spray

η_N = eigenvalue for closed, rigid walled chamber, Eq. 62

θ = angular coordinate

Λ = normalization factor, Eq. 63

λ = parameter in source distribution, $\lambda = \bar{u}\,\bar{\tau}$

ρ = gas density

ρ_ℓ = spray density, mass per unit chamber volume

$(\rho D)_{dr}$ = density-diameter product for droplet

σ = $(\vec{u}-\vec{u}_s)\ w_s$

τ = NREC delay time

ϕ = complex eigenvalue, $\phi = kr_w = \omega r_w/c + j\alpha r_w/c$; also with subscript, eigenfunction

ω = angular frequency

ω_{inj} = Priem parameter, $\omega_{inj} = \dot{\omega}_{inj}\ m/A_c$

SUPERSCRIPTS

$\bar{\ }$ (overbar) = denotes time average value; also, particular index

$\sim$ = denotes oscillatory quantity

$\rightarrow$ = denotes vector quantity

(i) = denotes i^{th} iteration

$\wedge$ = denotes amplitude of complex quantity

SUBSCRIPTS

o = denotes steady-state value; also, source coordinate

c = denotes chamber condition

d = denotes droplet condition

dr = denotes droplet condition

f = denotes fuel

g = denotes gas

ℓ = axial mode index

N = m, ℓ, q

m = circumferential mode index

q = radial mode index

ox = denotes oxidizer

r = denotes radial components

s = denotes spray parameter

t = denotes throat condition

z = denotes axial component

θ = denotes angular component

INTRODUCTION AND SUMMARY

As requirements for new rocket engines arise, selections of the propellant combination and general hardware configuration to be used are normally required. The selection processes should include an evaluation of the likelihood of encountering combustion instability problems during engine development and the expected difficulty of obtaining adequate stability through the use of instability suppression devices, such as acoustic cavities. In addition, such factors as the applicability of particular stabilization devices, their size requirements, and special difficulties with particular propellants must be considered.

The purpose of the investigation described herein was to analytically predict the relative stability of various propellant combinations of interest to NASA-JSC when used with hardware configurations representative of current design practice and with or without acoustic cavities to improve stability. Originally, consideration was given to propellant combinations of the LOX/hydrocarbon, LOX/amine, and the NTO/amine families. However, because of subsequent diminished interest in the former two families, attention was later concentrated on the NTO/amine family after the program was under way. The investigation included a literature search, to define the known stability-related characteristics, and stability analyses, employing two combustion instability models and a model to describe the effects of the acoustic cavities. The evaluation was done in a manner that was not specific to any particular engine or hardware design but which provides general information necessary to rationally include stability factors in the propellant selection processes for a range of engine applications. In addition, preliminary development was completed of a generalized acoustic cavity model that includes steady flow and combustion effects not considered in the previously developed model.

Early in the program, a thorough, but not exhaustive, review of the literature was made, to locate and summarize available information relating to stability. Information concerning the propellant combinations of interest and, also, similar propellant combinations, along with any special characteristics of the propellants (such as a tendency toward "popping" or to form an explosive adduct), which may affect stability, was sought. The available stability-related data were summarized and related to injector and engine characteristics as well as possible. Although considerable information was obtained, the results suggest a complex interaction between important effects. Probably the results may be best used with the aid of an analytical model to permit separation of diverse effects.

Two combustion instability models were used to predict the variation in engine stability with hardware configuration and propellant combination, exclusive of acoustic cavity effects. One of these was a Priem-type model; this type of instability model has been used extensively at Rocketdyne and elsewhere for many years. The second model, which is applicable to liquid propellant engines but which has been developed for analysis of turbojet engine afterburners, has been called the Northern Research and Engineering Corporation (NREC) model (Ref. 1). The NREC model is based on an analysis of liquid propellant combustion instability by Culick (Ref. 2). In addition, a model for the steady-state combustion was used to provide needed input for these stability models. Results from these stability analyses were used to develop parametric representations, as much as possible, to show the relationship of stability to key parameters (such as dropsize and burning rate). Parametric representations were used to avoid restricting the results to a particular set of injector/chamber conditions and dimensions. Results from the analyses were used to establish the relative stability of the various configurations and to establish stability trends with changes in design parameters.

The Priem-type stability analysis was done for a relatively broad range of conditions and extensive plots have been developed of the variation of the stability index, A_p, with important physical parameters. These plots may be used to a assess the stability of new hardware configurations with minor additional calculations. Calculations were also made to show the effects of varying the choice of analysis parameters. The results show the importance, when performing stability analyses, of the choice of parameters to be held constant. In addition, the results suggest that the propellant mass flux within an engine has a very strong influence on stability. The greatest changes in stability were predicted when (1) chamber pressure was increased by increasing the propellant flow through a fixed set of hardware (worsened stability) or (2) contraction ratio was increased with a fixed thrust (improved stability).

The analysis done with the NREC stability model was less extensive than that done with the Priem-type model. However, the results from the NREC analysis appear to agree in a rough qualitative way with those from the Priem-type analysis. The degree of agreement appears compatible with the major differences in approach that have been used in development of the two models. The NREC model, or similar approaches, appears to be a valuable method of analysis for liquid-propellant engines. The Priem and NREC models complement each other because each includes important factors not included in the other. Further work with the NREC model is recommended.

Also, preliminary development of a model was undertaken to aid in the design of acoustic cavities, which specifically included the effects of the nozzle, combustion, and steady flow. This model was based on a combination of the concepts used in the existing cavity damping model (which does not specifically allow for these effects) and those used in the NREC model. Preliminary development of this model was completed, the effects due to pressure-coupled combustion response (velocity coupling effects remain to be added), nozzle effects, and steady flow (as a uniform approximation), as well as the acoustic cavity being included. The limited computational results obtained thus far show the importance of interactions between the effects of the cavities and those due to the nozzle, combustion, and steady flow, under some circumstances. Because of these interactions, the need to adequately allow for them in cavity design is evident and additional work is recommended.

STABILITY EXPERIENCE REVIEW

Available information relating to combustion instability, particularly concerning the LOX/hydrocarbon, LOX/amine, and N_2O_4/amine and similar propellant combinations has been reviewed to summarize and assess available information. The principal effort involved review of the proceedings from combustion and combustion instability meetings. Although a computerized library search resulted in the acquisition of only a few pertinent references, the review was aided by consultations with informed Rocketdyne personnel.

Results from this review are summarized in Table 1, which shows the combustion stability experience obtained with various propellant combinstions during a number of engine development programs. The references quoted in Table 1 are Ref. 3 through 37. Abbreviations used in Table 1 are defined at the end of the table.

The preponderance of stability experience with LOX/RP-1 has been accumulated at Rocketdyne. This propellant combination was used in the Jupiter, Thor, Atlas, Saturn IB, and Saturn V engine systems. The earliest engine development programs did not inlcude dynamic stability testing (i.e., no stability rating devices were used) but significant testing was done to eliminate spontaneous instabilities. The MB-3 engine, for the Thor vehicle, required an injector face baffle to eliminate spontaneous instabilities. A baffle was also employed in the MA-5 engine used for the Atlas booster (which was essentially identical to the MB-3); also, this was the first LOX/RP-1 engine for which dynamic stability was verified. An identical baffle configuration was employed in the H-1 engine to achieve dynamic stability. Much difficulty was encountered in the development of a dynamically stable F-1 engine. Among these difficulties were the elimination of low-frequency (nonacoustic) instability modes and a high sensitivity of acoustic modes of instability to minor changes in the injector face orifice pattern. In the final version of the F-1 engine, a 13-compartment, 3-inch-long baffle was used on the injector face. The F-1 engine is relatively unique compared to all other engines listed in Table 1, however, because of its large chamber diameter (39.2 inches) and its small contraction ratio (1.25). No more recent stability work was found concerning engines in which the LOX/RP-1 propellant combination was used.

With the exception of a very limited number of tests with LOX/UDMH in a high-pressure, two-dimensional model of the F-1, no experience with LOX/amines was found.

The NTO/amine propellant combinations have been employed extensively in recent years. The majority of applications have been in engines of moderate size (~10-inch diameter). When these propellants have been employed in chambers with diameter greater than 10 inches, dynamic instability problems have invariably occurred. These problems have been solved in a number of cases (GEMSIP, Apollo, SPS, etc.) through the use of injector face baffles. In other cases, such as the 7.79-inch-diameter Lunar Module Ascent engine, acoustic absorbers have been used in addition to (or in place of) injector face baffles to achieve dynamic stability. Moreover, no maximum engine size is evident below which no instability is encountered. For example, instability problems were encountered in very small combustion chambers, viz., the 3-inch-diameter Rocketdyne RS-14 (9000 Hz instability) and the 1.6-inch-diameter Thiokol C-1 (17,000 Hz instability).

TABLE 1. SUMMARY OF RESULTS FROM STABILITY EXPERIENCE REVIEW

Company	Engine	Oxidizer	Fuel	Element Type		Number of Primary Elements	Orifice Diameter, inch		Thrust, pounds	Thrust per Element, lbf	Mixture Ratio	Chamber Pressure, psia	Injection Pressure Drop, psi		Injection Velocity, ft/sec		Injection Temperature, F		General Chamber Configuration	Chamber Diameter, inch	Injector to Throat Distance, inch	Contraction Ratio	η_{c^*}	Baffle	Baffle Length, inch	Number of Blades or Compartments	Acoustic Absorber	Absorber Size	Absorber Fractional Open Area, percent	Pops, etc.	Stability Rating Device	Instability Mode	Undisturbed Stability (No Rating Device)	Dynamic Stability (With Rating Device)	References	Stability Comments and Conclusions
				Oxidizer	Fuel		Oxidizer	Fuel					Oxidizer	Fuel	Oxidizer	Fuel	Oxidizer	Fuel																		
Rocketdyne	Redstone	NTO	UDMH	LD	LD	355 O 355 F	0.113	0.1015	83.6K	118	1.8	332					73	89	Cyl	21.5	34.7	2.0		None			None				None		Stable		3, 4	NTO/UDMH successfully substituted for LOX/75% Alcohol
↓	S3, Jupiter	LOX	RP-1	LD	LD	361 O 361 F	0.113	0.089	150K	208	2.3	530							Cyl	20.9	28	1.6	94.7	None			None				None		↓		4	
↓	S3, Jupiter	NTO	UDMH	LD	LD	361 O 361 F	0.113	0.089	143K-188K	~230	1.8-2.5	542							Cyl	20.9	28	1.6	98.8	None			None				None		↓		3	NTO/UDMH successfully substituted for LOX/RP-1
↓	MB-3, Thor	LOX	RP-1	Trip	LD	335 O 582 F	0.113	0.635	170K	185	2.15	588							Cyl	20.9	28	1.6	95.5	⊛	3	7 cmpt	None				None	1T	↓		5, 6	1T eliminated with baffle
↓	MA-5, Atlas Booster	LOX	RP-1	Trip	LD	335 O 582 F	0.113	0.635	165K	180	2.36	578	91	101	94	114			Cyl	20.9	28	1.6	95.5	⊛	3	7 cmpt	None				Bomb	1T	↓	Stable	5	1T eliminated with baffle
↓	MA-5, Atlas Sustainer	LOX	RP-1	L. Trip	L. Trip	144 O 175 F	0.120	0.935	57K	178	2.4	706	117	63	97	86			Cyl	12.4	28	1.8	96.4	None			None				None	1T	See Note		5	0.1% incidence of undamped 1T mode
↓	S-4, Atlas Sustainer	NTO	UDMH	LD	LD				~60K										Cyl	12.4	28	1.8		None			None				None		Stable		3	These propellant combinations were successfully substituted for LOX/RP-1
↓	↓	NTO	MMH	LD	LD				73.7K		1.48	853						250	Cyl	12.4	28	1.8		None			None				None		↓		3	
↓	↓	NTO	UDMH-50	LD	LD				~60K										Cyl	12.4	28	1.8		None			None				None		↓		3	
↓	MA-5, Atlas Vernier	LOX	RP-1	2 O on 2 F Quadlet		30	0.037	0.032	1K	33	1.8	350	100	55	93	79			Cyl	2.83	8.75	3		None			None				None		↓		5	
↓	H-1, Saturn 1B	LOX	RP-1	Trip	LD	365 O 612 F	0.120	0.082	205K	210	2.34	705	120	81	107	95			Cyl	20.9	31	1.6	97.3	⊛	3	7 cmpt	None				Bomb		↓		5	1T, 2T modes elim. by baffle, dynamically stable with baffle and low fuel injection velocity
↓	E-1	LOX	RP-1	LD	LD				300K		2.4	880							Cyl	21.6	40	1.5		None			None				None	1T	↓		7	Longer chamber (40 inches) stable but shorter (28 inches) chamber unstable
↓	E-1	NTO	UDMH	LD	LD				300K												40			None			None				None		↓		7	Stable in long (40 inches) chamber, but unstable in short (28 inches) chamber. Similar to LOX/RP-1 behavior.
↓	E-1	NTO	UDMH-50	LD	LD				300K												40			None			None				None		Unstable		4	
↓	F-1, Saturn 1C	LOX	RP-1	LD	LD	714 O 702 F	0.242	0.281	1522K	1073	2.27	1128	312	95	132	56	-289	30-105	Cyl	39.2	40	1.25	93.8	◎	3	13 cmpt	None			Pops	Bomb	1T	Stable		5	1T mode elim. with baffle and pattern mods; chug/buzz in transition elim. with low LOX ΔP; harmonics elim. with hot injection
↓	F-1, Saturn 1C	LOX	RP-1	LD	LD	714 O 702 F	0.242	0.281	1522K	1073	2.27	1128	312	95	132	56	-289	30-105	Cyl	39.2	40	1.25		◎	3	13 cmpt	Liner	Full-Length	6	Pops	Bomb	1T	↓		5	Some improvement in damp time
↓	LP2D	LOX	RP-1	LD	LD	17 O 18 F	0.113	0.089	~3K	~86	2.3	450							2D	21.5x1	24	1.6		⊔⊔⊔⊔	2-3	3	None				Bomb		↓	Unstable	8	Spont. stable with three 2- or 3-inch-long baffles, dyn. stable (for many, but not all, bomb sizes) with six 3-inch long baffles
↓	↓	NTO	UDMH	LD	LD	17 O 18 F	0.113	0.089	~3K	~86	2.15	570							2D	21.5x1	24			⊔⊔⊔⊔	2.5	3	None				Bomb	1T			8	Concluded that with same injection and similar operating conditions long baffles required to stabilize NTO/UDMH than LOX-RP-1
↓	↓	NTO	UDMH	LD	LD	17 O 18 F	0.113	0.089	~3K	~86	2.15	570							2D	21.5x1	24			⊔⊔⊔⊔	4	3	None				Bomb			Stable	8	
↓	Annular Chamber	LOX	RP-1	LD	LD				15K		2.3	450							Ann.	12.3 ID 9.4 OD		1.6		⊛	3	6	None				Bomb			↓	8	Concluded that longer baffles required for high usually stable contraction ratio chambers
↓	↓	LOX	RP-1	LD	LD				15K		2.3	750							Ann.	12.3 ID 9.4 OD		3.0		⊛	6	6	None				Bomb			↓	8	
↓	HP2D	LOX	RP-1	Trip	LD	17 O 18 F			~30K	~860		1100							2D	20x1.5	40	1.25		⊔⊔⊔⊔	3	3	None				Bomb			See Note	9	Usually stable
↓	↓	LOX	RP-1	LD	LD	17 O 18 F	0.242	0.281	~30K	~860	2.4	1100							2D	20x1.5	40	1.25		⊔⊔⊔⊔	3	3	None				Bomb			Stable	9	
↓	↓	LOX	UDMH	T/LD	LD	17 O 18 F			~30K	~860	2.1-2.6	1100							2D	20x1.5	40	1.25		Yes			None								11	Concluded RP-1 more stable than UDMH, particularly in the LOX-triplet injector; RP-1 flow damped UDMH instability in one case
↓	LP2D	LOX	RP-1	LD	LD		0.073	0.067	3K		2.3	425							2D	21.5x1	24						None				Press Pulse		Stable		10	For uniplanar injector with short fuel impingement distance, NTO/UDMH spontaneously unstable. For biplanar injector with long fuel imp., ΔP rating was: LOX/RP-1 = 0.92 and NTO/UDMH = 1.00 Concluded NTO/UDMH no more tractable than LOX/RP-1
↓	LP2D	NTO	UDMH	LD	LD		0.073	0.067	3K			425							2D	21.5x1	24						None				Press Pulse		Mixed Results		10	
↓	Barrel	LOX	RP-1	LD	LD		0.055	0.055	12K		2.3	320	255	155					Cyl	21.6	24	18.3					None				↓		Stable		4	ΔP Rating: LOX/RP-1 = 1.00 NTO/UDMH = 0.45 NTO/UDMH = 0.13 Conclude: NTO/UDMH has lower inherent resistance to instability than LOX/RP-1
↓	↓	NTO	UDMH	LD	LD						2.14	320	200	200					Cyl	↓	↓	↓					None				↓		↓		4	
↓	↓	NTO	UDMH	LD	LD						2.55	320	255	155					Cyl	↓	↓	↓					None				↓		↓		4	
↓	Horiz. Test Stand	LOX	UDMH-50						135K															None			None				None		See Note		4	Shutdown triggered instability. Concluded N_2H_4 either with LOX or NTO is far from tractable. UDMH felt to be considerably better.
↓	Horiz. Test Stand	LOX	25 UDMH 75 N_2H_4						135K															None			None				None		Unstable		4	
↓	↓	LOX	N_2H_4						135K															None			None				None		↓		4	
↓	↓	NTO	N_2H_4						135K															None			None				None		↓		4	
↓	SE-6, Gemini Re-entry	NTO	MMH	UD Splashplate	UD	4	0.0225	0.018	23.5	5.8	1.3	150	36	85	49	97			Cyl	0.70		3.7	93.6	None			None				None		Stable		13	
↓	SE-7, Gemini OAMS	NTO	MMH	UD Splashplate	UD	16	0.024	0.018	79	4.9	1.2	137	21	56	35	56			Cyl	1.25	3.74	3.4	87.6	None			None				None		↓		13	
↓	SE-7, Gemini OAMS	NTO	MMH	UD Splashplate	UD	16	0.024	0.018	94.5	5.9	1.2	140	30	45	43	67			Cyl	1.25	4.0	3.1	85.9	None			None				None		↓		13	
↓	SE-8, Apollo RCS	NTO	MMH	UD Splashplate	UD	16	0.026	0.021	93	5.8	2.1	140	40	57	44	52			Cyl	1.25	4.3	3.1	91.9	None			None				None		↓		13	
↓	SE-9, Titan & Transtage	NTO	A-50	UD Splashplate	UD	4	0.024	0.021	25	6.25	1.56	150	31	33	46	60			Cyl	0.70	2.77	4.45		None			None				None		↓		13	
↓	SE-9, Titan & Transtage	NTO	A-50	UD	UD	8	0.024	0.020	45	5.63	1.56	140	25	33	41	62			Cyl	1.06	2.59	5	93.2	None			None				None		↓		13	
↓	SE-10, LM Descent	NTO	A-50	F-O-F Unlike Triplet		165	0.067	0.045	10.5K	63.6	1.6	150	40	40	46	57			Cyl	11.35	15	2.5	97.2	⊛	1.75	3	None			Pops	Bomb		Marginal*	Marginal**	14	*Pops triggered instability which damped **"Almost all" damped
↓	RS-18, LM Ascent	NTO	A-50	F-O-F Unlike Triplet		96	0.0544	0.0326	3.5K	~36.5	1.6	120	31	29	46	57	T_A-40 to T_A+100		Cyl	7.79	11	2.9	96.0	⊛	1.75	3	QWR	0.6 L x 0.1 W	5.2		Bomb		Stable	Stable	5	Originally designed with baffles (1T) and cavities (1R, 3T)

FOLDOUT FRAME 1

FOLDOUT FRAME 2

FOLDOUT FRAME 3

TABLE 1 (Continued)

Company	Engine	Oxidizer	Fuel	Element Type		Number of Primary Elements	Orifice Diameter, inch		Thrust, pounds	Thrust per Element, lbf	Mixture Ratio	Chamber Pressure, psia	Injection Pressure Drop, psi		Injection Velocity, ft/sec		Injection Temperature, F		General Chamber Configuration	Chamber Diameter, inch	Injector to Throat Distance, inch	Contraction Ratio	η_{c^*}	Baffle	Baffle Length, inch	Number of Blades or Compartments	Acoustic Absorber	Absorber Size	Absorber Fractional Open Area, percent	Pops, etc.	Stability Rating Device	Instability Mode	Undisturbed Stability (No Rating Device)	Dynamic Stability (With Rating Device)	References	Stability Comments and Conclusions
				Oxidizer	Fuel		Oxidizer	Fuel					Oxidizer	Fuel	Oxidizer	Fuel	Oxidizer	Fuel																		
Rocketdyne	RS-18, LM Ascent	NTO	A-50	UD	UD	177	0.0504 O 0.0362 I	0.0397 O 0.0319 I	3.5K	19.8	1.6	120	32	31	47	58	T_A-40 to T_A+100		Cyl	7.79	11	2.9	97.1	Ⓨ	1.75	3	QWR	0.6 L x 0.1 W	5.2	Ign. Spikes	Bomb		Stable	Stable	15	Originally designed with baffles (1T) and cavities (1R, 3T)
																									1.75							1R, 3T	Stable	Unstable	15	
																									1.0									Stable	15	Determined marginal baffle length
																									0.75									Unstable	15	
																								None				Var	Var			1T	Stable	Stable	15, 16	Could stabilize with cavity alone; 16 percent open area marginal
	RS-14, PBPS	NTO	MMH	UD	UD	36	0.0270 O 0.0250 I	0.0175 O 0.0205 I	316	8.8	1.60	125	54	47	54	66				3.0	3	4.9	92.1	Tabs 0.5 W	0.6 L					Ign. Spikes	Pulse Mode	1T		Unstable	17	1 to 2 percent incidence rate of instable (3 percent without tabs)
																								Tabs 0.5 W	0.6 L			0.55 L x 0.06 W	7					Stable	17	Completely stable
																								None										Stable	17	Completely stable
	RS-21, Mars Mariner	NTO	MMH	UD	UD	36			3	8.3	1.57	116																			None			Stable*	5	*Assumed stable
Bell	LM-Ascent	NTO	A-50	F-O-F Unlike Triplet		84	0.055	0.033	3.5K	41.7	1.6	120								7.79	11.95	2.9					None			Ign. Spikes		1T	Stable	Unstable	18, 19	
																								See Note*	0.4 to 0.4	See Note*	None			Pops**				Usually Unstable	18, 19	* ⦶⊕ⓎⓎ Not all blades extended to wall; especially unstable with wall gap. **Pops associated with propellant accumulation under baffle
																								Ⓨ	1.25 Y 0.5 O	3						1R, 3T		Unstable	18, 19	Concluded ineffective damping of 1R which triggers 3T
																													~3					?	18, 19	Investigated but dropped
																											Groove in Wall	1/16 x 7/32						Stable	18,19,20	Final injector configuration included groove in wall at chamber periphery to eliminate 3T
	Adv. Agena Mod. Mod. 8533	NTO	A-50	F-O-F Unlike Triplet		88			15-19K		1.8-2.0				56	89	97	322		10.79	10.2	4.9		None			None					1T		Unstable	21	
																								⊕	1-1/4-2	4				Pops*		2T		Marginal	21	1.25 inch long baffle dyn. unstable; 1.5 inch and 1.75 inch baffles resurge; 2 inch long baffle dyn. stable but long damp time. *Associated with accumulation under baffle
																								None			600 Orif Liner		~5		Bomb			Unstable	21	Discontinued effort
																								⊗		5									21, 22	Recommended but program terminated before testing
Aerojet	Titan I Booster	LOX	RP-1	LD	LD	560 O 610 F	0.119		180K	154	2.25	637								21.6		2	97.8	None			None						Stable	Unstable	23	Statistically stable spontaneously
	Titan II, III Gemini, 1st Stage	NTO	A-50	LD	LD	568 O 516 F	0.119	0.082	215K	200	2.0	785							Cyl	21.8	22	1.93	97.2	None			None				Bomb	1T	Stable	Unstable	24, 25	Statistically stable spontaneously, 0.6 percent incidence of instability (during operation in low MR, low P_c region)
	Titan I Sustainer	LOX	RP-1	LD	LD	328 O 392 F	0.085	0.057	80K	111		682								14.2			98.9	None			None						Stable	Unstable	24	Statistically stable spontaneously
	Titan II, III Gemini, 2nd Stage	NTO	A-50	LD	LD				100K	100	1.8	827							Cyl	14.5	21	2.5		None			None				P.G.	1T, 2T	Marginal*	Unstable	25	*1.3 percent incidence of instability
				LD	LD																			⊛	4	8 + Hub	None				Bomb	1L	Unstable*	Unstable	25	*30 percent incidence of instability
				Quadlet			0.049	0.037															97.4	⊛	4	6 + Hub	None				P.G. Bomb	3T	Marginal	Unstable	25	*1.3 percent incidence of instability
	Titan 2nd Stage GEMSIP	NTO	A-50	Quadlet								804												⊛	5*	7	None				P.B. Bomb–			Stable	25, 26	*Marginal length 2.5 inches. Lumped injection at mid-radius
				2-on-2 Unlike Impingement						200														None			None							Unstable	26	
										200			140	140										⊛	5*	7	None							Stable	26	*Marginal length 2.5 inches. Flat distribution; selected concept
	Apollo SPS		UDMH-50	UD	UD				21.5K	30	2.0	100							Cone	17.6	21	2.0		None							Bomb	2T	Stable**	Unstable	25	*Less than 1 percent incidence of instability. **Statistically stable. Injector has varying impingement distances across face
						575				40														⊛	4	6 Unsym. + Hub							Stable	Stable	25	Mixed impingement
							0.041-0.073	0.041-0.077		40														⊛	4	5 + Hub							Stable	Stable	25	Mixed impingement; selected concept
										40	1.6*													⊛	4*	5 + Hub				Pops*				Stable*	27	*Shift in MR from 2.0 to 1.6 resulted in marked increments in incidence of random popping; dyn. stab. was restored by counterboring ox. orifices and increasing baffle length
	Transtage 21-10	NTO		Quadlet		336	0.036	0.0292	8.15K	24	2.0	100			~40	~40	31-73	32-60		11.91	17.72	2.53		⊕	3.2	4	None			Pops		2T	Unstable		25, 27	Pops triggered sustained instability
	Transtage 21-11B	NTO		Alt Rings Quad. & F-O-F Triplet		336	0.036 Q 0.051 T	0.0292	8.15K	24	2.0	100			~40	~45	24-85	57-86		11.91	17.72	2.53	96.1	⊕	3.2	4	None			Pops			Stable	Marginal	25, 27	Flight version
	Transtage 21-11B	NTO		Alt Rings Quad. & F-O-F Triplet		336	0.036 Q 0.051 T	0.0292	8.15K	24	2.0	100			~40	~45	24-85	57-86		11.91	17.72	2.53		None			Yes		5.3/6.5					Unstable/ Stable	5, 24	6.5 percent open area of absorber required for dyn. stability
AFRPL	8 Spud Pulse Motor	NTO	N_2H_4	LD	LD	40 O 18 F	0.0785	0.0785	4.5K		0.9-1.44	300							Cyl	12.8		10.3		None			None				P.G.		Unstable	Unstable	28	
				O-F-O Triplet		20	0.104	0.104																									Unstable		28	
				Like Doublets With O-F-O Fan Trip		78	0.028	0.035																									Unstable		28	
			MMH	LD	LD	40 O 18 F	0.0785	0.0785			1.4-2.3																							Stable	28	*Unstable at low MR. Concluded MMH more stable than N_2H_4. Instability increases with decreasing MR for N_2H_4. Experimental results agreed with predicted stability trends using Priem model
				O-F-O Triplet		20	0.104	0.104																									Unstable	Unstable	28	
				Like Doublets With O-F-O Fan Triplet		78	0.028	0.035																									Unstable		28	

FOLDOUT FRAME 1

FOLDOUT FRAME 2

FOLDOUT FRAME 3

TABLE 1 (Concluded)

Company	Engine	Oxidizer	Fuel	Element Type		Number of Primary Elements	Orifice Diameter, inch		Thrust, pounds	Thrust per Element, lbf	Mixture Ratio	Chamber Pressure, psia	Injection Pressure Drop, psi		Injection Velocity, ft/sec		Injection Temperature, F		General Chamber Configuration	Chamber Diameter, inch	Injector to Throat Distance, inch	Contraction Ratio	η_{c*}	Baffle	Baffle Length, inch	Number of Blades or Compartments	Acoustic Absorber	Absorber Size	Absorber Fractional Open Area, percent	Pops, etc.	Stability Rating Device	Instability Mode	Undisturbed Stability (No Rating Device)	Dynamic Stability (With Rating Device)	References	Stability Comments and Conclusions
				Oxidizer	Fuel		Oxidizer	Fuel					Oxidizer	Fuel	Oxidizer	Fuel	Oxidizer	Fuel																		
AFRPL	8 Spud Pulse Motor	NTO	MMH	LD	LD		0.042 to 0.12	0.039 to 0.113	5K		2.0	300 400 600			40 to 130	30 to 120			Cyl	15		Ø (P_c)	> 85	None			None				P.G.	1T	Stable	Unstable	29	Stability increases with: Inc. P_c, dec. W_T, inc. V_{inj}, inc. $\bar{D}$. This trend agrees with Priem theory predictions
↓	Transtage 21-1D	↓	N_2H_4	Quadlet		336	0.036	0.0292	8.15K	24	1.4-2.6	100			~40	~40	31-73	32-60	Cone	11.91	17.72	2.53		⊕	3.2	4	None			Pops	Bomb P.G.	2T	Unstable	Unstable	30	S to nothing; unstable to pops 1/2
↓	↓	↓	UDMH-50	↓		↓	↓	↓	↓	↓	↓	↓			↓	↓	↓	↓	↓	↓	↓	↓	~95.0	↓	↓	↓	↓			↓	↓	↓	↓	↓		S to 10 gr. P.G. 25 percent of time (1/4); unstable to pops 2/7
↓	↓	↓	MMH	↓		↓	↓	↓	↓	↓	↓	↓			↓	↓	↓	↓	↓	↓	↓	↓	~97.8	↓	↓	↓	↓			↓	↓	↓	↓	↓		S to 10 gr. P.B., 15 gr. P.G. 1/7; unstable to pops 7/19
↓	↓	↓	MMH-50	↓		↓	↓	↓	↓	↓	↓	↓			↓	↓	↓	↓	↓	↓	↓	↓	~91.8	↓	↓	↓	↓			↓	↓	↓	↓	↓		Always unstable to pops 6/6
↓		↓																																		Concluded: Inc. S with inc. MR. MMH stability ~UDMH-50 stability until MR > 2
↓	Transtage 21-11B	↓	UDMH-50	Alt. Rings Quadlet and F-O-F Triplet		336	0.036 Q 0.051 T	0.0292	8.15K	24	Nom 2.0	100			~40	~45	24-85	57-86	Cone	11.91	17.72	2.53	~98	⊕	3.2	4	None			Less Pops	Bomb P.G.	2T	Stable	Unstable	30	~20 gr. P.G. threshold
↓	↓	↓	MMH	↓		↓	↓	↓	↓	↓	↓	↓			↓	↓	↓	↓	↓	↓	↓	↓	~98		↓	↓	↓			↓	↓	↓	Stable	Unstable		20 gr. P.G. threshold } No correlation between pops and propellant temp., percent F.C. baffle cracks
↓	↓	↓	MMH-50	↓		↓	↓	↓	↓	↓	↓	↓			↓	↓	↓	↓	↓	↓	↓	↓			↓	↓	↓			↓	↓	↓	Unstable			Unstable to pops 2/3
JPL		↓	N_2H_4	UD	UD		0.02-0.173					15 to 450					40-140													Pops					29	Pop study: Observed that pops inc. with inc. D_{orif}, dec. V_{inj}, dec. P_c, dec. T_{inj}
↓		↓	MMH	↓	↓		↓					↓					↓													Pops						
↓		↓	UDMH	↓	↓		↓					↓					↓													No Pops					32	Popwise N_2H_4 ~MMH with UDMH much better (almost no pops)
↓	RC-1	↓	UDMH-50	↓	↓		↓			135	2.0	100							Cyl	18	15.9			⊕	Var.	4					Bomb	1T		Stable	33	Req. baffle length between 2.4 and 2.9 for dyn. stability
Thiokol	C-1	↓	MMH	↓	↓	10	↓		100	10	1.6	96					104-126	104-127		1.60		3.38		None			Helmholtz Reson.		6		Pulse Mode	1T		Stable	34	10 percent instability occurrence rate without absorber
UTC		↓	UDMH-50	Quadlet					8K	15	2.0	100							Cone	10		1.81		None							P.G.	4T, 5T		Unstable	35	Unique in that 1, 2, 3T modes were triggered but damped
Marquardt	S-IV-B Ullage	↓	↓	UD	UD	98			1.75K	18	1.62	100							Cyl	4.75		1.84	94	None												
↓	↓	↓	↓	↓	↓	↓			↓	↓	↓	↓							↓	↓		1.84		Added	~0.75	5 Rad Tabs 10 Rad Tabs								Unstable/ Stable		Unstable with 5 tabs, stable with 10 tabs
↓	↓	↓	↓	↓	↓	↓			↓	↓	↓	↓							↓	↓		2.75		None										Stable		Achieved stability by inc. CR
↓	"Zot" Study		N_2H_4																																36, 37	Loudest Explosion. Zots occur when cell press >1/2 VP of N_2H_4 at head end temperature. Zots aggravated by chamber wall temperature >head end temperature
↓	↓		UDMH-50																																	
↓	↓		MMH																																	
↓	↓		UDMH																																	

ABBREVIATIONS

Ann = annular chamber
CR = contraction ratio
cmpt = baffle compartment
Cyl = cylindrical chamber
$\bar{D}$ = mass median droplet size
dyn. = dynamically
elim. = eliminate
F = fuel
GEMSIP = Gemini Stability Improvement Program (Aerojet)
Horiz. = horizontal
JPL = Jet Propulsion Laboratory
L = acoustic cavity depth
LD = like doublet injection element
LM = lunar module
LOX = liquid oxygen
L. Trip = like propellant triplet element
MMH = monomethylhydrazine
NTO = N_2O_4
O = oxidizer
Orif. = orifice
PBPS = post boost propulsion system
P_c = chamber pressure

P.G. = pulse gun stability rating device
QWR = quarterwave acoustic resonator, acoustic cavity
RP-1 = kerosene-type fuel
S = stable
Spont = spontaneous
T_A = ambient temperature
T/LD = mixed triplet and like-doublet injection elements
UD = unlike doublet injection elements
UDMH = unsymmetrical dimethylhydrazine
UDMH-50 = 50 percent N_2H_4 and 50 percent UDMH
Unsym. = unsymmetrical
US = unstable
UTC = United Technology Center
Var = various
V_{inj} = injection velocity
W = width of acoustic cavity
W_T = total propellant flowrate
1R = first radial mode of instability
1T = first tangential mode of instability
2D = two-dimensional combustion chamber
2T = second tangential mode of instability
3T = third tangential mode of instability
ΔP = pressure pulse amplitude

FOLDOUT FRAME

1

FOLDOUT FRAME

2

FOLDOUT FRAME

3

As might be expected, little information was found that would allow a direct comparison between LOX/RP-1 systems and NTO/amine systems. However, a limited number of directly comparable tests was made with LOX/RP-1 and NTO/UDMH propellant combinations in Rocketdyne engines. Both propellant combinations were operated successfully in the Atlas sustainer, Thor/Jupiter, and E-1 engine systems but without attempting to determine the relative dynamic stability. In addition, both propellant combinations were used in a low-pressure, two-dimensional model of the F-1 and a so-called "barrel" chamber with inert gas pulse rating techniques being employed. The barrel chamber was a model of a relatively high thrust engine in which the chamber diameter was modelled but a high contraction ratio was used to reduce the thrust to a convenient level. The results indicated essentially no difference of stability in the two-dimensional engine but an indication of greater stability with the LOX/RP-1 combination with the barrel chamber was found. In addition, the LOX/UDMH propellant combination was found to be less stable than the LOX/RP-1 combination in tests with a high-pressure, two-dimensional model of the F-1 chamber. It should be noted, however, that in most cases no special effort was made to operate with the alternate propellant combination at its optimum mixture ratio and in many cases the exact mixture ratio achieved is not readily available.

The NTO/50-50 propellant combination was substituted for LOX/RP-1 when the Titan-I was uprated slightly to become the Titan-II. Both the Titan-I and Titan-II were only "statistically" stable (i.e., without disturbing the engine with a rating device, large numbers of tests could be made without the occurrence of spontaneous instabilities). These engines were unstable to artificial disturbances introduced with dynamic rating methods. No inherent stability advantage of either propellant combination appeared evident. The desire to achieve a dynamically stable Titan second-stage engine led to the GEMSIP (Gemini Stability Improvement Program) Program which culminated in the achievement of dynamic stability through an increase in thrust per element and the addition of injector face baffles.

The AFRPL performed a comparative stability study of the Transtage engine with N_2H_4, N_2H_4/UDMH (50-50), MMH, and N_2H_4/MMH (50-50) fuels and NTO oxidizer. With pulse guns being used for stability rating, the stability with the N_2H_4/UDMH (50-50) and MMH fuels was approximately equal and was significantly better than that obtained with either the N_2H_4 or N_2H_4/MMH (50-50) fuels (which were also conducive to "pops").

The susceptibility of amine-type fuels to pops, ignition spikes, etc., has often been of concern. While pops have been observed with LOX/RP-1 propellants, these pops have been attributed to entrainment of air in the propellant stream (Ref. 5). Pops observed with NTO/amine propellants have generally been attributed to blow-apart or stream separation (Ref. 31). Pops with NTO/amine propellants often result in sustained instability and/or hardware damage. A recent study of popping is reported in Ref. 30 in which the popping tendencies of N_2H_4, MMH, and UDMH were compared under varying injection conditions; UDMH was found to have less popping tendency than N_2H_4 or MMH, which were comparable to each other.

Minton and Swick (Ref. 36) report the investigation of manifold explosions (which they called "Zots") with NTO/amine propellants. Their experiments indicated that the condensation of residual fuel vapor in a cold, empty oxidizer manifold followed by the contracting of this detonable fuel condensate with fresh oxidizer leads to a manifold explosion or "Omzot". In Ref. , other types of Zots (Chizot, Pizot) are described, some of which would be called pops by other investigators. Zots were concluded to occur only under conditions where local pressure is greater than one-half the vapor pressure of N_2H_4 at the local temperature. The occurrence of Zots was found to be aggravated by high chamber wall temperatures.. Artificial explosions were created by adding NTO to identical amounts of various fuels. The "loudness" of the resulting detonations was measured and the resultant ranking may be an indication of susceptibility to occurrence of damaging Zots as well (Table 1).

The literature review indicated that UDMH is the least likely of the amine family to exhibit detrimental popping. MMH and (N_2H_4/UDMH, 50-50) are about equally susceptible to detrimental popping and are ranked as worse than UDMH but better than N_2H_4/MMH (50-50) and straight N_2H_4 which are considered quite susceptible.

Of particular interest to this program is the work of Abbe et al. at AFRPL (Table 1)) during which the Priem stability model was used successfully to: (1) predict the relative stability of an NTO/MMH engine design with an NTO/N_2H_4-UDMH (50-50) engine design (Ref. 27) and (2) to investigate the effect on stability of various design and operating conditions (Ref. 28). Abbe concluded that interactions between the various processes occurring in a combustor are so complex that an analytical model is necessary to predict the overall effect of a change in even a single design or operating parameter.

PRIEM MODEL INSTABILITY ANALYSIS

DESCRIPTION OF THE MODEL

The Priem-type instability model has been used extensively to predict engine stability. This model is based on numerical solution of a system of equations describing the combustion/flow field within a small annular region chosen as representative of the combustion chamber. The model considers basically only one dimension and, therefore, can approximate tangential modes but not radial, longitudinal, or coupled modes. Although this model has some limitations, it does include the detailed spray combustion processes in a quasi-steady sense and it does account for nonlinearities. Numerical solution of the equations gives a nondimensional overpressure, $A_p = \Delta p/p_c$, required to initiate a high-frequency instability (transverse mode) as a function of several nondimensional parameters. This critical overpressure, A_p, is determined from a series of computer experiments in which the oscillatory combustion response (history), subsequent to various initial disturbance levels, is calculated. The disturbance that will cause an oscillation that neither grows nor decays is the critical overpressure, the A_p. Conceptually, this is similar to bombing an engine with varying bomb sizes until the minimum size is found that will cause a sustained oscillation.

According to the Priem model, the stability index A_p is a function of several parameters:

$$\text{Burning Rate Parameter, } \mathscr{L} = \frac{mR}{CR} \tag{1}$$

$$\text{Velocity Difference, } \Delta V' = |V_{gas} - V_{drops}|/c \tag{2}$$

$$\text{Mass Accumulation Parameter, MAP} = M_{vap}/\omega_{inj}\ t_w \tag{3}$$

$$\text{Small } \Delta V' \text{ Parameter, } K_1 = \frac{10}{3} Sc_o^{-1/3} \left(\frac{D_{dr}\ c\rho}{\mu}\right)_o^{-1/2} \tag{4}$$

$$\text{Droplet Drag Parameters, } K_2 = \left(\frac{3\ C_D\ R\ M_{vap}}{4\ (\rho D)_{dr}}\right)_o \text{, and} \tag{5}$$

$$K_3 = \left(\frac{3\ C_D\ R\rho}{4\ (\rho D)_{dr}}\right)_o \tag{6}$$

where the subscript o refers to steady-state (stable) conditions. The values of these parameters may be calculated from the results of steady-state combustion model calculations. Generally (for most propellants and injector configurations), the most influential parameters are $\mathscr{L}$, the burning rate parameter, and $\Delta V'$, the axial velocity difference.

A generalized plot of the calculated relationship between A_p, $\mathscr{L}$ and $\Delta V'$ is shown in Fig. 1. The parameter $\Delta V'$ varies with axial position in the engine and usually has a minimum value near the injector. The model predicts that this region, corresponding to a minimum $\Delta V'$, is the most unstable or most sensitive zone and, therefore, the analysis is generally done for this location only. Further, although

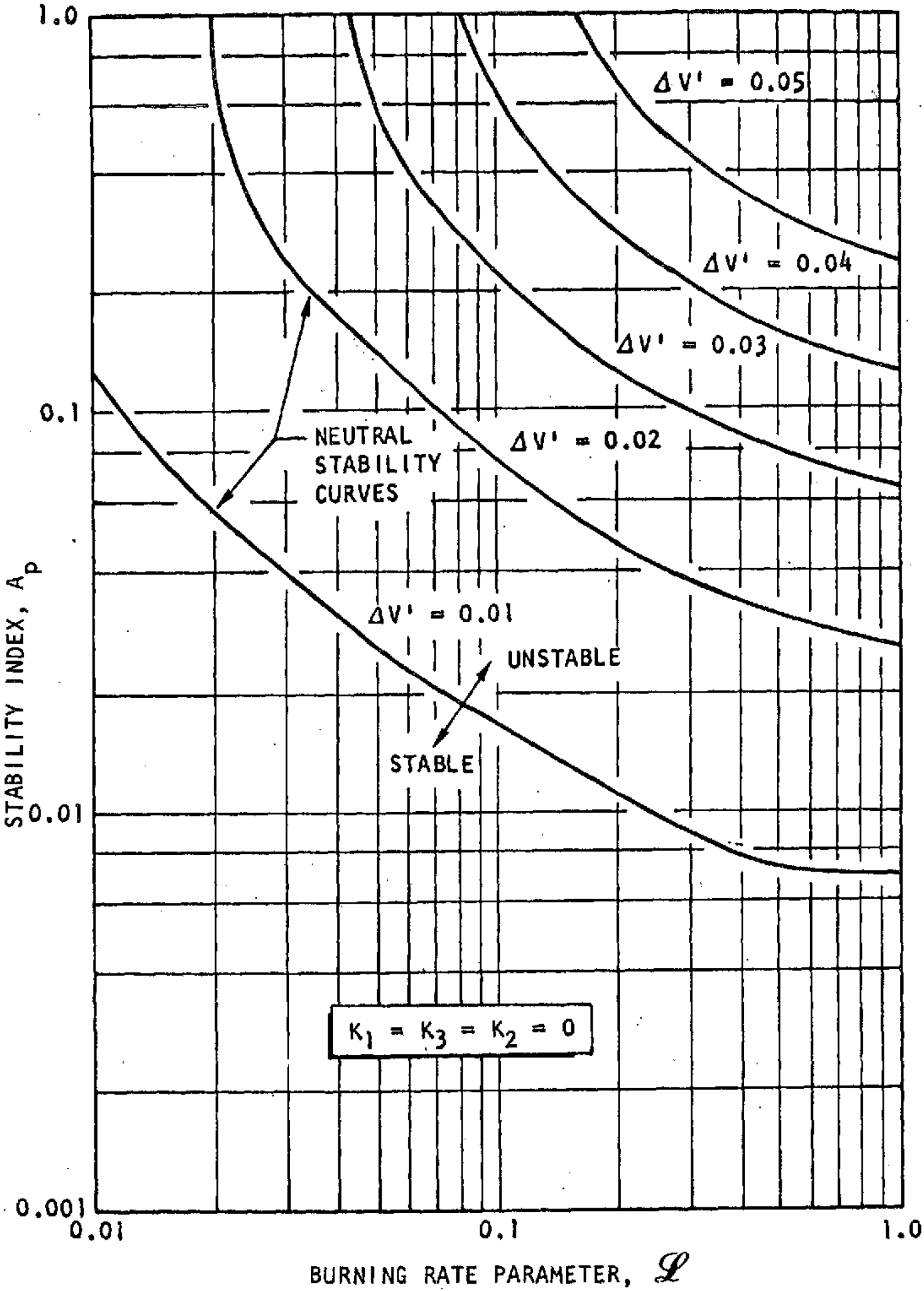

Figure 1. Priem-Type Stability Map Showing Effect of ΔV'

the value of $\Delta V'$ may be predicted to be zero at this location, it is generally agreed that a minimum value of 0.01 is more reasonable because of turbulence effects and nonuniformity of dropsizes. Thus, the stability analysis is commonly made with $\Delta V' = 0.01$ and for the sensitive zone.

The relationship between A_p, $\mathscr{L}$, and K_1, for $\Delta V' = 0.01$ is shown in Fig. 2. The parameter K_1 arises through consideration of a more exact burning rate expression, than was originally used by Priem, for small values of $\Delta V'$ (Ref. 38).

The relationship between A_p, $\mathscr{L}$, and MAP is shown in Fig. 3. The effect of the MAP parameter is to raise the stability limit at locations where a large proportion of the propellant has already been burned, and a small amount of unvaporized propellant is left to sustain an instability by burning. The most sensitive zone of instability (minimum $\Delta V'$) normally occurs at an axial location where a large proportion of the propellant is unburned (large MAP); therefore, the MAP parameter is generally of little importance.

The relationship between A_p, $\mathscr{L}$, K_2 and K_3 is shown in Fig. 4. These parameters arise from a modification to the Priem model to include the effect of droplet drag (Ref. 38). These curves show that K_1 and K_2 can significantly change A_p, indicating the importance of droplet drag.

Results from a steady-state combustion model are required for the Priem-type analysis. Such steady-state models have been used extensively and several model variations are available. Generally, in these models, the mass and mixture ratio distributions created by the injector are assumed uniform to avoid the complexities of handling the nonuniform case. Moreover, in most cases it is satisfactory to employ a model based on an evaporation coefficient rather than including droplet heating. This approximation is good as long as the chamber pressure is significantly below the critical pressure of the propellants.

Steady-state combustion models are based on numerical solution of the differential equations describing the spray combustion processes. These equations apply to arrays of discrete droplets and, generally, are restricted to one-dimensional flow. Therefore, the calculation is usually begun at a position downstream from the injector where the equations are expected to apply. The calculation then proceeds downstream in a stepwise fashion to the nozzle throat. Iteration procedures are employed to ensure that the flow satisfies sonic conditions at the throat. The input required by the steady-state models includes:

- Chamber geometry (diameter, length, contraction ratio)
- Combustion gas properties (ρ, T, μ, k, etc.) as a function of mixture ratio (obtained from equilibrium performance calculations)
- Axial position where calculation is to begin
- Initial condition of spray and gas at starting position
    - Spray dropsize and dropsize distribution
    - Spray velocity
    - Spray temperature

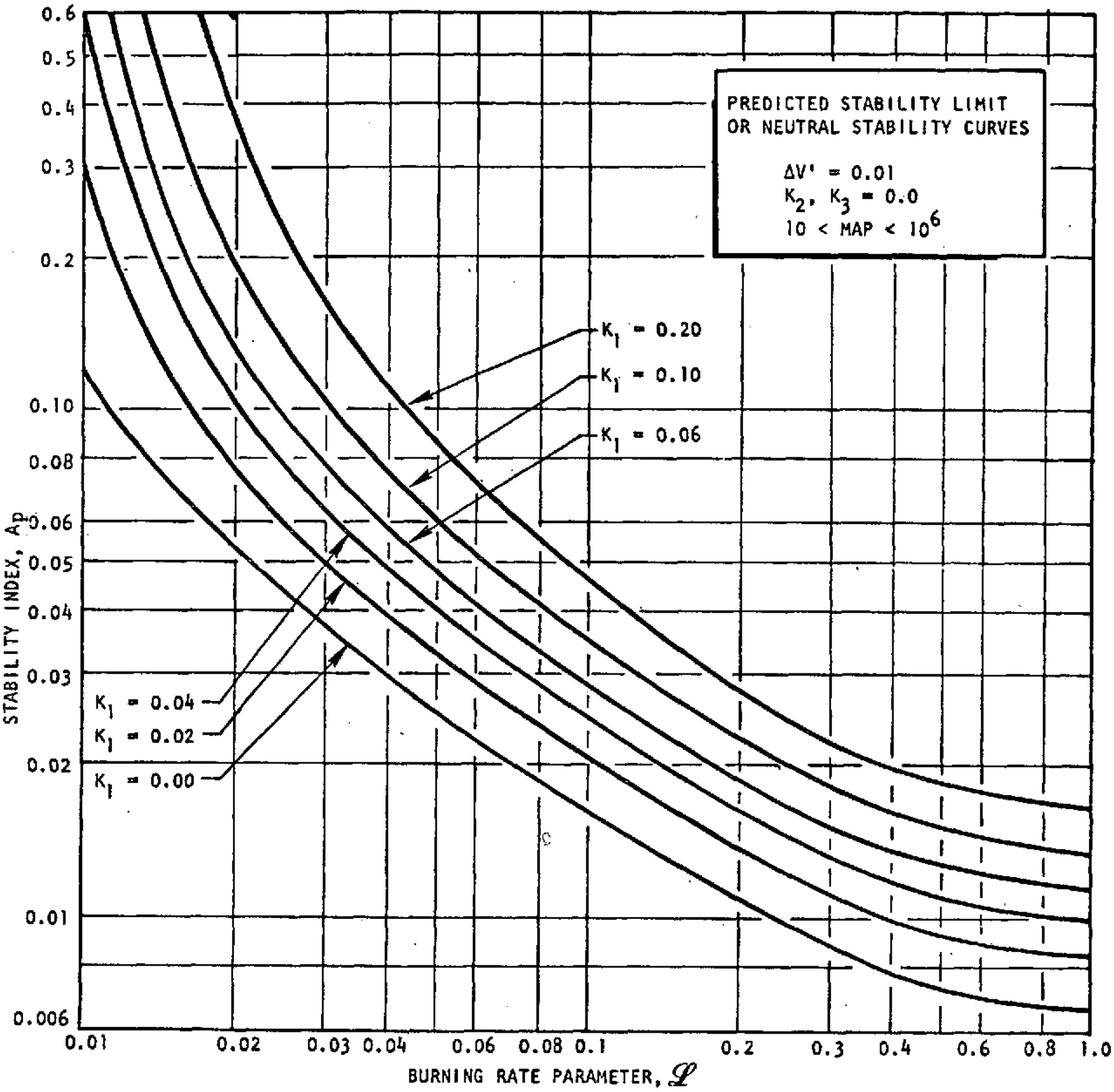

Figure 2. Priem-Type Stability Map Showing Effect of K_1 Parameter

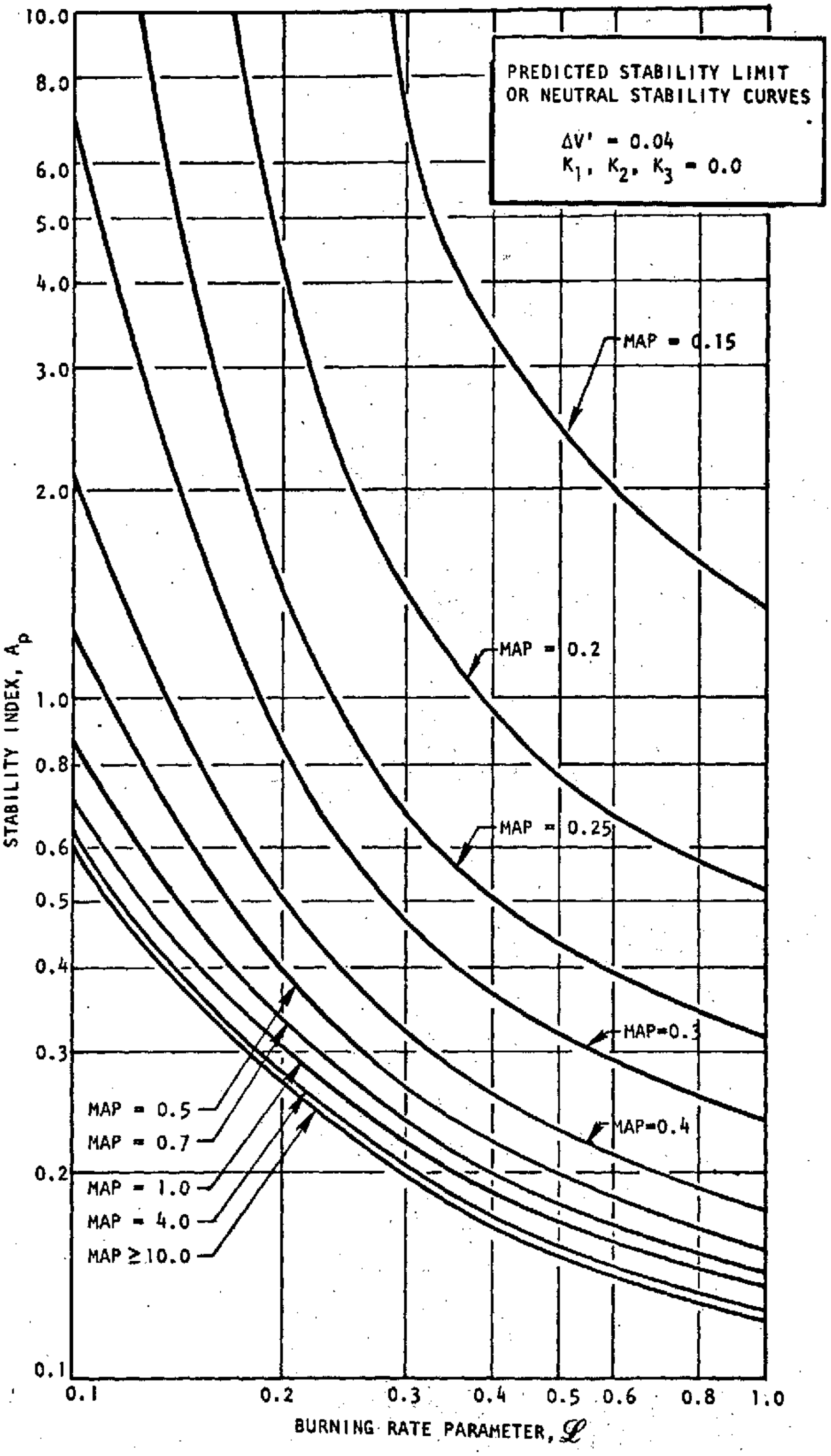

Figure 3. Effect of MAP Parameter on Predicted Stability Limits

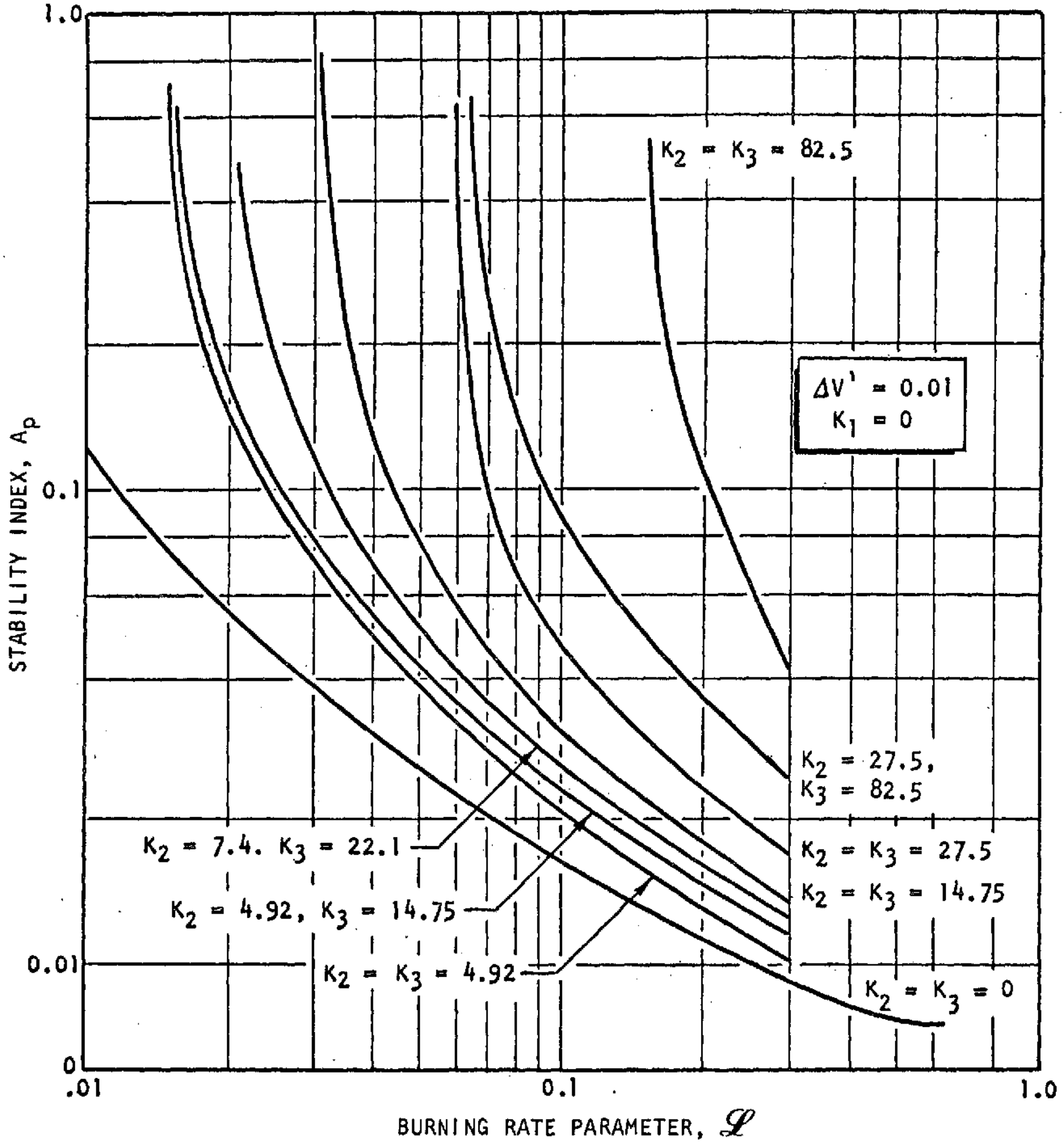

Figure 4. Effect of K_2 and K_3 Parameters on Predicted Stability Limits

- Gas composition (MR)
- Gas flowrate (percent of spray burned)
- Gas pressure
- Initial dropsize
- Initial drop velocity
- Gas velocity
- Gas composition (percent of fuel burned, percent of oxidizer burned)
- Initial overall percent burned (vaporized)

Output from the steady-state combustion model includes the following variables as a function of axial location:

- Dropsize
- Drop velocity
- Gas velocity
- Gas composition (fraction of fuel burned, fraction of oxidizer burned)
- Gas physical properties
- Overall fraction burned (vaporized)

The Priem model input parameters can be calculated from the steady-state combustion model output through use of the following relationships:

$$m = \frac{\Delta\varepsilon}{\Delta z} \tag{7}$$

where ε is the overall fraction burned.

$$M_{vap_o} = \left\{ (1-X_{OX}) \frac{MR}{MR+1} + (1-X_F) \frac{1}{MR+1} \right\} \rho_o \tag{8}$$

where X_{OX}, X_F are the burned fractions of oxidizer and fuel, respectively. Also:

$$\omega_{inj_o} = \frac{\dot{w}_{inj}}{A_c} m \tag{9}$$

$$t_w = \frac{2\pi R}{c} \tag{10}$$

$$C_D = \begin{cases} 27.0 \, Re^{-0.84} & Re \leq 80 \\ 0.271 \, Re^{0.217} & 80 < Re < 10^4 \\ 2.0 & Re \geq 10^4 \end{cases} \tag{11}$$

where $\mathrm{Re} = \left(\frac{D_{dr} |\Delta V| \rho}{\mu} \right)_o$

The use of the Priem-type model in conjunction with a steady-state combustion model allows a relatively thorough evaluation of variations in engine stability with the parameters of interest. These parameters can include dependent parameters such as dropsize as well as operating and design variables such as chamber pressure or contraction ratio.

STEADY-STATE COMBUSTION MODEL CALCULATIONS

In formulating the analysis scheme, particular care was taken to group the effects of the many independent variables such that a parametric analysis would not require excessive computer time or manual labor. Moreover, the results must be expressible in a reasonable number of graphs, tables, or example problems. A summary of this analysis scheme and selection of analysis parameters is described below.

A so-called k' or evaporation coefficient steady-state model was used with the following input parameters:

- Chamber diameter
- Chamber contraction ratio (throat diameter), CR
- Chamber length
- Chamber pressure, p_c
- Mixture ratio, MR
- Initial spray velocity, V_{inj}
- Initial spray dropsize, $\overline{D}_f$ and $\overline{D}_{ox}/\overline{D}_f$

While the chamber and throat diameters are actually input into the steady-state model, the model is one-dimensional and actually considers only the total propellant mass flux (flowrate per chamber cross-section area) $\dot{w}_t/A_c$. Also:

$$\frac{\dot{w}_t}{A_c} = \frac{p_c A_t g_c}{c^* A_c} = \frac{p_c g_c}{c^* CR} \tag{12}$$

This expression was used to eliminate the chamber diameter from the list of key parameters shown above.

Further, propellant dropsize was treated as an independent variable, which effectively separates some of the effects of injector orifice, injection pressure drop, liquid propellant properties, and chamber contraction ratio.

The coding of the k' computer model was modified to directly calculate the following Priem parameters from the steady-state model results: m, M_{vap_o}, ω_{inj_o}, $\Delta V'$

and K_1. In addition, the following Priem-related parameters were calculated by the model as functions of axial position:

$\mathscr{L}/R$

$MAP(R)$

K_2/R

K_3/R

The effect of chamber size (radius, R) on the Priem parameters and thus, the stability limit (A_p), was calculated through use of Fig. 2 without additional steady-state model results being required.

Additional practices were followed to reduce the number of variable steady-state model input parameters from the nine listed earlier to a total of six, viz., propellant combination, CR, p_c, V_{inj} (or Δp_{inj}), $\overline{D}_f$ and $\overline{D}_{ox}/\overline{D}_f$. The chamber length was held constant at 9 inches (injector face to beginning of nozzle convergence). The combustion efficiency (η_c*) was assumed to be 96 percent. Mixture ratio was fixed for each propellant combination (thus fixing the theoretical c*); a mixture ratio of 1.60 was used for both NTO/MMH and NTO/50-50 propellant combinations.

The assumed initial percent burned at the computational starting position was 1.0 percent of each propellant. The spray velocity was calculated from selected values of Δp_{inj}, with $C_d = 0.89$ being used. A specialized form of the Nukiyama-Tanasawa dropsize distribution was used which allowed the distribution to be calculated from a specific mass median dropsize. This distribution is based on work by Ingebo as described in Ref. 40. The distribution function is:

$$\frac{dV}{dD} = \begin{cases} (4.63/\overline{D})^6 \; (D^5/120) \; \exp\,(-4.63\; D/\overline{D}) & D \leq 2.00\; \overline{D} \\ 0.0 & D > 2.00\; \overline{D} \end{cases}$$

where $D = D_{ox}$ or D_f and V is the volume fraction of the spray. An axial step size of 0.020 inch was used in the computer calculation procedure. The inclusion of droplet heating is the k' combustion model was not attempted.

A total of 240 computer runs with the steady-state combustion model was made for the NTO/MMH and NTO/50-50 propellant combinations. These computer runs encompassed the entire desired matrix of steady-state combustion conditions to be investigated for those propellant combinations. The steady-state model runs for each propellant combination included all possible combinations of the following variables:

Chamber Pressure, p_c = 125 psia, 200 psia

Injector Pressure Drop, $\Delta p = 0.2\; p_c,\; 0.4\; p_c$

Combustor Contraction Ratio, CR = 2.0:1, 3.0:1

Fuel Dropsize (Mass Median), $\overline{D}_f$ = 60, 100, 200, 300, 400 microns

Ratio of Oxidizer to Fuel Dropsize, $\overline{D}_{ox}/\overline{D}_f$ = 0.5, 0.75, 1.0

RESULTS FROM PRIEM-TYPE ANALYSIS

Steady-state combustion parameters needed as input to the Priem instability model were tabulated from the steady-state model results as functions of distance and chamber radius, if appropriate, for each case. The location of the most sensitive zone was found to shift further downstream as the variables $\overline{D}_f$, $\overline{D}_{ox}$, CR, Δp_{inj} and p_c were increased. For operation at $\overline{D}_f$ = 60 microns, $\overline{D}_{ox}$ = 30 microns, CR = 2, Δp_{inj} = 0.20 p_c and p_c = 125 psia, the most sensitive zone was located about 0.02 inch downstream of the starting point for the computer calculations. The maximum shift in the location of the sensitive zone was found to occur at $\overline{D}_f$ = 400 microns, $\overline{D}_{ox}$ = 400 microns, CR = 3, Δp_{inj} = 0.40 p_c and p_c = 200 psia. The sensitive zone was located at slightly more than 2.00 inches from the starting point for these conditions. Although the value of $\Delta V'$ at the most sensitive zone was assumed to be its "turbulence," or minimum, value of 0.01, the actual numerical value was usually only 0.002 to 0.004.

In all cases, the numerical values of MAP (representing the effect of remaining unvaporized propellant) and K_2 and K_3 (representing the effects of droplet drag) were found to be of such a magnitude that their influence on predicted stability was negligible for the entire matrix of computer runs. This is not unusual for storable propellants. Calculation of the Priem stability index, A_p, was thus simplified considerably, being a function of only the non-dimensional burning-rate parameter, $\mathscr{L}$, the parameter K_1 (the correction for small $\Delta V'$) and the non-dimensional $\Delta V'$, which was assumed to have a turbulence level value of 0.01 at the sensitive zone.

Two methods of calculating the burning rate parameter were used. One method involved the use of the local value of the fraction burned per unit length (m) at the most sensitive zone. With the second method, the average value of m over the first 2 inches of the combustion zone was calculated, which included the "most sensitive" zone for all computer cases and which would avoid high local "point" values whose magnitude is sensitive to poorly defined steady-state model input parameters such as initial percent of propellant burned. The local value of m at the sensitive zone was almost a factor of 10 larger than the averaged value of m over the first 2 inches of chamber length for small dropsizes while for large dropsizes it was roughly one-half the averaged value.

The calculated value of K_1 increased with decreasing p_c, $\overline{D}_f$ and $\overline{D}_{ox}$ but was independent of CR and Δp_{inj}. A maximum value of K_1 = 0.204 was obtained for p_c = 125 psia, $\overline{D}_f$ = 60 microns and $\overline{D}_{ox}$ = 30 microns. A minimum value of K_1 = 0.041 was obtained for p_c = 200 psia and $\overline{D}_f$ = $\overline{D}_{ox}$ = 400 microns.

Values of the Priem stability index, A_p, were determined for the previously mentioned ranges of chamber pressure, injection pressure drop, contraction ratio, and fuel and oxidizer dropsize for both the NTO/MMH and NTO/50-50 propellant combinations at combustor radii of 2, 4, and 6 inches. Figure 2 was used in conjunction with the numerical values of $\mathscr{L}$ and K_1 obtained from the computer printout to obtain the A_p value.

The results from this analysis are summarized in Appendix B, examples of which are shown in Fig. 5 and 6. These results have been placed in an appendix

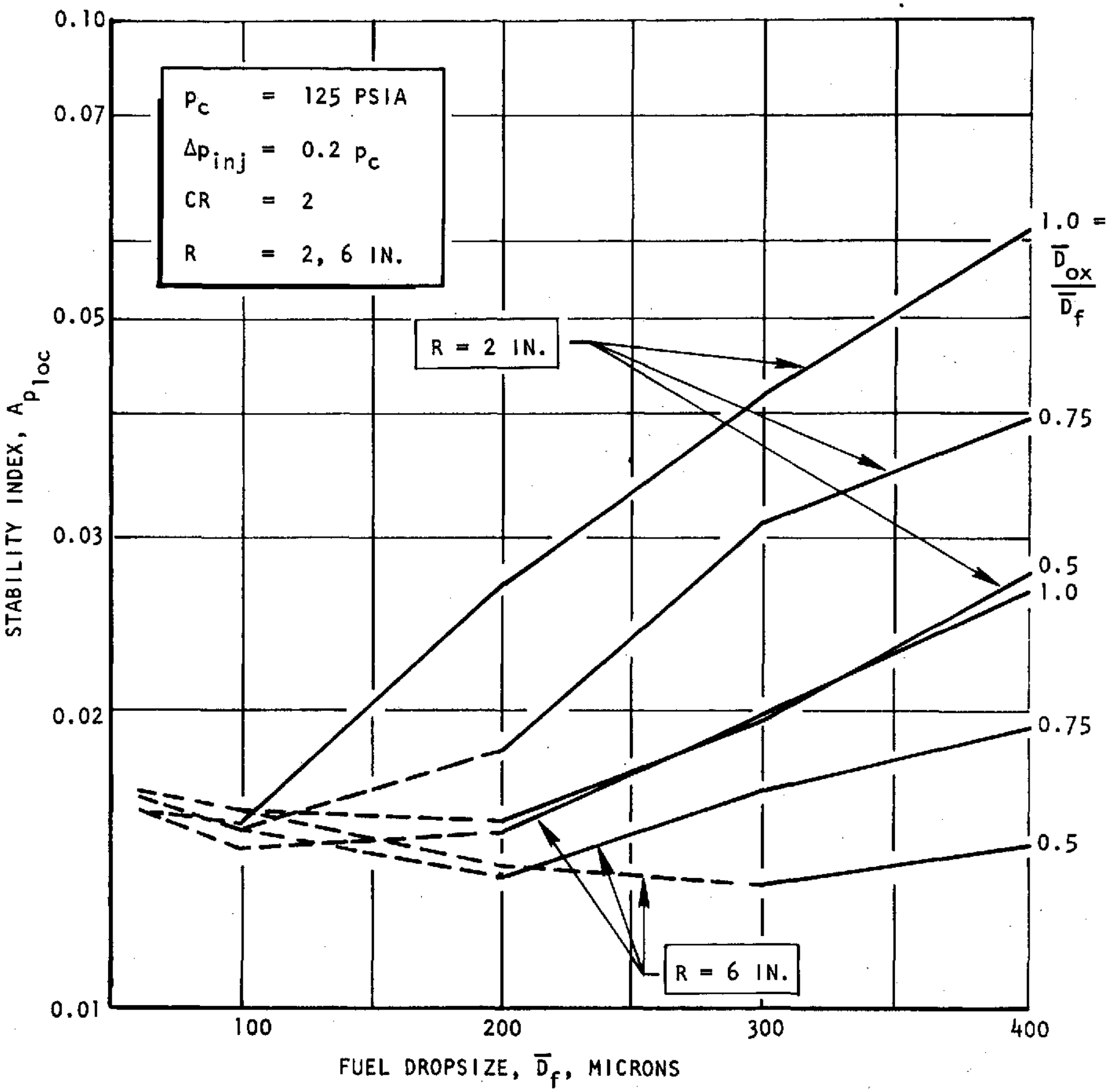

Figure 5. Local Stability Index as a Function of Dropsize for p_c = 125 psia, Δp_{inj} = 0.2 p_c, CR = 2

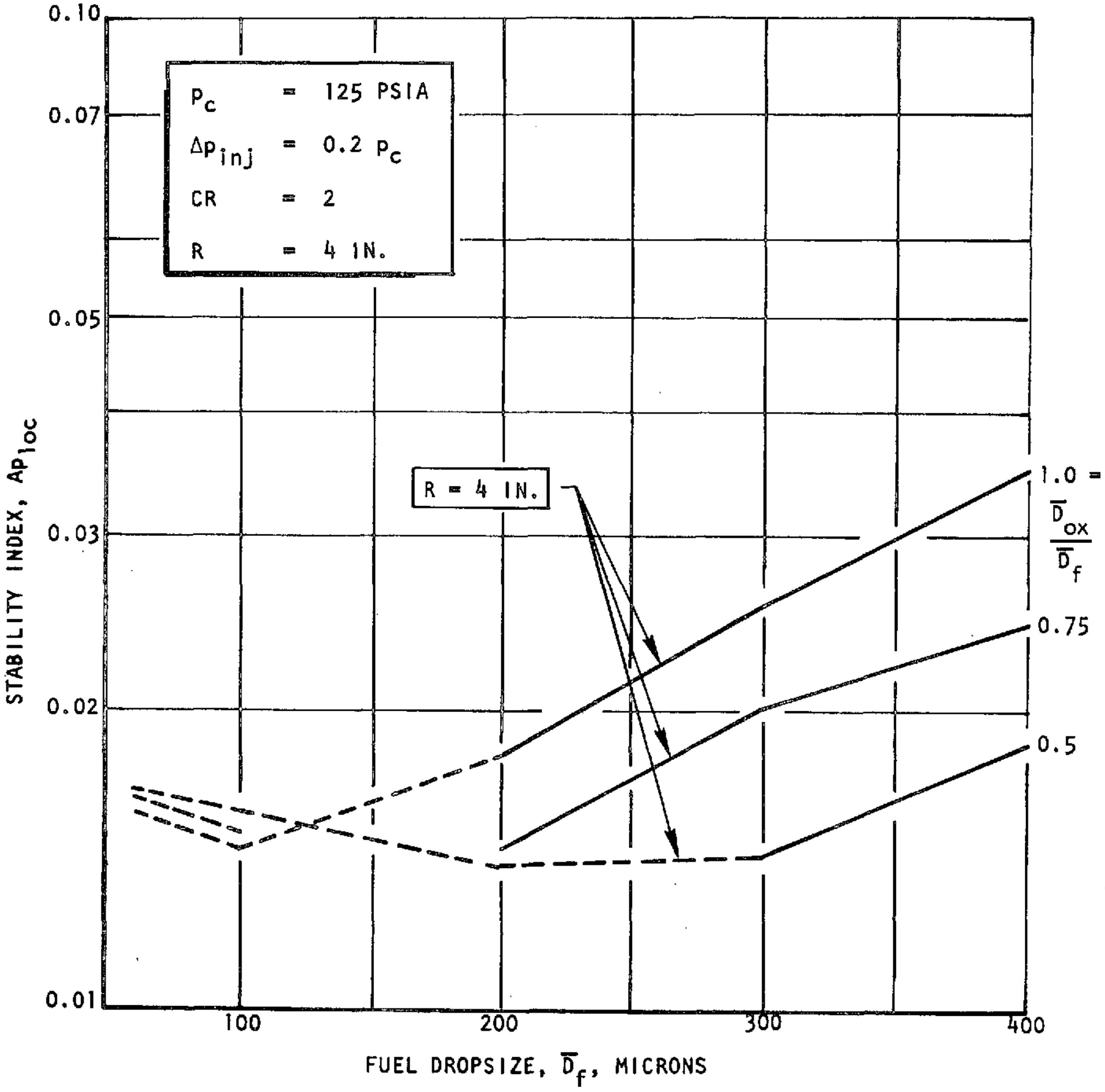

Figure 6. Local Stability Index as a Function of Dropsize for p_c = 125 psia, Δp_{inj} = 0.2 p_c, CR = 2

because of the large number of figures involved. Results obtained with the local value of the burning rate are presented in Fig. B-1 through B-16, while results obtained with the averaged value of the burning rate over the first 2 inches of axial distance are presented in Fig. B-17 through B-32. The dotted lines in the figures represent an extrapolation of the stability curve shown in Fig. 2 to a value of $\mathscr{L}$ between 1.0 and 10. For purposes of extrapolation it was assumed that the stability limit remained invariant beyond $\mathscr{L} = 1.0$, i.e., $A_p\ (\mathscr{L} > 1.0) = A_p\ (\mathscr{L} = 1.0)$. Attempts during previous Rocketdyne programs to extend the range of the stability limit plot in the direction of greater $\mathscr{L}$ were unsuccessful because numerical instability was encountered in the computer solution of the programmed equations. While Priem's original work (Ref. 41) showed a bowl-shaped curve, with A_p increasing with increasing $\mathscr{L}$ for $\mathscr{L} > 1$, more recent work at Rocketdyne indicates that it may not increase, the apparent increase being due to numerical instabilities. Therefore, the dotted lines are believed to be upper limits for the stability index.

Many of the A_p curves shown in Fig. B-1 through B-32 exhibit a minimum in A_p. This results from the influence of K_1, which is dominant over the influence of the $\mathscr{L}$. It occurs most often when the value of $\mathscr{L}$ is relatively large and the variation of A_p with $\mathscr{L}$ is small (see Fig. 2). Although this minimum in A_p implies a "worst" dropsize, the curves on which the results are based have been extrapolated somewhat and this conclusion may be invalid.

The Priem-type stability analysis showed no significant difference in stability between the NTO/MMH and NTO/50-50 propellant combinations. The effect of varying each of the other parameters on stability, the remaining parameters being constant, can easily be determined by comparison of Fig. B-1 through B-32. These results indicate that stability increases (improves) with increasing dropsize (for fixed CR, $\Delta p_{inj}/p_c$, p_c, D_{ox}/D_f, and chamber diameter), contraction ratio (for fixed dropsize, $\Delta p_{inj}/p_c$, p_c and chamber diameter) and fractional injection pressure drop as well as with decreasing chamber pressure and chamber diameter. However, care must be exercised in making and using such comparisons because the results depend on the parameters being held constant. The parameters being held constant for the results just noted imply hardware changes to allow them to be held constant. Different results would be expected if, e.g., chamber pressure were changed with fixed hardware.

The parameters chosen for the stability calculations (chamber pressure, fractional injection pressure drop, contraction ratio, chamber diameter and dropsize) were chosen because the selection minimized the number of parameters considered and emphasized the important physical processes. Nevertheless, the results (Fig. B-1 through B-32) may be used by interpolation to estimate the Priem stability index and, thus, relate stability to various hardware configurations and operating conditions. Such calculations have been made that illustrate the use of the curves. The principal additional information that is needed for this assessment is some method of calculating dropsizes of the propellants.

The influence of varying certain design parameters on stability with alternate constraints, relative to a reference case, was calculated. The reference case was:

p_c = 125 psia

D = 8.0 inches (chamber diameter)

$CR = 2.0$

$\Delta p_{inj}/p_c = 0.40$

$\overline{D}_f = 300$ microns

$\overline{D}_{ox}/\overline{D}_f = 0.5$

$MR = 1.6$

The local stability limit for this base case ($A_{p_{loc}} = 0.0164$) is given by Fig. B-5.

The parameter constraints that were used to relate the various model parameters to the design or operating parameters are summarized below. Thrust is related to chamber pressure and contraction ratio through the thrust coefficient:

$$F = \frac{\dot{w}_t C_F c^*}{g_c} = p_c A_t C_F = \frac{p_c A_c C_F}{CR} \tag{13}$$

Injection velocity can be expressed as either a function of Δp_{inj} or of flowrate per orifice and orifice size where the flowrate per orifice is, in turn, function of thrust per element:

$$V_{inj} = C_d \sqrt{2c \frac{\Delta p_{inj}}{\rho_\ell}} \tag{14}$$

$$V_{inj} = \frac{\dot{w}_{orif}}{\rho A_e} = \frac{\dot{w}_{orif}}{\rho \pi d^2_{orif}/4} \tag{15}$$

where

$$\dot{w}_{orif} = \frac{C(F_e) g_c}{C_F \eta_c{}^*}$$

and $C(F_e)$ is a function of the MR and element type that relates flow per element to flow per orifice.

The dropsize may be related to such variables as orifice diameter, injection velocity, and chamber pressure through any of a number of correlations. The Dickerson like-doublet dropsize expression (see Appendix A) was used to determine the effect of various parameters on dropsize. This equation gives the relationship $\overline{D} \sim V_{inj}{}^{-0.852}\, d_{orif}{}^{0.568}$.

Results from the calculations for alternate parameters are summarized in Table 2 and are discussed below. If chamber pressure is varied at a constant thrust level, then either chamber area or chamber contraction ratio must also vary (see Eq. 13) but total propellant flow is fixed. Assuming the number of injector elements is held constant, either (1) the injector pressure drop, Δp_{inj}, may be fixed or (2) the

TABLE 2. PREDICTED EFFECT OF PARAMETER VARIATIONS ON STABILITY

Parameter Variation	p_c, psi	Chamber Diameter, inch	CR	Δp_{inj}, psi	$\Delta p_{inj}/p_c$	Injection Velocity, $v/v_{ref}^{(2)}$	Thrust, $F/F_{ref}^{(2)}$	Thrust Per Element, $\tau/\tau_{ref}^{(2)}$	Injection Orifice Diameter, $D/D_{ref}^{(2)}$	$\overline{D}_f^{(1)}$, microns	Stability Index, $A_p/A_{p,ref}^{(3)}$
Reference Case	125	8.0	2.0	50	0.40	1.0	1.0	1.0	1.0	300	1.000
Increase Chamber Pressure											
Increase Flowrate	200	8.0	2.0	128	0.64	1.6	$1.6^{(4)}$	1.6	1.0	201	0.884
Reduce Throat Area	200	8.0	$3.2^{(5)}$	50	0.25	1.0	1.0	1.0	1.0	300	1.043
				80	0.40	1.26	1.0	1.0	0.88	230	1.012
Reduce Chamber Diameter	200	6.3	2.0	50	0.25	1.0	1.0	1.0	1.0	300	1.049
				80	0.40	1.26	1.0	1.0	0.88	230	0.988
Increase Contraction Ratio											
Increase Chamber Diameter	125	9.8	3.0	50	0.40	1.0	1.0	1.0	1.0	300	1.299
Reduce Throat Area	$187.5^{(5)}$	8.0	3.0	50	0.27	1.0	1.0	1.0	1.0	300	1.067
				75	0.40	1.0	1.0	1.0	0.90	248	1.055
Reduce Injection Δp	125	8.0	2.0	25	0.2	0.71	1.0	0.71	1.0	403	1.140
								1.0	1.19	419	1.189

(1) $\overline{D}_{ox}/\overline{D}_f$ = 0.5 for all cases

(2) Referred to reference case; $A_{p,ref}$ = 0.0164 (local value)

(3) $A_{p,ref}$ = 0.0164 (local value); relative values greater than indicate improved stability

(4) Only case in which thrust was allowed to vary

(5) Steady-state combustion model was not run for these cases; A_p obtained by interpolation

fractional injection pressure drop, $\Delta p_{inj}/p_c$, may be fixed, with corresponding changes in injection velocity and orifice diameter. Results from a series of calculations for several parameter variations are summarized in Table 2.

The analysis indicates that an increase in chamber pressure from 125 to 200 psia will worsen stability only if thrust increased (see Table 2). Improved stability is predicted if p_c is increased to 200 psia while thrust and injection velocity were held constant, irrespective of whether contraction ratio or chamber diameter was increased. No appreciable change in stability was predicted for an increase in p_c to 200 psia, while holding thrust and fractional injection pressure drop, $\Delta p/p_c$, constant when either contraction ratio or chamber diameter was increased.

An increase in contraction ratio from 2.0:1 to 3.0:1 improved the predicted stability if p_c was allowed to increase so as to maintain constant thrust (Table 2). A substantial improvement in predicted stability occurred if the chamber diameter was allowed to increase while maintaining constant p_c and thrust.

A decrease in injection Δp (or injection velocity), while maintaining constant thrust, improved the predicted stability when either the number of elements or the orifice size was increased. This result is exactly opposite the conclusion that might be reached from the A_p curves directly with the original constraints on the remaining parameters. The stability decrease caused by the decreased injection Δp indicated by the curves is more than offset by the stability increase caused by the resultant increase in dropsize.

These results clearly show the importance of carefully defining the manner in which parameters are varied, viz., the parameter constraints. Different results may be obtained from variations in the same parameter depending on how the remaining parameters are controlled. Nonetheless, the stability index plots developed during this study allow appropriate evaluations to be made. Use of the local stability index plots (Fig. B-1 through B-16) is recommended over the averaged stability index plots (Fig. B-17 through B-32); the effect of the various parameters on stability appears to be overly suppressed in the latter plots by the averaging. Dropsize, and therefore the method used to determine dropsize, has a strong effect on predicted stability. Unfortunately, fully satisfactory methods of determining dropsize are not available. For this reason the stability index plots have been developed for a wide range of dropsizes to that they are not restricted to particular methods of predicting dropsize.

QUASI-LINEAR STABILITY ANALYSES

The analyses that form the basis for the Northern Research and Engineering Corporation (NREC) stability model and, also, the generalized acoustic cavity damping model, as well as the previously developed cavity damping model, may be described as quasi-linear (i.e., linearized equations are used and nonlinearities are introduced only through the boundary conditions). Such analyses are not likely to accurately predict strongly nonlinear phenomena but they may be used to reasonably represent three-dimensional stability problems. On the other hand, fully nonlinear analysis methods are intractable for three-dimensional stability problems.

The conservation equations for a two-phase mixture may be linearized to obtain an inhomogeneous wave equation, as described by Culick (Ref. 42). The resultant wave equation is:

$$\nabla^2 \tilde{p} - \frac{1}{c^2} \frac{\partial^2 \tilde{p}}{\partial t^2} = -\rho_o \nabla \cdot (\vec{u}_o \cdot \nabla \vec{\tilde{u}} + \tilde{u} \cdot \nabla \vec{u}_o) + \frac{1}{c^2} \vec{u}_o \cdot \nabla \frac{\partial \tilde{p}}{\partial t} +$$

$$\nabla \cdot (\vec{\tilde{F}} - \vec{\tilde{\sigma}}) + \frac{\gamma}{c^2} \frac{\partial \tilde{p}}{\partial t} \nabla \cdot \vec{u}_o - \frac{1}{c^2} \frac{\partial \tilde{\mathscr{P}}}{\partial t} \qquad (16)$$

where

$$\tilde{\mathscr{P}} = \frac{R}{C_v} \left\{ \tilde{e}_s \bar{w}_s + \bar{e}_s \tilde{w}_s + \tilde{Q} + \tilde{Q}_s \right\}$$

This equation was derived under the assumptions that the oscillatory quantities are small compared to their mean value and, further, that the steady-flow Mach number is small compared to unity (Ref. 42). The term $\mathscr{P}$ represents the oscillatory combustion. This equation must be solved subject to a boundary condition that may be written as:

$$\vec{N} \cdot \nabla \tilde{p} = -\left\{ \rho_o \frac{\partial \vec{\tilde{u}}}{\partial t} + \rho_o (\vec{u}_o \cdot \nabla \vec{\tilde{u}} + \vec{\tilde{u}} \cdot \nabla \vec{u}_o) - (\tilde{F} - \tilde{\sigma}) \right\} \cdot \vec{N} \qquad (17)$$

Culick's formulation of several stability problems is based on a first-order approximate solution to these equations (Ref. 42). The NREC model is based on the same first-order approximate solution with an approximate expression for the combustion source terms (Ref. 1). The Rocketdyne generalized cavity damping model is based on a more accurate iterative-variational solution to these equations with a similar expression for the combustion source terms.

The indicated first-order approximate solution may be obtained in the following way. A solution to the time-independent homogeneous wave equation and boundary conditions corresponding to Eq. 16 and 17 can usually be obtained, i.e.:

$$\nabla^2 \phi_N + \eta_N^2 \phi_N = 0 \qquad (18)$$

$$\vec{N} \cdot \nabla \phi_N = 0 \qquad (19)$$

where the subscript N stands for three indices, one for each dimension. Alternate boundary conditions can be used, and are desirable in some cases. Assuming a harmonic time dependence ($e^{j\beta t}$, $\beta = \omega + j\alpha$) the time independent forms of Eq.16 and 17 may be written as:

$$\nabla^2 \tilde{p} + k^2 \tilde{p} = h \tag{20}$$

$$\vec{N} \cdot \nabla \tilde{p} = -f \tag{21}$$

where h and f represent the time independent form of the right-hand sides of Eq. 16 and 17. If Eq. 18 and 20 are multipled by $\tilde{p}$ and ϕ_N, respectively, then one equation is subtracted from the other and the result integrated over the chamber volume, the result may be expressed as

$$k^2 = \eta_N{}^2 + \frac{\int \phi_N h dV + \int f \phi_N dS}{\int \phi_N{}^2 dV} \tag{22}$$

The integrals may be evaluated with ϕ_N being used in the expressions for h and f as an approximation for the pressure $\tilde{p}$.

The latter equation may also be obtained through use of Green's functions with an eigenfunction expansion being used for the Green's function. A more useful expression has been obtained by Culick from further evaluation of the integrals in Eq. 22, i.e.;

$$\begin{aligned}(k^2 - \eta_N{}^2) \int \phi_N{}^2 dV = \{ & i \eta_N \int \left[\mathrm{Re}(y) + \vec{M}_o \cdot \vec{N} \right] \phi_N{}^2 dS - \\ & i \eta\cdot_N \int \phi_N{}^2 (\nabla \cdot \vec{M}_o)\, dV - \int \mathrm{Re}(\vec{\tilde{F}}) \cdot \nabla \phi_N dV - \\ & i \frac{\eta_N}{c} \frac{R}{C_v} \int \mathrm{Re} \left\{ \tilde{e}_s \, w_s + \tilde{Q} + Q_s \right\} \phi_N dV + \\ & i \frac{\eta_N \gamma}{\rho_o c} \int \overline{w}_s \, \phi_N{}^2 dV + \int \overline{w}_s \, \mathrm{Re} \left\{ \vec{\tilde{u}} - \vec{\tilde{u}}_s \right\} \cdot \nabla \phi_N dV \end{aligned} \tag{23}$$

NREC INSTABILITY MODEL*

The NREC model is based on a quasi-linear solution to the conservation equations describing the combustion/flow field. NREC developed this model from an analysis formulated by Culick in the manner outlined above. The NREC model comprises two computer programs (HLMHLT and REFINE). HLMHLT calculates approximate oscillatory

---

*Rocketdyne has developed a capability for using the NREC model as a result of a subcontract to the General Electric Company for work on contract F33615-71-C-1742, Augmentor Combustion Stability Investigation. Rocketdyne's principal role has concerned analytical modeling at the driving processes.

pressure distributions and the corresponding frequencies as solutions to the Helmholtz equation (time independent form of the wave equation) and without considering combustion, i.e., it solves for ϕ_N and k_N from Eq.18 and 19, usually with admittance-type boundary conditions without considering combustion. REFINE calculates the frequencies and damping coefficients through a first-order correction for combustion effects. This model can be used to predict the stability of longitudinal and radial modes as well as the tangential modes described by the Priem model. In principle the model can also describe an acoustic cavity or liner but the description is much less accurate than the cavity damping model. The required input to the HLMHLT model includes:

- Chamber dimensions
- Average sound velocity and gas density
- Nozzle acoustic admittance
- Steady flow Mach number at nozzle entrance

The output from this program (approximate frequencies, damping coefficients, and pressure and velocity distributions) are used in REFINE. In addition, the input to REFINE includes:

- A series of coefficients representing the oscillatory combustion
- Steady flow velocity distribution

These combustion coefficients may be calculated from models for the spray combustion. The REFINE program predicts the damping coefficients for each mode corresponding to the operating conditions.

The combustion energy release rate is approximated in the NREC model by an exponentially decaying function (with axial position). Employing this assumption, the time averaged energy release rate becomes:

$$\bar{\dot{e}}_V = \bar{\rho}\frac{\bar{E}}{\bar{\tau}}\, e^{-z/\bar{u}\,\bar{\tau}} \tag{24}$$

while the oscillatory energy release rate is represented by:

$$\begin{aligned} \tilde{e}_V = \bar{\dot{e}}_V \Bigg\{ & \frac{\tilde{\rho}}{\bar{\rho}} + \frac{\tilde{E}}{\bar{E}} - \frac{\tilde{\tau}}{\bar{\tau}} + \int_0^z \frac{\tilde{\tau}}{\bar{\tau}}\left(r,\ \theta,\ \xi,\ t - \frac{z}{\bar{u}} + \frac{\xi}{\bar{u}}\right)\frac{d\xi}{\bar{u}\bar{\tau}} + \\ & \int_0^z \frac{\tilde{u}_z}{\bar{u}}\left(r,\ \theta,\ \xi,\ t - \frac{z}{\bar{u}} + \frac{\xi}{\bar{u}}\right)\frac{d\xi}{\bar{u}\bar{\tau}}\Bigg] \end{aligned} \tag{25}$$

The oscillatory energy content (E) and the oscillatory time delay (τ) are related to the pressure and velocity fluctuations through following combustion coefficients:

$$\frac{\widetilde{E}}{\overline{E}} = C_{2z}\frac{\widetilde{u}_z}{\overline{u}} + C_{2\theta}\frac{\widetilde{u}_\theta}{\overline{u}} + C_{2r}\frac{\widetilde{u}_r}{\overline{u}} + C_3\frac{\widetilde{p}}{\overline{p}} + C_4\left(\frac{\widetilde{u}_z}{\overline{u}}\right)_{inj} + C_5\left(\frac{\widetilde{p}}{\overline{p}}\right)_{inj} \tag{26}$$

$$\frac{\widetilde{\tau}}{\overline{\tau}} = C_1\frac{\widetilde{p}}{\overline{p}} + C_6\left(\frac{\widetilde{u}_z}{\overline{u}}\right)_{inj} \tag{27}$$

In the original model formulation, droplet vaporization was assumed to be the controlling mechanism for driving an instability, with the vaporization rate being assumed to depend only on the relative droplet Reynolds number. Recent calculations (Ref. 43) have shown that this assumption can lead to substantial errors with high-frequency instabilities.

Method of Evaluating Combustion Coefficients

The mathematical formulation used in the NREC program results in a linear stability model (i.e., the model formulation and solution are independent of the pressure amplitude). From experimental data, the stability characteristics of a rocket engine are known to be dependent upon the instability pressure amplitude. Therefore, to allow for these nonlinearities to some extent and to analyze rocket engines using the NREC program,the combustion coefficients, which appear in the oscillatory energy release rate equation, are considered functions of the pressure amplitude.

According to the Rayleigh principle, maximum oscillatory driving effect is obtained when an unsteady combustion process (energy addition) occurs in phase with, and in a region of, oscillating pressure. However, the overall combustion process comprises numerous localized, and often superimposed, combustion-related processes distributed throughout the chamber. Any of these processes may drive or supress a resonance, depending upon relative location and sensitivity to the local pressure variation.

A measure of the extent to which the combustion process can reinforce an acoustic oscillation is the response factor which is defined so that it is compatible with the Rayleigh criterion and is related to the local perturbations (Ref. 43). The nonlinear response factor for an unspecified parameter W is defined as:

$$\mathscr{R}_W = \frac{\int_0^{2\pi} (\widetilde{W}\widetilde{p}/\overline{W}\overline{p})\ d(\omega t)}{\int_0^{2\pi} \left[\mathrm{Re}(\widetilde{p}/\overline{p})\right]^2 d(\omega t)} \tag{28}$$

where $\widetilde{W}$ is any oscillatory source of mass or energy and:

$$\widetilde{W} = W - \overline{W} \tag{29}$$

The time averaged rate, $\overline{W}$, is given by:

$$\frac{\overline{W}}{W_o} = \int_o^{2\pi} \frac{W}{W_o} \frac{d(\omega t)}{2\pi} \tag{30}$$

For linear analysis of combustor instability, the response factor can be used directly to couple the combustion process to the gas dynamics. In the linear case, where all oscillations are sinusoidal, the relationship

$$\widetilde{W}/\overline{W} = \mathscr{R}_w (\widetilde{p}/\overline{p})$$

fully specifies the coupling. However, when oscillatory pressure levels become sufficiently large, often at a relative low amplitude, nonlinear effects (wave distortion) become important. Further, shock wave-type behavior in either the tangential or longitudinal modes has been observed in which the nonlinearity of the gas dynamic oscillations is clearly important. To analyze the wave distortion problem, the oscillatory pressure used in the calculation of the response factor has been assumed to be described by the form (see Ref. 44):

$$\text{Re}\left\{ \widetilde{p}/\overline{p} \right\} = \sum_n p_1{}^n \cos (n\omega t) \tag{31}$$

where p_1 is defined in terms of the peak-to-peak pressure amplitude by $(n \to \infty)$:

$$\frac{\widetilde{p}_{max} - \widetilde{p}_{min}}{\overline{p}} = \frac{2p_1}{1-p_1{}^2} \tag{32}$$

For low amplitudes the corresponding wave shape is sinusoidal while for large amplitudes the pressure wave shape approaches a steep fronted shock-type form.

Through the use of the response factor defined by Eq. 28, the combustion coefficients for the NREC program can be evaluated as a function of the pressure amplitude (Ref. 45).

Evaluation of Combustion Coefficients for Spray Combustion

Theories of droplet combustion are available that may be used to evaluate the extent of coupling between droplet burning rate and local pressure and velocity fluctuations. In general, droplet burning is enhanced by increased turbulence levels or by periodic directional variations in velocity, because droplets are relatively heavy and resist following gas streamlines. The overall process is controlled largely by heat transfer to the droplet and mass transfer away from the droplet, which are, in turn, influenced by the dynamics of the droplet relative to its gaseous environment. The droplet vaporization rate may be expressed as (see Ref. 46):

$$\dot{w}_{VAP} = \frac{6\rho_s \, z k_g \, Nu_H}{\rho_\ell D_d{}^2 \, c_{pv}} \tag{33}$$

$$z \equiv \frac{c_{pv}\ Nu_M\ p\ MW_v \mathscr{D}_v}{k_g\ Nu_H\ R_u\ T_f}\ \ell n \left(\frac{p}{p-p_v}\right) \tag{34}$$

$$Nu_H = 2.0 + 0.6\ Pr^{1/3} \left\{\frac{\rho D_d}{\mu_g} \left|\vec{u}_g - \vec{u}_d\right|\right\}^{1/2} \tag{35}$$

The equations used to represent the spray combustion are actually for a single vaporizing material but the properties and energy release profiles that are used pertain to bipropellant combustion.

The droplet mass continuity equation is:

$$\dot{w}_{VAP} = -\frac{d}{dz}\left(\rho_s\ u_{zd}\right) \tag{36}$$

Substituting Eq. 33 into Eq. 36 and integrating yields the droplet density as a function of location. From this density distribution, the energy release rate per unit volume may be obtained, i.e.:

$$\dot{e}_v = \frac{\rho E}{\tau}\ e^{-\int_0^z dz/u_z \tau} \tag{37}$$

where the time delay and the energy content are:

$$\tau \equiv \frac{\rho_\ell\ D_d^{\ 2}\ c_{pv}}{6\ z\ k_g\ Nu_H} \tag{38}$$

$$E \equiv \Delta H_{COMB}\ \frac{\dot{w}_d(z=0)}{\dot{w}_g} \tag{39}$$

Equations 37, 38, and 39 may be expanded into time averaged and oscillatory parts. The first of these is the same as that discussed previously. The latter equations become:

$$\frac{\tilde{\tau} + \tau'}{\tau_o} = \frac{\tau}{\tau_o} = \frac{z_o}{\bar{z}}\ \frac{Nu_{HO}}{\overline{Nu}_H} \left\{1 - \frac{\tilde{z}}{\bar{z}} - \frac{\widetilde{Nu}_H}{\overline{Nu}_H}\right\} \tag{40}$$

$$\frac{\bar{E} + \tilde{E}}{E_o} = \frac{E}{E_o} = \left\{1 - \frac{\tilde{u}_z}{\bar{u}} - \frac{\tilde{\rho}}{\bar{\rho}}\right\} \tag{41}$$

where τ_o and E_o refer to steady-state (rather than time averaged) conditions and:

$$\overline{Nu}_H = 2.0 + 0.6\ Pr_o^{\ 1/3}\ Re_o^{\ 1/2} \left\{ \overline{F}_\rho^{\ 4} \left(\frac{\Delta u_z}{c_o} \right)^2 + \overline{F}_u^{\ 4} \right\}^{1/4} \tag{41}$$

$$\frac{\widetilde{Nu}_H}{\overline{Nu}_H} = \frac{\left(\dfrac{\overline{Nu}_H - 2}{\overline{Nu}_H} \right) \left[\overline{F}_\rho^{\ 4} \left(\dfrac{\Delta \overline{u}_z}{c_o} \right)^2 \left(\dfrac{\widetilde{F}_\rho}{\overline{F}_\rho} \right) + F_u^{\ 4} \dfrac{\widetilde{F}_u}{\overline{F}_u} \right]}{\left[\overline{F}_\rho^{\ 4} \left(\dfrac{\Delta \overline{u}_z}{c_o} \right)^2 + \overline{F}_u^{\ 4} \right]} \tag{42}$$

$$Re_o \equiv \frac{\rho_o D_d c_o}{\mu_o} \tag{43}$$

$$F_u \equiv \left(\frac{\rho}{\rho_o} \right)^{1/2} \left| \frac{\widetilde{u}_z}{c} \right|^{1/2} \tag{44}$$

$$F_u = \mathscr{R}_{F_u}\ \overline{F}_u \left(\frac{\widetilde{p}}{\overline{p}} \right) \tag{45}$$

$$F_\rho = \left(\frac{\rho}{\rho_o} \right)^{1/2} \tag{46}$$

$$F_\rho = \mathscr{R}_{F_\rho}\ \overline{F}_\rho \left(\frac{\widetilde{p}}{\overline{p}} \right) \tag{47}$$

By comparing the preceding equations with the NREC oscillatory time delay and energy content equations, the combustion coefficients may be identified as:

$$C_1 = -\left(\mathscr{R}_z + \mathscr{R}_{Nu_H} \right)$$

$$C_{2z} = -1,\ C_{2r} = C_{2\theta} = 0$$

$$C_3 = -\frac{1}{\gamma},\ C_4 = C_3 = C_6 = 0 \tag{48}$$

where

$$\mathscr{R}_{Nu_H} \equiv \frac{\widetilde{Nu}_H / \overline{Nu}_H}{\widetilde{p} / \overline{p}}$$

The heat blockage term, z shown in the equations above is related to the combustion gas and liquid vapor properties by Eq. 34. This blockage term depends on the oscillatory droplet temperature because the vapor pressure (p_v) at the droplet surface is related to the droplet temperature. For a single droplet, the heating rate may be described by (see Ref. 46):

$$\frac{dT_d}{dt} = \frac{6k_f}{D_d^{\,2}} \frac{z\ Nu_H}{\rho_\ell\ c_{pd}} \left\{ \frac{T_g - T_d}{e^z - 1} - \frac{\Delta H_v}{c_{pv}} \right\} \tag{49}$$

Assuming that, at steady-state conditions,

$$\left(\frac{dT_d}{dt}\right)_o = 0 \tag{50}$$

and

$$\tilde{p}_v/\bar{p}_v = \mathscr{R}_{pv}\ (\tilde{p}/\bar{p}) \tag{51}$$

etc., for the other variables, the time averaged solution to the preceding equations gives:

$$\bar{z} \simeq z_o = \ell n \left\{ 1 + c_{pv}\ (T_g - T_d)/\Delta H_v \right\} \tag{52}$$

and the oscillatory solution gives:

$$\mathscr{R}_z = -\beta_z \left(\frac{1 - iA_c}{1 + A_c^{\,2}} \right) \tag{53}$$

where

$$\beta_z = \left[\frac{p_{vo}}{p_o - p_{vo}} \right] \Big/ \ell n \left(\frac{p_o}{p_o - p_{vo}} \right)$$

$$A_c = \frac{z_o\ e^{z_o}}{\left(e^{z_o} - 1\right)^2} \left(\frac{c_{pv}}{c_{pd}} \right) \frac{\beta_z \xi}{\omega_o \bar{\tau}} \left(\frac{T_{go} - T_{do}}{T_{do}} \right)$$

and

$$\xi = d\ \ell n\ p_v / d\ \ell n\ T_d$$

Examination of the real part of the oscillatory blockage term indicates that the real part of the response factor corresponding to this term will always be negative and that its magnitude will increase as the frequency of oscillation increases. Combining the above results with

$$\frac{\tau}{\bar{\tau}} \sim -\left(\mathscr{R}_z + \mathscr{R}_{Nu_H} \right) \left(\frac{\tilde{p}}{\bar{p}} \right) \tag{54}$$

and noting that the response factor for the Nusselt number is always positive (Ref. 43) lead to the conclusion that the response factor for the time delay will be negative for low frequencies and positive for high frequencies.

The foregoing equations have been used to calculate the combustion·coefficents. Based on information given in Ref. 47, β has been assumed to be equal to 1.5. The response factor has been evaluated with the velocity being assumed to be described by:

$$\tilde{u}_g = \frac{c}{\gamma} \sum_n p_1{}^n \cos (n\omega t-\theta) \tag{55}$$

where θ is the phase angle between the velocity and pressure. When θ is zero, the velocity and pressure are in phase, and traveling wave properties are simulated. For standing acoustic modes, the velocity and pressure are out of phase, which corresponds to θ = 90 degrees.

The steady-state time delay (z_0) has been determined by curvefitting results from the steady-state combustion model calculations.

NREC MODEL CALCULATIONS

The NREC model was used to predict the stability characteristics corresponding to some of the same engine conditions that were analyzed with the Priem-type model. The combustion coefficients were calculated as described above. No acoustic cavity effects were considered at this stage. The nozzle admittances were calculated separately and input to the program.

Nozzle admittances were calculated with an adaptation of the computer program described by Bell and Zinn (Ref. 48) which is based on the Crocco theory. Typical calculated admittance curves are shown in Fig. 7, which pertain to the first tangential mode and first tangential/longitudinally coupled modes. The real part of the predicted nozzle admittance is positive at high frequencies but negative at low frequencies. The negative real components of the admittance implies a driving effect which, presumably arises from a conversion of steady-flow energy into oscillatory energy. The nozzle also influences stability through the steady flow, which causes a convection of acoustic energy out of the chamber. Because of this convective effect, the net effect of the nozzle is expected to be a stabilizing one even at low frequencies.

The importance of allowing for oscillations in droplet temperature was investigated to determine whether or not this effect should be included in subsequent calculations. The effect arises through the heat blockage factor, z, discussed earlier. Stability calculations were made for two chamber sizes. The results are shown in Fig. 8 , which show the variation of predicted logarithmic decrements (damping coefficient divided by frequency) with the instability amplitude (peak to peak). Negative logarithmic decrements correspond to growing oscillations or unstable conditions. Apparently the importance of this droplet temperature effect is greatest at high frequencies (i.e., the 2.0-inch-radius chamber) and at this condition the effort is significant. Therefore, the effect was included in all subsequent calculations.

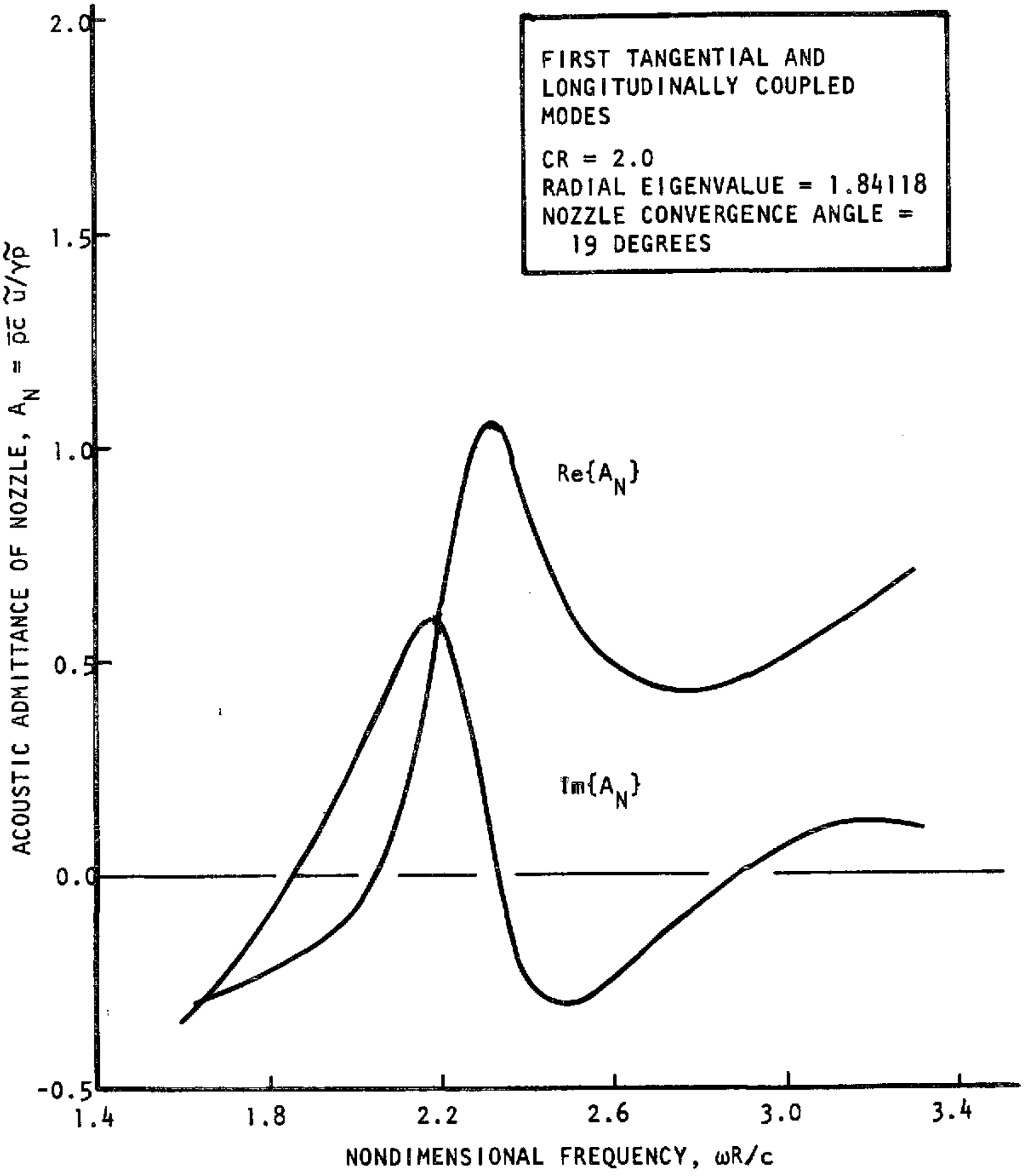

Figure 7. Predicted Nozzle Admittance for First Tangential and Longitudinally Coupled Modes

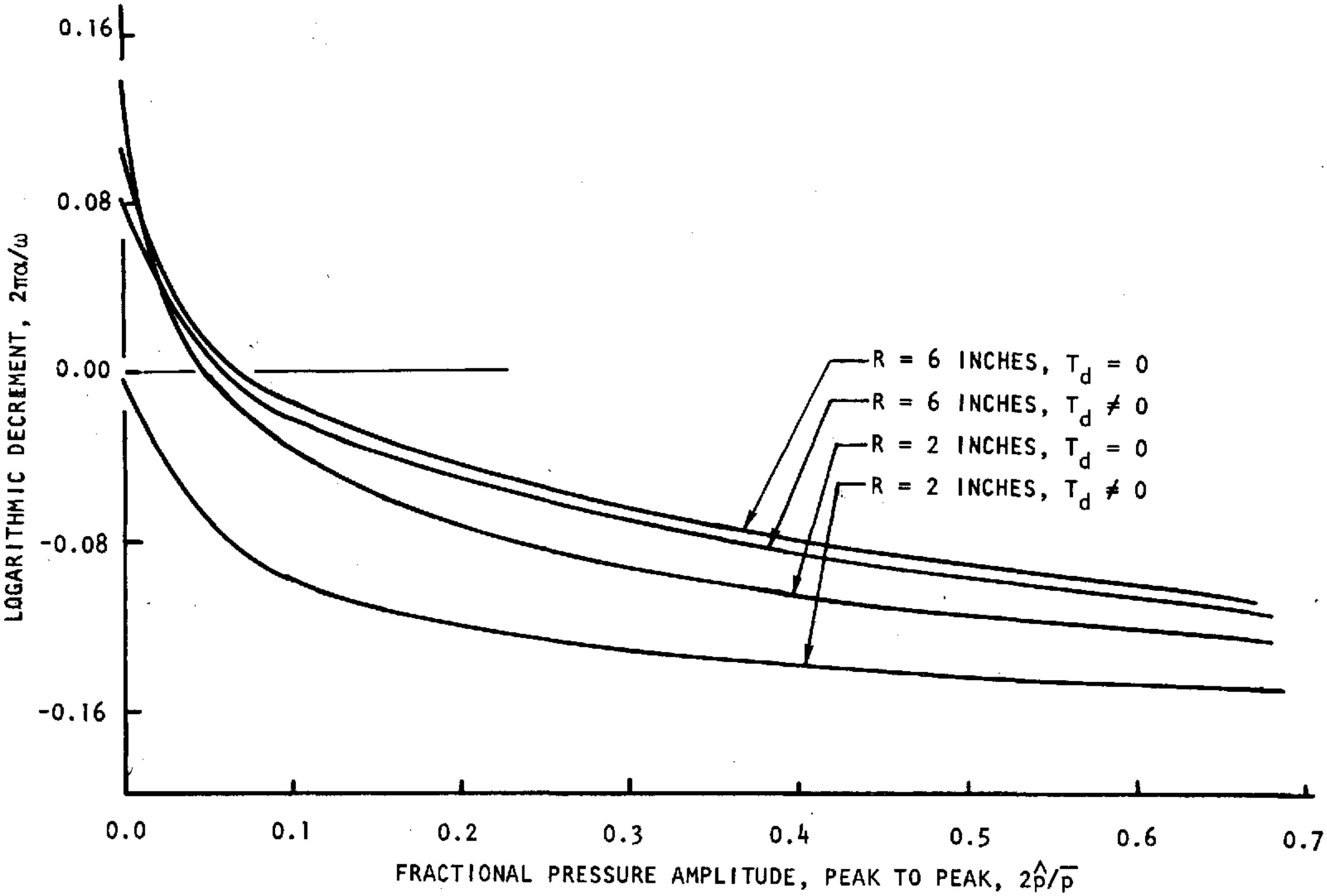

Figure 8. Predicted Oscillatory Decay Rates Showing the Effect of Droplet Temperature Oscillation

Results from a set of stability calculations for the first tangential mode in three chamber sizes and with two droplet sizes are shown in Fig. 9 and 10. In each case a critical amplitude is shown above which an instability is predicted the critical amplitude being that corresponding to a logarithmic decrement of zero. This critical amplitude, on a zero-to-peak rather than a peak-to-peak basis, corresponds to the Priem stability index.

Results from the NREC model analysis are summarized in Fig. 11 through 13, which show the variation of this critical pressure amplitude (zero-to-peak) with dropsize, dropsize ratio, and chamber radius. Corresponding curves from the Priem-type analysis are also shown. Some of the results from the NREC model analysis show a maximum stability index with increasing dropsize. This maximum arises because the time average combustion effeciency drops with increasing dropsize, which increases the available energy and worsens stability. The reduction in efficiency causes E, the energy content (Eq. 34), to increase, thus making more energy available for driving an instability. This effect will not occur if the combustion efficiency is 100 percent. It is not considered in the Priem-type analysis as usually done. The results show a worsening of stability with increasing chamber radius and, generally, an improvement with increasing dropsize.

The comparison of results from the NREC model analysis with those from the Priem-type analysis (Fig. 11 through 13) shows substantial differences in the magnitude of the critical pressure amplitude corresponding to the stability limit. Moreover, as noted above, the Priem-type results do not show the maximum that appears in the NREC-type results. However, there are also major differences in the methods of analysis used in these models and, therefore, substantial differences in the results are not surprising. Nonetheless, the results show qualitatively similar trends, which is encouraging.

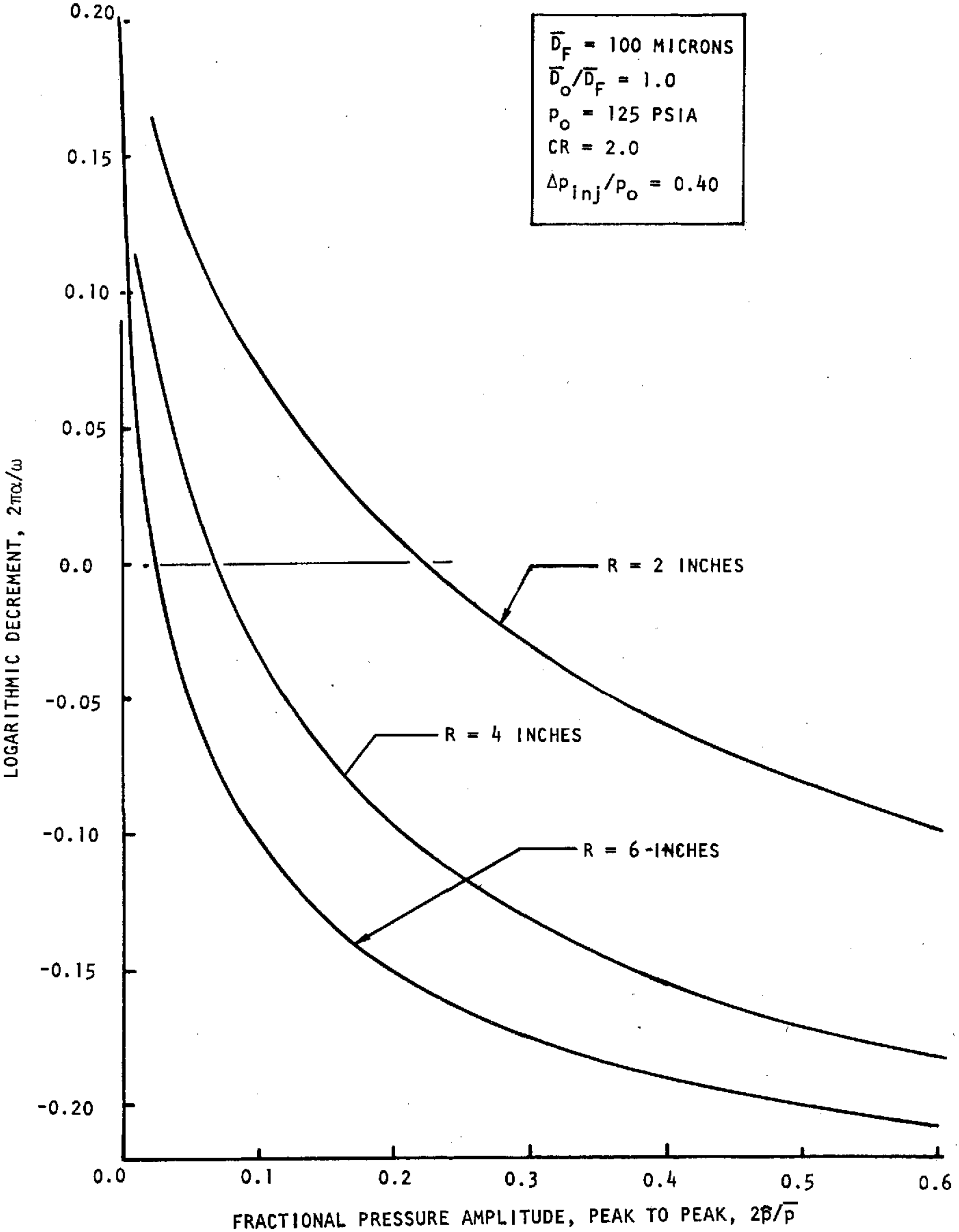

Figure 9. Predicted Oscillatory Decay Rates for $\overline{D}_F$ = 100 Microns

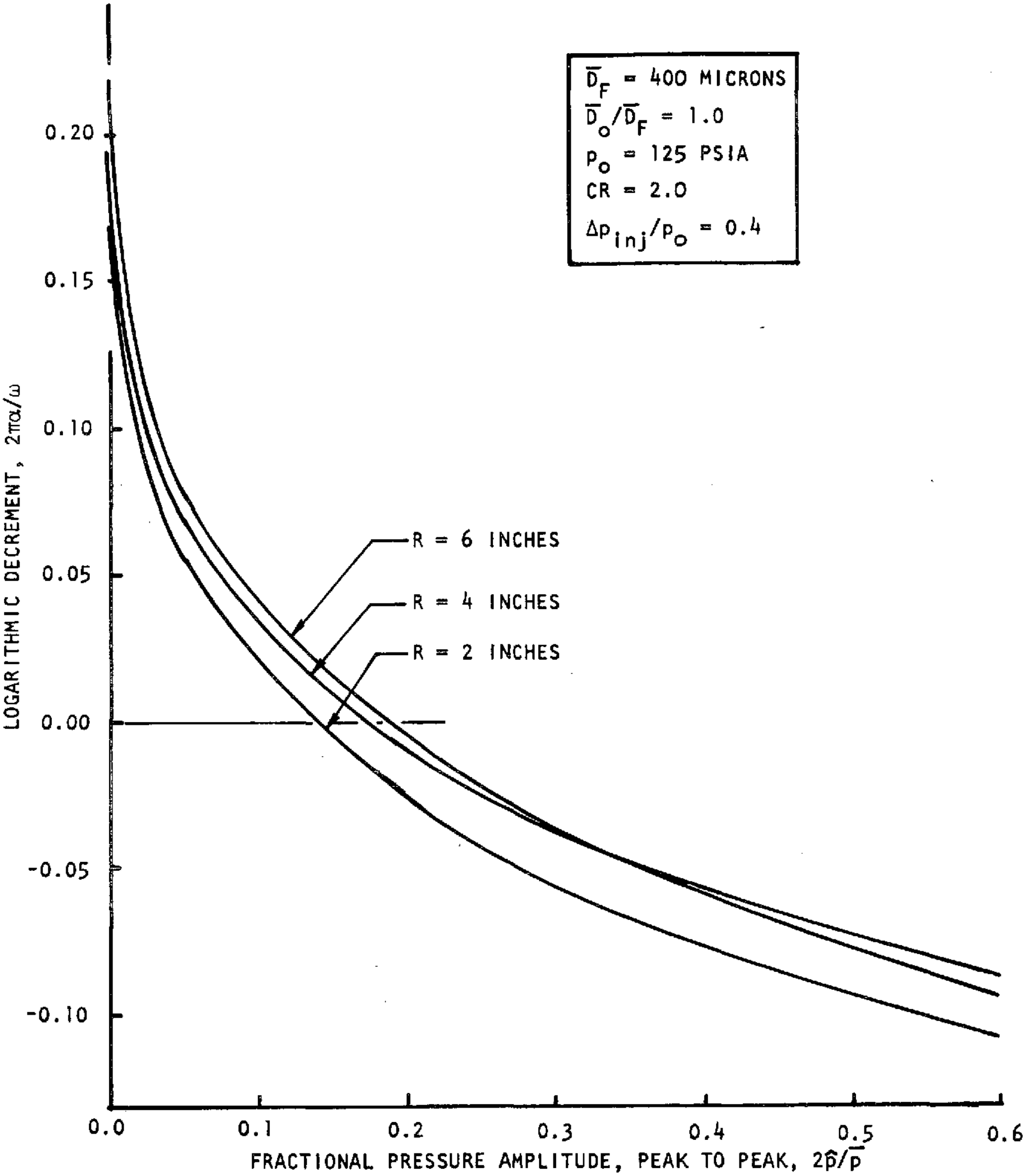

Figure 10. Predicted Oscillatory Decay Rates for $\overline{D}_F$ = 400 Microns

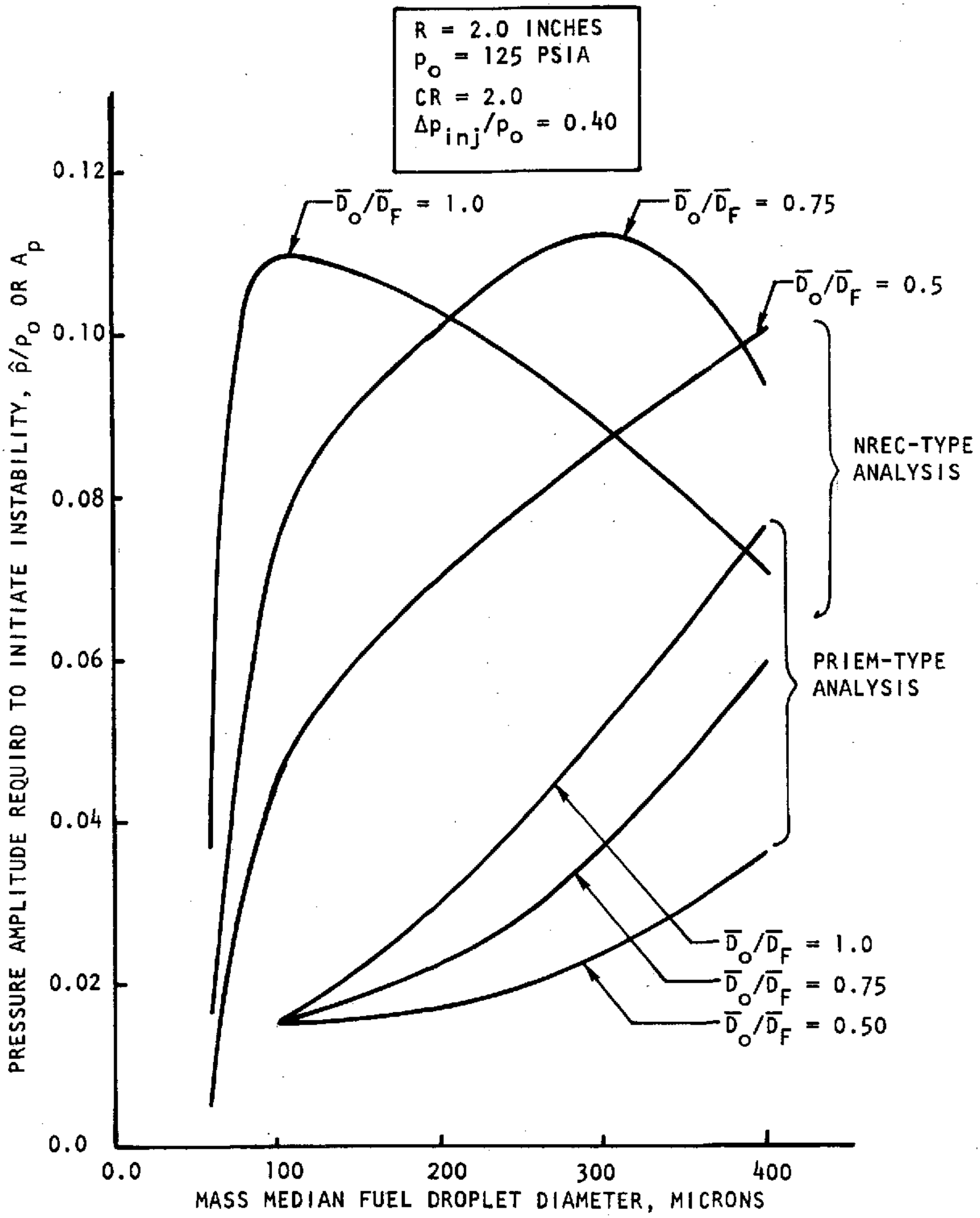

Figure 11. Predicted Stability Limit Amplitudes for R = 2.0 Inches

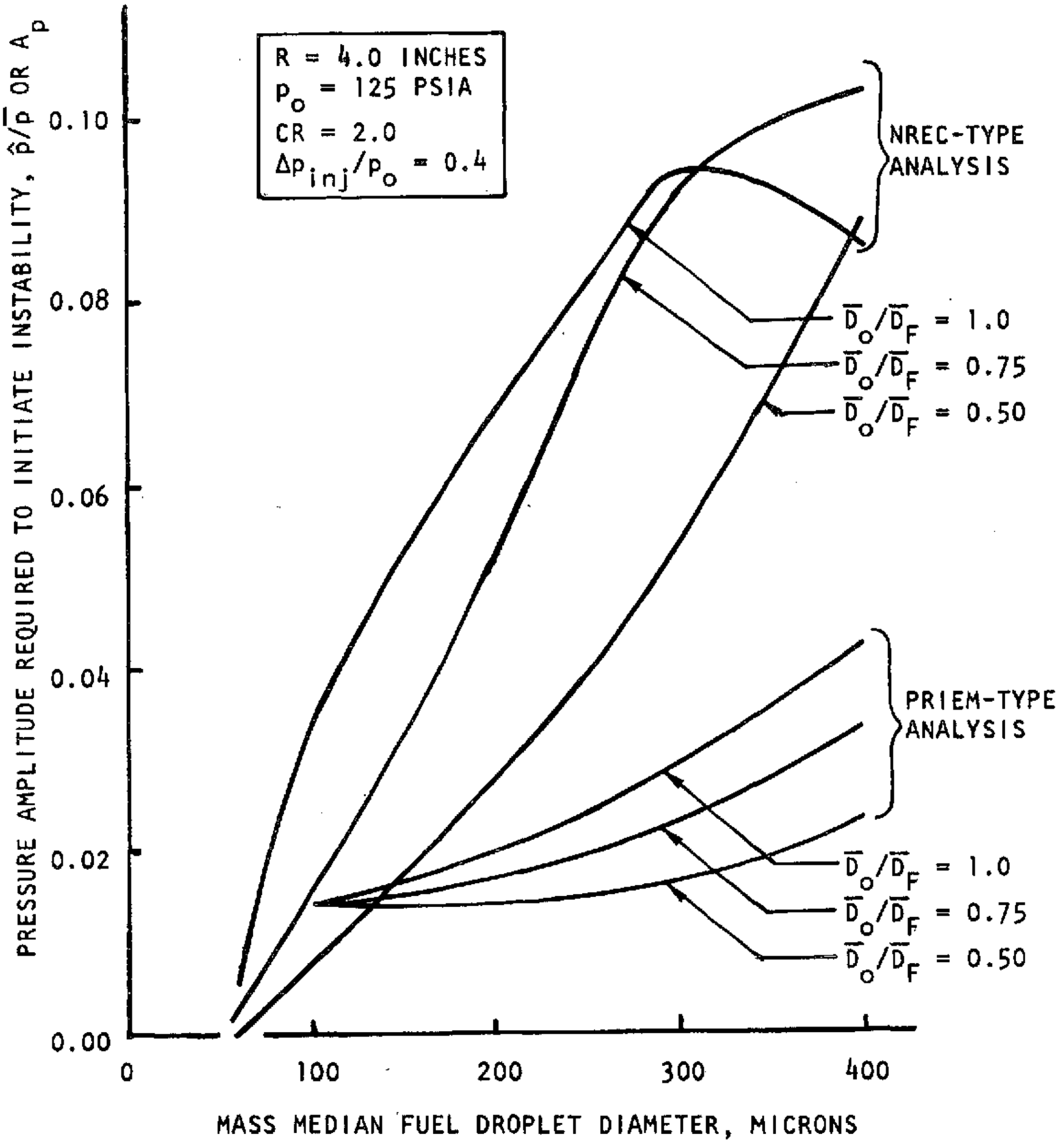

Figure 12. Predicted Stability Limit Amplitudes for R = 4.0 Inches

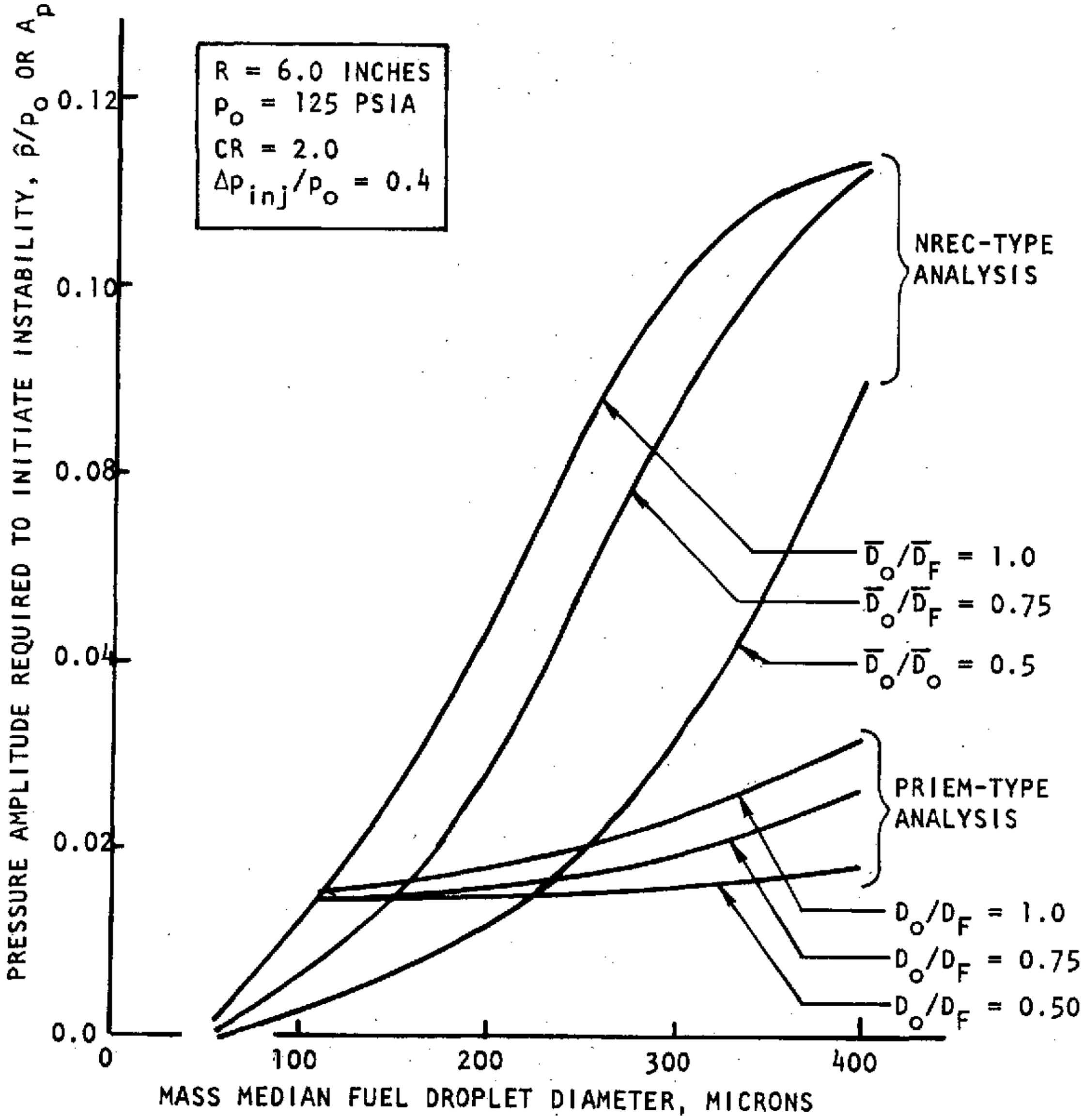

Figure 13. Predicted Stability Limit Amplitudes for R = 6.0 Inches

GENERALIZED CAVITY DAMPING MODEL

A generalized cavity damping model, based on the quasi-linear approach described earlier, has been formulated and the preliminary development completed. With this model, approximate solutions are obtained to restrictive forms of the inhomogeneous wave equation and boundary conditions (Eq. 16 and 17). The combustion source terms were represented in the manner described previously for the NREC model. For the vaporization limited process, the source may be written as:

$$\tilde{e} = \bar{\rho}\frac{\bar{E}}{\bar{\tau}}\, e^{-\int dz/\bar{u}\,\bar{\tau}} \left\{ \mathscr{R}_s \frac{\tilde{p}}{\bar{p}} - \int_o^z \mathscr{R}_s \frac{\tilde{p}}{\bar{p}} \left(t - \frac{z}{\bar{u}} + \frac{\xi}{\bar{u}}\right) \frac{d\,\xi}{\bar{u}\,\bar{\tau}} - \frac{\tilde{u}_z}{\bar{u}} + \int_o^z \frac{\tilde{u}_z}{\bar{u}} \left(t - \frac{z}{\bar{u}} + \frac{\xi}{\bar{u}}\right) \frac{d\xi}{\bar{u}\,\bar{\tau}} \right\} \qquad (56)$$

where

$\mathscr{R}_s = \mathscr{R}_z + \mathscr{R}_{Nu}$. This expression replaces all of the source terms shown in Eq. 16, i.e., $\tilde{\mathscr{P}} = R\tilde{e}/C_v$.

Development of this cavity damping model has been approached on an incremental basis with individual effects being added one at a time. At present, three kinds of effects have been introduced: (1) a uniform steady flow, (2) a nozzle admittance, and (3) pressure-coupled combustion response. However, the steady flow contribution at the acoustic cavity has been neglected. (This is probably small for a cavity located adjacent to the injector.) The effects of gradients in the steady flow, velocity coupled combustion, droplet drag, and steady flow at the cavity must be added at a later time. Therefore, at present the generalized cavity model is based on solution of the following inhomogeneous wave equation:

$$(\nabla^2 + k^2)\,\tilde{p} = 2jk\bar{M}\,\frac{\partial\tilde{p}}{\partial z} - \bar{M}^2\,\frac{\partial^2 p}{\partial z^2} - h_o\, e^{-z/\lambda}\left[\tilde{p} - \int_o^z \tilde{p}\,(r,\,\theta,\,z')\; e^{-j\beta\,\frac{z-z'}{\lambda}}\,\frac{dz'}{\lambda}\right] \equiv -\,S(r;\,\tilde{p}) \qquad (57)$$

where a time dependence of the form $e^{j\beta t}$ has been assumed ($\beta = \omega + j\alpha$). The first two terms on the right-hand side of Eq. 57 correspond to the uniform steady flow in the axial direction, where $\bar{M} = \bar{u}/\bar{c}$. The last expression arises from the pressure-coupled combustion source terms, where:

$$h_o = \frac{\bar{\rho}\,\bar{E}}{\bar{\tau}}\,\mathscr{R}_s$$

and

$$\lambda = \bar{u}\,\bar{\tau}$$

Equation 57 has been solved subject to the boundary conditions

$$\vec{N} \cdot \nabla\tilde{p} = 0 \qquad (58)$$

at rigid walls, including the injector wall and

$$\frac{\vec{N} \cdot \nabla\tilde{p}}{\tilde{p}} = -jky \qquad (59)$$

at the acoustic cavity interface where y is the specific acoustic admittance of the cavity. Thus, the effect of the steady flow at the cavity has been neglected. The real part of the specific admittance for the boundary condition at the nozzle entrance includes the steady-flow effects and may be written as:

$$\vec{N} \cdot \nabla\tilde{p} = -jk \left[A\,\tilde{p} + \frac{\overline{M}}{k^2} \; \frac{\partial^2 \tilde{p}}{\partial z^2} \right] \qquad (60)$$

where $A = \gamma\,\overline{p}\,\vec{N} \cdot \vec{u}/\tilde{p}\,\overline{c}$, the specific nozzle admittance. The inhomogeneous Helmholtz equation has been solved by conversion to an integral equation which was solved approximately by an iterative variational technique. The method of solution is similar to that used previously for the no-flow, no-combustion case.

INTEGRAL EQUATION FORMULATION

The integral equation is developed in terms of the following Helmholtz Green's function $G\ (\vec{r}|\vec{r}\ )$ satisfying:

$$(\nabla^2 + k^2)\ G\ (\vec{r}|\vec{r}_o) = -\delta(\vec{r}-\vec{r}_o) \qquad (61)$$

$$\vec{N} \cdot \nabla G\ (\vec{r}|\vec{r}_o) = 0$$

An eigenfunction expansion was used for the Green's function, G. The normal modes of a closed cylinder are employed for this expansion, i.e.:

$$\nabla^2\,\phi_N + \eta_N^{\ 2}\,\phi_N = 0 \qquad (62)$$

$$\vec{N} \cdot \nabla\phi_N = 0$$

$$\phi_N = J_m(\alpha_{m\ell}\ r/r_w)\ \cos\frac{q\pi z}{L} \begin{cases} \cos\ m\ \theta \\ \sin\ m\ \theta \end{cases}$$

$$\eta_N^{\ 2} = \alpha_{m\ell}^{\ 2}/r_w^{\ 2} + q^2\pi^2/L^2$$

where N represents the three indices m, ℓ, q. An expression for the Green's function may be readily obtained in terms of these functions, it being:

$$G(\vec{r}|\vec{r}_o) = \sum \frac{\phi_N(\vec{r})\ \ \phi_N(\vec{r}_o)}{\Lambda_N\left(\eta_N^{\ 2} - k^2\right)} \tag{63}$$

$$\Lambda_N \equiv \Lambda_m^{\theta}\,\Lambda_{m\ell}^{(r)}\,\Lambda_q^{(z)} = \int \phi_N^{\ 2}(\vec{r})\,dV$$

$$\Lambda_m^{(\theta)} = \int_o^{2\pi} d\phi \begin{Bmatrix}\cos^2\\ \sin^2\end{Bmatrix}\begin{matrix}m\phi\\ m\phi\end{matrix} = \begin{cases}\pi & m \neq 0\\ 2\pi & m=0\ \ (\cos\ m\phi\ \ \text{only})\end{cases}$$

$$\Lambda_{m\ell}^{(r)} = \int_o^{r_w} r\ dr\ J_m^{\ 2}\left(\frac{\alpha_{m\ell}r}{r_w}\right) = \frac{\alpha_{m\ell}^{\ \ 2} - m^2}{\alpha_{\ m\ell}^{\ 2}}\ J_m^{\ 2}(\alpha_{m\ell})$$

$$\Lambda_q^{(z)} = \int_o^L dz\ \cos^2\ \frac{q\pi z}{L} = \begin{cases}L/2 & q \neq 0\\ L & q = 0\end{cases}$$

Through use of this Green's function, the inhomogeneous wave equation and boundary condition may be converted to an integral equation (Ref. 49, page 321).

$$\tilde{p}(\vec{r}) = \int G(r|r_o)\ \ S(r_o;\ \tilde{p})\ dV_o\ +$$
$$+\ \int G(r|r_o)\ \vec{N}\cdot \nabla\tilde{p}^2(r_o)\ dS_o \tag{64}$$

where $S(r_o;\ \tilde{p})$ represents the inhomogeneous term in the wave equation, the $N \cdot \nabla\tilde{p}$ term is given by the boundary conditions, and the vector sign (→) has been suppressed on r and r_o for simplicity. This homogeneous integral is solved by an iterative-variational technique.

ITERATIVE-VARIATIONAL SOLUTION TECHNIQUE

The solution technique is similar to that used previously (Ref.50). Frequently with equations of this form, the integrals may be evaluated with an initial approximation for pressure to achieve an improved approximation for the pressure. Therefore, an iteration form of the expression is written as:

$$\tilde{p}^{(i+1)}(\vec{r}) = \int G(r|r_o)\ S(r_o;\ \tilde{p}^{(i)})\ dV_o\ +$$
$$\int G(r|r_o)\ \vec{N}\cdot \nabla\tilde{p}^{(i)}\ dS_o \tag{65}$$

Because an eigenfunction expansion was used for the Green's function, evaluation of the integrals leads to a series expression for the pressure in terms of the same eigenfunctions. Thus, from an approximation for $p^{(i-1)}$, an expression is obtained of the form:

$$p^{(i)}(\vec{r}) = \sum_{\ell,q} a^{(i)}_{\ell q}\, J_{\bar{m}}\left(\frac{\alpha_{\bar{m}\ell}\, r}{r_w}\right) \cos\frac{q\pi z}{L}\, \cos \bar{m}\, \phi \tag{66}$$

Evaluation of the integral expression gives an expression for $a^{(i+1)}_{\ell q}$ in terms of $a^{(i)}_{\ell q}$. The iteration is usually started with the eigenfunction corresponding to the mode of interest, i.e.:

$$a^{(o)}_{\ell q} = \begin{cases} 1.0 & \ell,q = \bar{\ell},\bar{q} \\ 0.0 & \ell,q \neq \bar{\ell},\bar{q} \end{cases} \tag{67}$$

The angular dependence drops out because the boundary conditions are uniform in the circumferential direction. At times, it is more convenient (if not necessary) to use the $a^{(i)}_{\ell q}$ from a simpler case as the starting point for a more complicated case, e.g., by tracking the solution as a parameter is incrementally changed.

Although it is possible, in principle, to use the iteration equation alone to solve for complex angular frequency, and determine stability, it is more efficient to develop a separate characteristic or eigenvalue equation. The variational approach has been used for this purpose.

Eigenvalue Equation

Successful use of a variational method depends to a large extent on the form of $S(r;\tilde{p})$ from the wave equation. The variational method described by Morse and Ingard (Ref. 49, page 561) has been used previously. By separating a particular term from the integral expression for pressure, the following equation is obtained:

$$\tilde{p}(\vec{r}) = -jk \int G_N(r|r_o)\, y(r_o)\, \tilde{p}(r_o)\, dS_o - \int G_N(r|r_o)\, S(r_o;\tilde{p})\, dV_o + \phi_N(r) \left\{ \frac{-jk \int \phi_N(r_o)\, y(r_o)\, \tilde{p}(r_o)\, dS_o + \int \phi_N(r_o)\, S(r_o;\tilde{p})\, dV_o}{\Lambda_N\left(\eta_N^2 - k^2\right)} \right\}$$

where (68)

$$G_N(r|r_o) = G(r|r_o) - \frac{\phi_N(r)\, \phi_N(r_o)}{\Lambda_N\left(\eta_N^2 - k^2\right)}$$

Because of the homogeneous form of the equation, an amplitude coefficient can be chosen for $\widetilde{p}$ such that the term in parentheses ( ) equals unity. Without changing the notation for pressure, this choice of amplitude gives:

$$\widetilde{p}(r) = \phi_N(r) - jk \int G_N(r|r_o)\, Y(r_o)\, \widetilde{p}(r_o) dS_o - \int G_N(r|r_o)\, S(r_o;\widetilde{p}) dV_o \tag{69}$$

$$\Lambda_N(\eta_N{}^2 - k^2) = -jk \int \phi_N(r_o)\, y(r_o)\, \widetilde{p}(r_o) dS_o + \int \phi_N(r_o)\, S(r_o;\widetilde{p}) dV_o \tag{70}$$

This expression for $\widetilde{p}$ clearly approaches the normal mode ϕ_N as y and S $(r;\widetilde{p})$ approach zero. Following Morse and Ingard by analogy, a functional is developed by multiplying Eq. 69 by $-jk \int y(r)\widetilde{p}(r) dS$ and then by $\int S(r;p)\, dV$ and adding the resultant expressions to Eq. 70 to obtain:

$$\begin{aligned}\Lambda_N(\eta_N{}^2 - k^2) = {} & 2\int \phi_N(r_o)\left[-jk\, y(r_o)\, p(r_o)\right] dS_o + \int \phi_N(r_o)\, S(r_o;\widetilde{p}) dV_o \; - \\ & \int \widetilde{p}(r_o)\left[-jk\, \widetilde{p}(r_o)\right] dS_o + \int [-jk\, y(r_o)\, \widetilde{p}(r_o)] \int G_N(r|r_o)\left[-jk\, y(r_o)\; ;(r_o)\right] dV_o\, dV \; + \\ & [-jk\, y(r_o)\, \widetilde{p}(r_o)] \int G(r|r_o)\, S(r_o;\widetilde{p}) dV_o dS - \int S(r;\widetilde{p})\, \widetilde{p}(r) dV \; + \\ & \int S(r;\widetilde{p}) \int G_N(r|r_o)[jk\, y(r_o)\, \widetilde{p}(r_o)]\, dS_o dV + \int S(r;\widetilde{p}) \int G(r|r_o)\, S(r_o;\widetilde{p}) dV_o dV\end{aligned} \tag{71}$$

By varying this equation, a characteristic equation may be obtained:

$$\begin{aligned}\delta[\Lambda_N(\eta_N{}^2 - k^2)] = {} & -2\int \delta S(r;\widetilde{p}) \left\{ \phi_N(r) - jk \int G_N(r|r_o)\, y(r_o)\, \widetilde{p}(r_o) dS_o \; - \right. \\ & \left. \int G_N(r|r_o)\, S(r_o\widetilde{p}) dV_o \right\} - \int S(r;\widetilde{p})\, \delta\widetilde{p} dV + \widetilde{p}(r)\, \delta S(r_o;\widetilde{p}) dV_o\end{aligned} \tag{72}$$

If the last two terms cancel, Eq. 72 is a variational implying Eq. 65. However, the last two terms cancel only for the special cases $S = \widetilde{p}(r)\; \overline{h}\; e^{-z/\lambda}$ and $-\overline{M}^2\, \partial^2\widetilde{p}/\partial z^2$ from the wave equation (Eq. 57) the latter case demanding restrictions on $\delta\widetilde{p}(r)$. The latter term is also usually dropped by order of magnitude arguments.

If only the term S $(r;p) = \widetilde{p}\, \overline{h}\; e^{-z/\lambda}$ is retained, an equation similar to that used previously is obtained (Ref. 50). With an approximation for pressure of the form $\widetilde{p} = A\widetilde{p}^{(i)}$, the variation may be performed to obtain:

$$\begin{aligned}& \int [-jk\, y(r)\, \widetilde{p}^{(i)}(r)] \left\{ \widetilde{p}^{(i)}(r) - \int G(r|r_o)\, [-jk\, y(r_o)\, \widetilde{p}^{(i)}(r_o)] dS_o \right. \\ & \left. \int G(r|r_o)\, S\,(r_o;\widetilde{p}^{(i)}) dV_o \right\} dS + \int S\,(r;\widetilde{p}^{(i)}) \left\{ \widetilde{p}^{(i)}(r) \; - \right. \\ & \left. \int G(r|r_o)\, [-jk\, y(r_o)\, \widetilde{p}^{(i)}(r_o)] dS_o - \int G(r|r_o)\, S(r;\widetilde{p}^{(i)}) \widetilde{d}V_o \right\} dV = 0\end{aligned} \tag{73}$$

This equation may be rewritten as:

$$\int(-jky\tilde{p}^{(i)})\left\{\tilde{p}^{(i)} - \tilde{p}^{(i+1)}\right\}dS + \int S\ (r;\tilde{p}^{(i)})\left\{\tilde{p}^{(i)} - \tilde{p}^{(i+1)}\right\}dV = 0 \tag{74}$$

The first term in this equation is the same as that developed previously to assess cavity effects alone (Ref. 50). Equation 74 has the interesting form of a weighted average of the residual, $\tilde{p}^{(i)} - \tilde{p}^{(i+1)}$, at the ith iteration. The weighting factor has surface contribution proportional to the wall admittance and a volume contribution proportional to the combustion coefficient. Unfortunately, the restriction on S(r;p) is undesirable.

An alternate derivation of an eigenvalue equation corresponding to Eq. 74 was found following Morse and Feshbach (Ref. 51). The derviation involved the use of adjoint solutions which could be specified for $S(r;\tilde{p}) = \bar{n}\ e^{-z/\lambda}$, but not in the more general cases. The additional complexity of adjoint functions and adjoint operators led to the abandonment of this approach in favor of a "least-squares" method.

"LEAST-SQUARES" DERIVATION OF EIGENVALUE EQUATION

Least-squares variational methods are described by M. Becker in his monograph (Ref. 51). The related approach used here differs in that the variational is not taken to be positive definite, which is the reason for the quotes on "least-squares." Consider the functional:

$$I = \int w(r)\left\{\mu\tilde{p} - M\ \tilde{p}\right\}^2 dV \tag{75}$$

where w(r) is a weighting function and the equation

$$\begin{aligned}\mu\tilde{p} &= M\tilde{p}\\ &= \int M(r,r_o)\ \tilde{p}(r_o)dV_o\end{aligned}$$

is a shorthand notation for the integral equation (Eq. 64). The quantity μ is an artificial eigenvalue. For arbitrary k, there will be discrete eigenvalues, $\mu(k)$. The desired eigenvalues correspond to inverting $\mu(k) = 1$ to obtain $k = k(\mu = 1)$. The variation of I is taken to include variations of the eigenvalue μ:

$$\begin{aligned}\delta I = {} & 2\ \delta\mu\int w(r)\ \tilde{p}(r)\left\{\mu\tilde{p}(r) - M\ \tilde{p}\right\}dV\ +\\ & 2\int\left\{\mu\tilde{p} - M\ \tilde{p}\right\}\left\{\mu\delta\tilde{p} - M\ \delta\tilde{p}\right\}dV\end{aligned} \tag{76}$$

This shows that $\delta I = 0$ when the integral equation (Eq. 64) is satisfied. With a trial function $\tilde{p}^{(i)}$, the variation of I with respect to μ implies

$$\int w(r)\ \tilde{p}^{(i)}(r)\left\{\mu\tilde{p}^{(i)}(r) - M\ \tilde{p}^{(i)}(r)\right\}dV = 0 \tag{77}$$

which a new eigenvalue equation for the cavity problem when $\mu = 1$ and w(r) is chosen. Rather than use the variation of I with respect to $\delta\tilde{p}$ to determine the coefficients $a_{\ell m}$ (Eq. 66), the iterative equation (Eq. 65) was used. Equation 77 holds for arbitrary M or S(r;p) and for arbitrary weighting functions, w(r). Thus, the eigenvalue equation is not unique. Different choices of weighting function will yield different eigenvalue estimates and, thus, affect the convergence rate in the iterative approach.

One choice of w(r) that is suggested by Eq. 73 is:

$$w(r) = h_o e^{-z/\lambda} + [-jky(r_o^s)]\,\delta(\vec{r} - \vec{r}_o^{\,s})dV_o \tag{78}$$

With this choice, Eq. 77 becomes:

$$\int[-jky(r)\,\tilde{p}^{(i)}(r)]\left\{\tilde{p}^{(i)}(r) - \tilde{p}^{(i+1)}(r)\right\} dV + \int S_h(r;p^{(i)})\left\{p^{(i)}(r) - p^{(i+1)}(r)\right\} dV = 0 \tag{79}$$

where μ has been set equal to unity. Equation 79 has the same form as Eq. 74 but this derivation shows that it holds for arbitrary S(r,p).

FORMULATION IN TERMS OF $a_{\ell q}^{(i)}$

The equations can be placed in a more convenient form for numerical solution by the series coefficients $a_{\ell q}^{(i)}$ of Eq. 66. In terms of these coefficients, Eq. 65 becomes:

$$a_{\ell q}^{(i+1)} = \frac{\sum_{\ell' q'} T_{\ell q,\ell' q'}\, a_{\ell' q'}^{(i)}}{\Lambda_{\bar{m}\,\ell q}\,(\eta^2_{\bar{m}\,\ell q} - k^2)} \tag{80}$$

where

$$\begin{aligned}
T_{\ell q,\ell' q'} = {} & (-jky)_{\text{CAVITY}}\, J_{\bar{m}}(\alpha_{\bar{m}\ell})\, J_{\bar{m}}(\alpha_{\bar{m}\ell'})\, I_{qq'} \; + \\
& (-jky)_{\text{NOZZLE}}\, \Lambda_{\bar{m}\ell}\, (-1)^{q+q'}\, \delta_{\ell\ell'} \; + \\
& (h_o L)\, \Lambda_{\bar{m}\ell}\, J_{qq'}(\lambda)\, \delta_{\ell\ell'} \; + \\
& (j\,2kM_o)\, \Lambda_{\bar{m}\ell}\, K_{qq'}\, \delta_{\ell\ell'} \; + \\
& (h_o L)\, \Lambda_{m\ell}\, \frac{\delta_{\ell\ell'}}{\left(\frac{q'\pi}{L}\right)^2 - \left(\frac{k}{\bar{\bar{M}}}\right)^2} \left(-\frac{jk}{\bar{M}\lambda}\right) \Bigg\{ J_{qq'}(\lambda) \; - \\
& \delta_{q'o}\, J_{qq'}\left(\frac{\lambda\bar{M}}{\bar{M} + jk\lambda}\right) \Bigg\} \; + \\
& (h_o L)\, \Lambda_{\bar{m}\ell}\, \frac{\delta_{\ell\ell'}}{\left(\frac{q\pi}{L}\right)^2 - \left(\frac{k}{\bar{\bar{M}}}\right)^2}\, \frac{1}{\lambda L}\, R_{qq'}(\lambda)
\end{aligned}$$

and

$$y_{\text{NOZZLE}} = A + \frac{\overline{M}}{k^2} \left(\frac{q'\pi}{L}\right)^2$$

$$I_{qq'} = \int_{w_s} \frac{dz}{L} \cos \frac{q\pi z}{L} \cos \frac{q'\pi z}{L}$$

where w_s denotes the slot width and:

$$J_{qq'}(\lambda) = \int_0^L e^{-z/\lambda} \cos \frac{q\pi z}{L} \cos \frac{q'\pi z}{L} \frac{dz}{L}$$

$$K_{qq'} = -q\pi \int_0^L \cos \frac{q\pi z}{L} \sin \frac{q'\pi z}{L} \frac{dz}{L}$$

$$R_{qq'}(\lambda) = -q\,\pi \int_0^L e^{-z/\lambda} \cos \frac{q\pi z}{L} \sin \frac{q'\pi z}{L} \frac{dz}{L}$$

Note that $R_{qq'}(\lambda = \infty) = K_{qq'}$. The terms in Eq. 80 can be associated with the corresponding terms in Eq. 65 via the coefficients, q, $\overline{M}$, $\overline{h}$, etc. The last two ($\overline{h}_o L$) expressions correspond to the combustion-convection integral term in Eq. 57. These two terms must be dropped in the computer program if the steady flow $\overline{M} = 0$ to avoid division by zero in the program. Analytically, these terms vanish when $\overline{M} = 0.0$.

This eigenvalue equation (Eq. 79) can be rearranged by direct substitution to obtain:

$$\sum_{\ell q, \ell' q'} a^{(i)}_{\ell q} T^{(M=0)}_{\ell q, \ell' q'} \left\{a^{(i)}_{\ell' q'} - a^{(i+1)}_{\ell' q'}\right\} = 0 \tag{81}$$

where the notation "M = 0" denotes that the steady flow terms have been deleted from $T_{\ell q, \ell' q'}$ in Eq. 80. The nozzle admittance term was retained. Equation 81 holds even when $\overline{M} \neq 0$, but when $\overline{M} = 0$, it can be rewritten as:

$$\sum_{\ell q} \Lambda_{\overline{m}\ell} \Lambda_q \left(\eta^2_{\overline{m}\,\ell q} - k^2\right) a^{(i)}_{\ell q} \left\{a^{(i+1)}_{\ell q} - a^{(i+2)}_{\ell q}\right\} = 0 \tag{82}$$

The essence of Eq. 82 is the residual $a^{(i)}_{\ell q} - a^{(i+2)}_{\ell q}$, which is weighted by $a^{(i)}_{\ell q}$ and some additional factors. Equation 82 was used as the basis for the computer program although the derivation is not rigorous for the case $\overline{M} \neq 0$. However, various modifications of Eq. 82 were tried successfully, e.g.:

$$\sum_{\ell q} a^{(i)}_{\ell q} \left\{a^{(i+1)}_{\ell q} - a^{(i+2)}_{\ell q}\right\} = 0 \tag{83}$$

and

$$\sum_{\ell q} a_{\ell q}^{(i+1)} \left\{ a_{\ell q}^{(i+1)} - a_{\ell q}^{(i+2)} \right\} = 0 \tag{84}$$

Equation 82 seemed to converge most rapidly. Attempts at "least-squares" derivation with a more general weighting function

$$I = \left\{ \mu p - M \tilde{p} \right\}_{r} w(r,r_o) \left\{ \mu\tilde{p} - M \tilde{p} \right\}_{r_o} dV \, dV_o = 0 \tag{85}$$

$$w(r,r_o) = \sum_{i,j} \phi_i(r) \, w_{ij} \, \phi_j(r_o)$$

did not yield Eq. 82. Equation 85 is perhaps more closely related to the method of weighted residuals (Ref. 52, page 10). Nevertheless, Eq. 80 and 82 have yielded the desired convergence in that additional iterations do not change the complex pressure distribution. These resulting solutions are considered to be very good approximations to solutions of the original partial differential (Eq. 57). Various factors, such as the truncation of the series expansion, Eq. 82, will affect the accuracy of the result.

COMPUTER RESULTS

A computer program was developed to solve the foregoing equations and was adapted from the previously developed cavity damping model. The computer subroutine used to calculate to acoustic impedance of the acoustic cavity was used without change. At present, the program is only capable of analyzing the first-tangential model, which was done to facilitate model development. Sufficient progress has been made to allow preliminary definition of the characteristics of the model predictions, but additional work is needed to generalize the model, fully characterize the predictions, and relate the model results to measured stability results.

The computer program has been checked to a large extent by comparison of computational results with analytical results from analytically solvable limiting cases. Also, comparisons have been made with results obtained with the previously developed model suppressing the new contributions in the generalized model. The two models are necessarily somewhat different because of the volume contribution included in the new model.

As noted previously, the model was developed and checked on an incremental basis. The results are discussed accordingly.

Acoustic Cavity

A comparison of results from the previous cavity model and from the generalized shows that they are essentially identical, although different series expressions and methods of calculation have been used. Some typical results are shown in Fig. 14.

As shown in Fig. 14, the mode splitting obtained with the previous model was also predicted with the generalized model. With the acoustic cavity, two modes are obtained in place of the normal first-tangential mode. The lower frequency mode approaches the normal chamber mode as the cavity becomes very small. The upper frequency mode approaches a quarterwave mode in the cavity as the cavity width becomes small; nonetheless, the chamber is fully involved in this oscillation for cavities wide enough to be useful for stabilization.

The damping associated with each of these modes has not been calculated beyond the crossover point between the two damping coefficient curves because only the most weakly damped mode is likely to occur.

For the lower frequency mode, the oscillatory pressure amplitude tends to increase with distance from the cavity. For the high frequency mode, the oscillatory pressure amplitude tends to decrease with distance from the cavity. It is of interest to note these pressure distributions could be approximated by only the first two terms in the series expansion, i.e.:

$$\tilde{p} \simeq J_1 \left(\alpha_{10}\, r/r_w\right) \cos m\theta \left(a_{00}^{(2)} + a_{01}^{(2)} \cos \frac{\pi z}{L}\right) \tag{86}$$

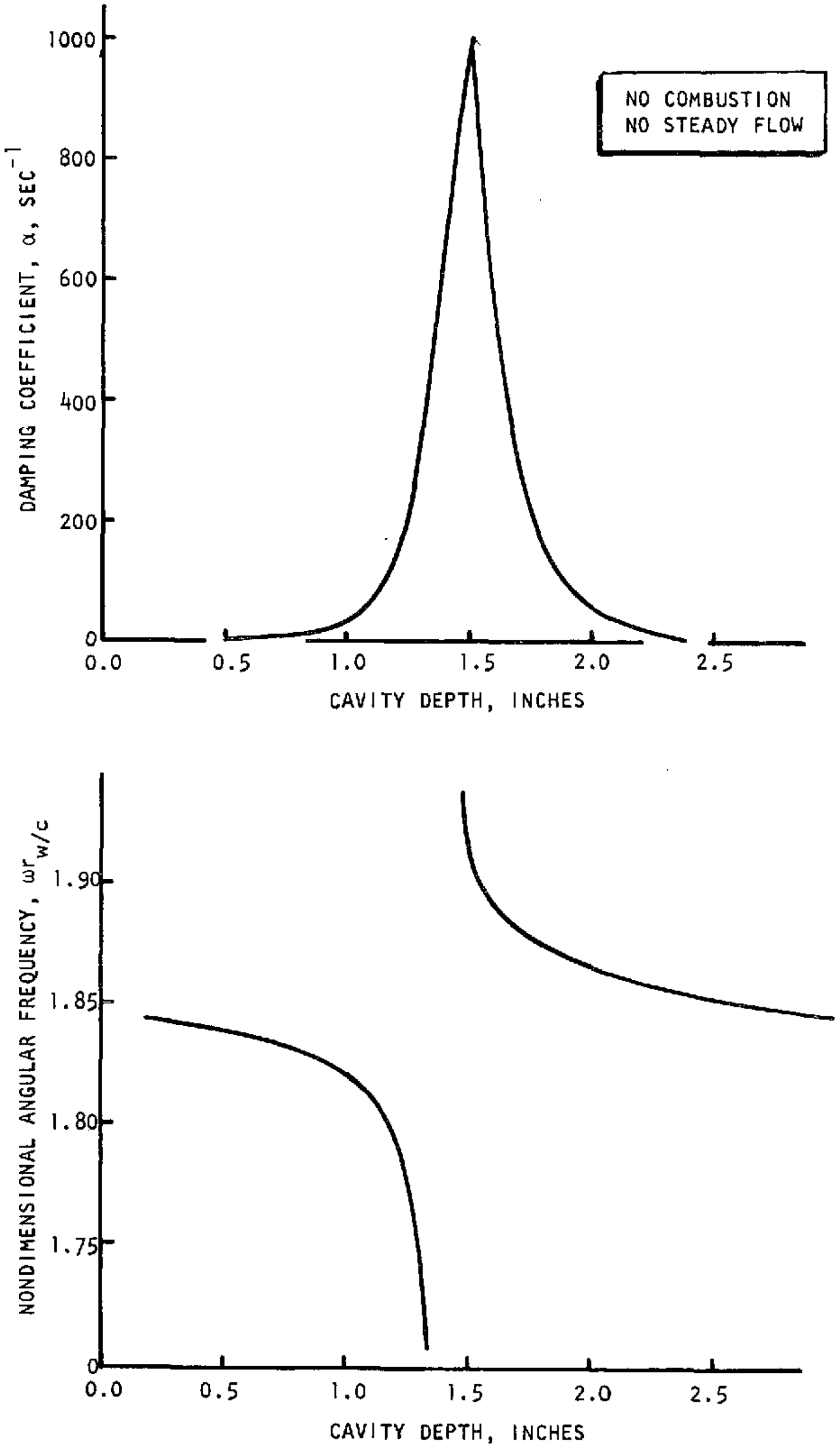

Figure 14. Predicted Cavity Damping Without Combustion or Steady Flow

It is also of interest that the flow of energy can be related to phase of the pressure:

$$\tilde{p} = \hat{p}\ e^{j\psi} \tag{87}$$

The energy flux is (for no steady flow)

$$\vec{I} = \tilde{p}\ \mathrm{Re}\ (\vec{\tilde{u}}) \tag{88}$$

so that the time averaged energy flux is:

$$\langle \vec{I} \rangle = \langle \tilde{p}\ \mathrm{Re}\{\tilde{u}\} \rangle = -\ \frac{\hat{p}^2}{\bar{\rho}\omega}\ \nabla\psi \tag{89}$$

The lines of constant phase are expected to have the qualitative features sketched below:

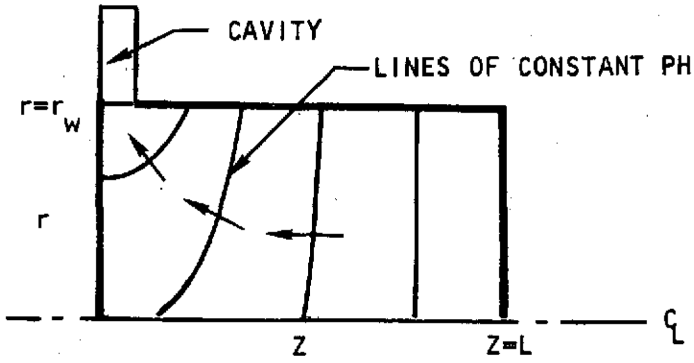

An examination of the computer results shows that this is the case if spatial oscillations in ψ are averaged out, since spatial oscillations are probably due to the finite nature of the expansion series. Physically, acoustical energy flows out of the chamber at the acoustic cavity. This energy flows from all parts of the chamber.

Uniform Combustion

The simplest source term is a spatially uniform combustion. For this case the wave equation becomes:

$$(\bar{\nabla}^2 + k^2)\ \tilde{p} = -h\tilde{p} \tag{90}$$

For the rigid wall (no cavity case), the solution to this equation is:

$$\tilde{p} = \phi_{100}\ e^{jkct} \tag{91}$$

$$k = \sqrt{\eta_{100}^2 - h} \simeq \eta_{100} - \frac{h}{2\eta_{100}}$$

For a purely imaginary combustion coefficient, a growing wave results; the computer program was checked for this simple case.

Spatially Uniform Combustion With Acoustic Cavity

A set of calculations was made for a uniform combustion source term. Results from these calculations are shown in Fig. 15. The primary effect is to shift the damping coefficient curve downward from the no-source case, as expected. Also, the net damping coefficient approximately equals the sum of the cavity and source contributions (calculated individually), i.e.:

$$\alpha_{comb} + \alpha_{cav} \simeq \alpha_{both} \tag{92}$$

An examination of the calculated pressure distributions shows little change due to the addition of the uniform combustion.

Nonuniform Combustion With Acoustic Cavity

Calculations were made with an exponentially varying combustion distribution, i.e.:

$$h(z) = \bar{h}\ e^{-z/\lambda} \tag{93}$$

From Eq. 70 it is evident that the contribution to the overall damping coefficient should be approximately proportional to:

$$\alpha \sim -\int |\tilde{p}|^2\ \mathrm{Im}\ \left\{h(z)\right\}\ dV \tag{94}$$

This expression suggests that this contribution will be nearly constant as λ is varied if $\tilde{p}$ is approximately independent of axial position and:

$$\int \mathrm{Im}\ \left\{h(z)\right\}\ dz = \text{constant} \tag{95}$$

or

$$\bar{h}(\lambda) = \bar{h}(\lambda \to \infty)\ \frac{L}{\lambda}\ \frac{1}{1 - e^{-L/\lambda}} \tag{96}$$

The effectiveness of this approach is demonstrated by the following results (no acoustic cavity):

ℓ_s, inches	h_o	λ, inches	$\frac{\omega r_w}{c}$	$\frac{\alpha r_w}{c}$
1.45	0.0 + 0.006j	1000	1.8413	-0.02453
↓	0.0 + 0.013878j	5	1.8414	-0.02466
	0.0 + 0.0018783j	-5	1.8414	-0.02466

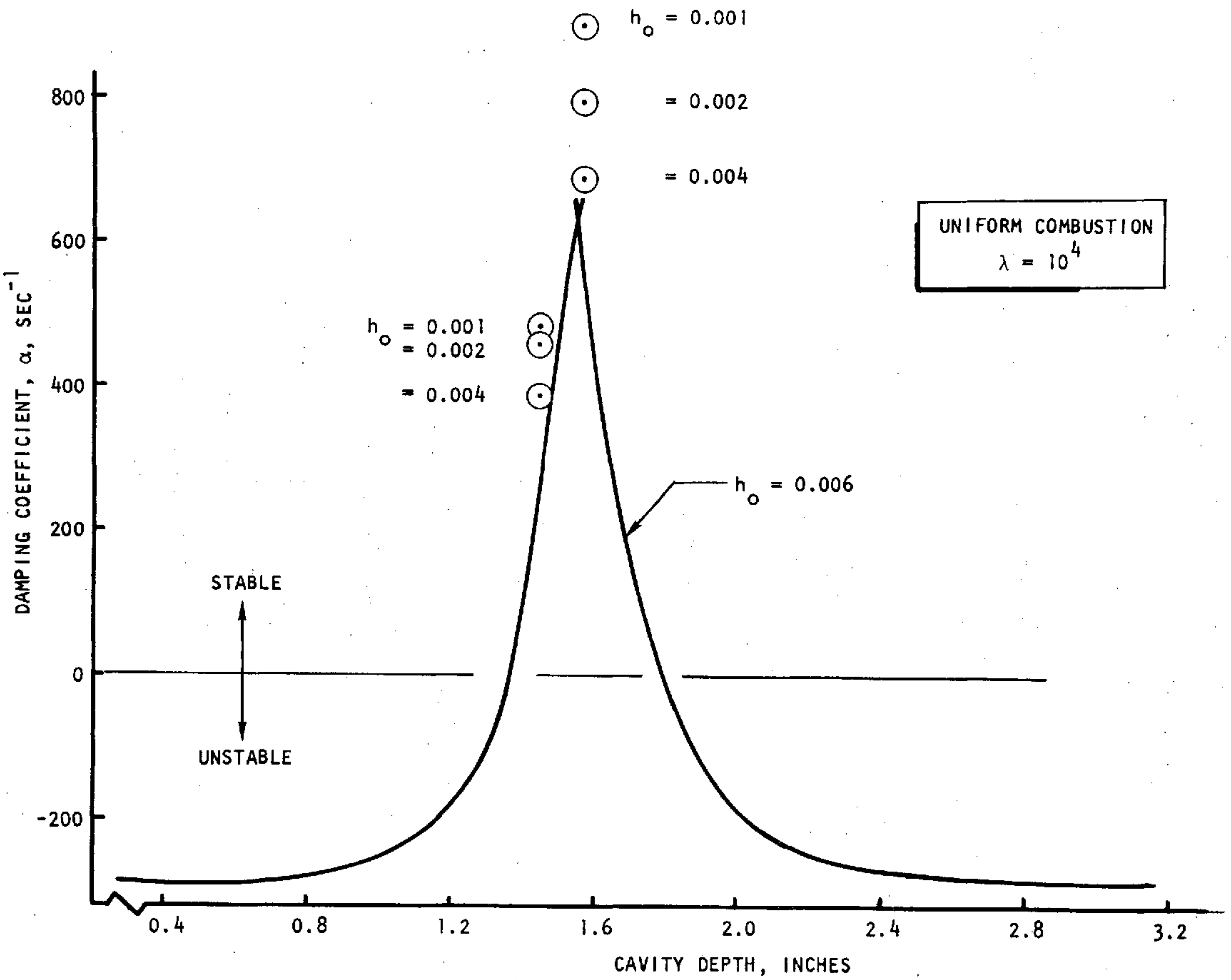

Figure 15. Predicted Effects of Uniform Combustion Source on Cavity Damping

The change in damping (or driving) is indicated by the change in the $\alpha r_w/c$. The negative value for λ corresponds to shifting the cavity to the opposite end of the chamber. In this mode, there is a small average flow of acoustic energy in the z-direction from the region of greater combustion to that of less combustion. When an acoustic cavity was introduced, the following results were obtained:

ℓ_s	$\mathrm{Re}\{h_o\}$	$\mathrm{Im}\{h_o\}$	λ, inches	$\frac{\omega r_w}{c}$	$\frac{\alpha r_w}{c}$
1.45	0.0	0.013878	5.0	1.7756	0.02116
↓	↓	0.006000	1000.0	1.7764	0.02331
		0.001878	-5.0	1.7767	0.02488
1.65		0.013878	5.0	1.8819	0.02066
↓		0.006000	1000.0	1.8832	0.01901
		0.001878	-5.0	1.8845	0.01732

Thus, the effect of changing λ has an opposite effect for the lower and upper (ℓ_s = 1.45, 1.65 correspond to the lower and upper modes, respectively). This result implies that the effects are not additive, i.e.:

$$\alpha\ (h,\ y_{cav}) \neq \alpha\ (h = 0,\ y_{cav}) + \alpha\ (h,\ y_{cav} = 0)$$

The trends of these results can be explained in terms of the following equation:

$$\alpha \sim - \int \mathrm{Im}\{h(z)\}\ |\tilde{p}|^2\ dV \tag{97}$$

The damping due to the cavity is greatest when the trends in pressure amplitude and combustion source, h(z), are the same, i.e., both increasing or both decreasing with axial position.

Effects of Steady Flow

At present the model only includes a uniform steady flow, $\overline{M} = \overline{u}/\overline{c}$, independent of position. Steady flow affects stability through its convective effect in the wave equation (Eq. 57) and also through the nozzle boundary condition (Eq. 60). Also, the injector boundary condition has been maintained as $\partial\tilde{p}/\partial z = 0$.

Without combustion or acoustic cavities, the inhomogeneous wave equation can be solved analytically. However, the first-tangential mode is independent of z and thus the addition of steady flow has no effect, since the relevant terms involve z-derivatives of pressure. Therefore, the program was checked out by comparison with analytical results for the first-tangential/first-longitudinal mode $\phi_{101} = J_1(1.841\ r/R)\ \cos \pi z/L\ \cos\theta$, with injector and nozzle boundary conditions of $\partial\tilde{p}/\partial n = 0$. The results were in agreement.

Calculations to investigate the effects of steady flow with distributed combustion but no cavity, with

h_o = 0.0 +0.013878j

λ = 5.0 inches

$\overline{M}$ = 0.1

led to the conclusion that there was no significant difference between the flow and no-flow cases. However, when an acoustic cavity was also included, the effects were significant, as shown below:

ℓ_s, inches	h_o	λ, inches	$\frac{\omega r_w}{c}$	$\frac{\alpha r_w}{c}$	$\bar{M}$
1.45	0.0 + 0.01387824j	5.0	1.7751	0.01729	0.0
	0.0 + 0.01387824j		1.7798	0.04511	0.1
	0.0 + 0.0j		1.7707	0.04280	0.0
	0.0 + 0.0j		1.7753	0.07190	0.1

The change in the damping coefficient, α, due to a steady-state flow M = 0.1 is approximately independent of the presence of combustion (i.e., $\Delta\alpha\ r_w/c$ = 0.045 - 0.017 = 0.028 and 0.072 - 0.043 = 0.029). The presence of steady flow increased the damping rate α for the cases considered, but for these cases, the amplitude of the oscillatory pressure $|\tilde{p}|$ decreases with increasing axial position.

Effects of Nozzle Admittance

For these calculations, the nozzle admittance has been taken to be a purely real positive number in Eq. 82 and, thus, has a damping effect. The major effect of nozzle admittance is to change the phase ψ of the pressure distribution so as to imply flow of acoustic energy into the nozzle according to Eq. 97. This can be seen in the following case (no acoustic cavity, λ = 1000 inches):

λ, inches	h_o	$\frac{\omega r_w}{c}$	$\frac{\alpha r_w}{c}$	A
1000	0.0 + 0.006j	1.8413	-0.02453	0
1000	0.0 + 0.006j	1.8432	-0.00849	1.0

The phase angle can be shown to be a function only of z in the absence of the acoustic cavity and is shown in Fig. 16. These results agreed with analytical results for the same case. With an acoustic cavity, the steady-flow effect was changed:

λ, inches	h_o	ℓ_s, inches	$\frac{\omega r_w}{c}$	$\frac{\alpha r_w}{c}$	A
5	0.0 + 0.01387824j	1.45	1.7798	0.04511	0
5	0.0 + 0.01387824j	1.45	1.7735	0.04922	1.0

The nozzle has the expected damping effect but, although the admittance is the same as in the preceding case, the incremental change in damping ($\Delta\alpha r_w/c$ = 0.04922 to 0.04511 = 0.00411) is down by a factor of four from the preceding case ($\Delta\alpha r_w/c$ = -0.00849 + 0.02453 = 0.01604). It is noted that the pressure amplitude $|\tilde{p}|$ at the

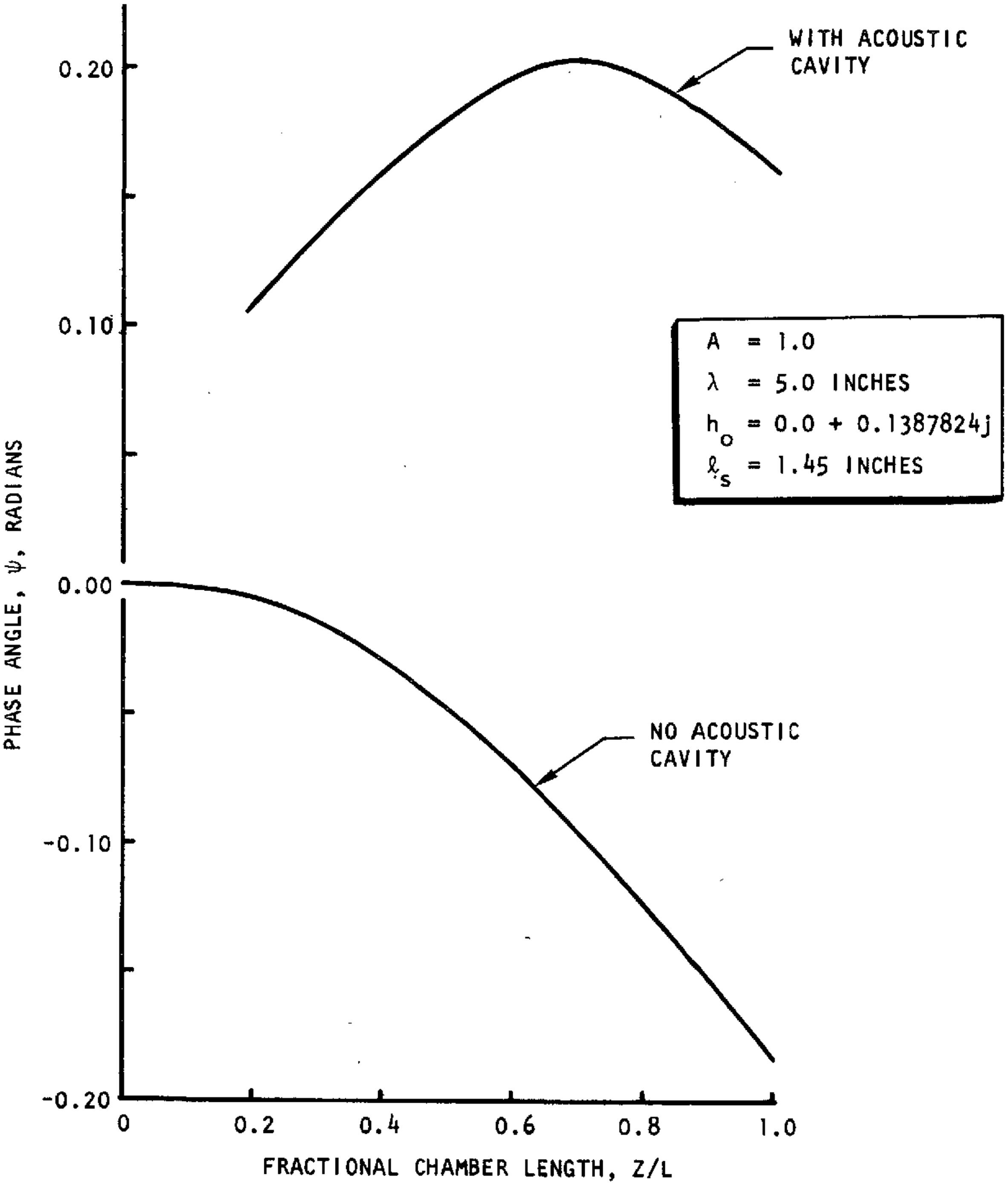

Figure 16. Predicted Effect of Nozzle on Phase Angle of Oscillating Pressure

nozzle has the same radial distribution in both cases, but the pressure $|\tilde{p}|$ decreases by approximately 50 percent in going from the injector to the nozzle in the latter case. The factor of four is most likely determined by the square pressure of the pressure at the nozzle in these cases.

It is expected that nozzle admittance will more strongly damp the lower mode because the pressure at the nozzle is relatively higher. The plot of phase angle in Fig. 16 shows that the flow of energy to the nozzle in accord with Eq. 97. The phase depends strongly on r for $0 < z/L < 0.2$ because of the acoustic cavity and, therefore, is not shown.

Effect of Cumulative Combustion-Convection Term

The last source term in Eq. 57 may be described as the cumulative combustion-convection term. The inclusion of this term in the program was found to have negligible effect on the results for $\bar{M} = 0.1$ for the few cases studied. The reason is probably associated with the rapid oscillations corresponding to the exponential term in the integral.

CONCLUDING REMARKS

The principal objective of the program described herein was to analytically predict the relative combustion stability of various propellant combinations of interest to NASA-JSC when used with hardware configurations representative of current design and properties with or without acoustic cavities. As noted earlier, consideration was originally given to propellant combinations of the LOX/hydrocarbon, LOX/amine, and NTO/amine families, but was later concentrated on the NTO/amine family because of diminished interest in the other families.

To meet the objective of the program, several kinds of analysis were performed. Although this objective was achieved within the context of the contracted program and considerable progress has been made, the results show the need for further analysis.

Considerable information was generated as a result of the literature review. However, the information shows considerable diversity, which probably reflects the general complexity of the instability problem. The results are probably best utilized in conjunction with an analytical model to relate the conditions at a point of interest to those that previously evaluated experimentally.

A Priem-type stability analysis was done for a relatively broad range of conditions. Extensive plots of the variation of the stability index, A_n, with important physical parameters have been developed. Because these plots were developed in terms of physical parameters, which minimized the total number of parameters, they do not show all effects of interest. However, the plots may be used by interpolation to assess the effect of varying other parameters and, similarly, they may be used to assess the stability of new hardware configurations with minor additional calculations. The manner in which this may be done has been illustrated by the additional calculations. The results from this analysis show the importance, when performing stability analyses, of the choice of parameters to be held constant. Opposite effects can be predicted by changing the parameters held constant. In addition, the results suggest that the propellant mass flux within an engine has a very strong influence on stability. The greatest stability changes were predicted when (1) chamber pressure was increased by increasing the propellant flow through a fixed set of hardware (worsened stability) or (2) contraction ratio was increased with a fixed thrust (improved stability).

The analysis done with the NREC stability model was less extensive than that done with the Priem-type model. The Priem-type analysis was done with generalized parametric curves that were available; but similar curves are not available for the NREC analysis and greater effort was required for each of these cases. The results from the NREC analysis appear to be roughly compatible with those from the Priem-type analysis. The degree of agreement appears consistent with the major differences in approach that have been used in development of the two models. The NREC model, or similar approaches, appears to be a valuable method of analysis for liquid-propellant engines. The Priem and NREC models complement each other because each includes important factors not included in the other. Further work with the NREC model is recommended.

Because of the need for a model to aid in the design of acoustic cavities that specifically included the effects of combustion and steady flow, development of a generalized acoustic cavity model was also undertaken. This model was based on a combination of the concepts used in the existing cavity damping model (which does not specifically allow for combustion and steady flow) and those used in the NREC model. Preliminary development of this model was completed, with an iterative variational solution method being used. At present the model includes effects due to pressure-coupled combustion response (velocity coupling effects remain to be added), nozzle effects, and steady flow (as a uniform approximattion), as well as the acoustic cavity. Each of these contributions has been added incrementally and checked by comparison with analytical results for limiting cases. The limited results obtained thus far show the importance of interactions between the effects of the cavities and those due to the nozzle, combustion and steady flow, under some circumstances. Because of these interactions, the need to adequately allow for them in cavity design is evident and additional work is recommended.

REFERENCES

1. Dix, M. D. and G. E. Smith, "Analysis of Combustion Instability in Aircraft Engine Augmentors," AIAA Paper No. 71-700, presented at the AIAA/SAE 7th Propulsion Joint Specialist Conference, Salt Lake City, Utah, June 1971.

2. Culick, F. E. C., "Stability of High-Frequency Pressure Oscillations in Rocket Combustion Chambers," AIAA J., Vol. 1, No. 5, May 1963.

3. Bates, J. O., Experimental Evaluation of Storable Liquid Propellants in Large Rocket Engines, R-1955, Rocketdyne Division, Rockwell International, Canoga Park, California, December 1959.

4. Levine, R. S., Rocketdyne Experience Regarding the Combustion Chamber Tractability of Various Propellant Combinations, RR-58-45, Rocketdyne, November 1958.

5. Nestlerode, J., Rocketdyne, Private Communication.

6. Mikuni, D., Rocketdyne, Private Communication.

7. Stassinos, J., Rocketdyne, Private Communication.

8. Rocketdyne Research Memorandum, RM 848/352, 1 February 1962.

9. Coultas, T. A. and R. S. Levine, "Baffles and Chemical Additives as Acoustic Combustion Stability Suppressors in a Two-Dimensional Thrust Chamber," Second ICRPG Combustion Conference, CPIA Publication No. 105, Vol. 2, May 1966, p. 61.

10. Rocketdyne Research Memorandum, RM 413/91, 18 June 1959.

11. Fourteenth NASA F-1 Program Review, Rocketdyne, May 1964.

12. Rocketdyne Research Memorandum, CHTUM 58-31, 25 August 1958.

13. Richtenburg, W., Rocketdyne, Private Communication.

14. Shuster, E., Rocketdyne, Private Communication.

15. Oberg, C. L., "LM Ascent Engine Acoustic Cavity Study," Sixth ICRPG Combustion Conference, CPIA Publ. No. 192, Vol. 1, December 1969, p. 303.

16. Oberg, C. L. et al., "Evaluation of Acoustic Cavities for Combustion Stabilization," Seventh JANNAF Combustion Meeting, CPIA Publ. No. 204, Vol. 1, February 1971, p. 743.

17. Oberg, C. L. et al., "Combustion Stabilization with Acoustic Absorbers," Fifth ICRPG Combustion Conference, CPIA Publ. No. 183, December 1968, p. 359.

18. Bell Aerosystems Report No. D8539-953001.

19. Senneff, J. M. and P. J. Morgante, "Combustion Stability Investigation of the LM Ascent Engine," Second ICRPG Combustion Conference, CPIA Publ. No. 105, Vol. 1, May 1966, p. 23.

20. Senneff, J. and K. Berman, "Stability Investigation Relating to Bell/LM Ascent Engine," Sixth ICRPG Combustion Conference, CPIA Publ. No. 192, Vol. 1, December 1969, p. 317.

21. Sherman, E. W., Jr. and D. T. Harrje, "History of Model 8533 Evolution with Particular Emphasis on Stability Aspects,: Sixth ICRPG Combustion Conference, CPIA Publ. No. 192, Vol. 1, December 1969, p. 351.

22. Reardon, F. H., "Advanced Agena Engine Combustion Stability Program,: Sixth ICRPG Combustion Conference, CPIA Publ. No. 192, Vol. 1, December 1969, p. 357.

23. Mehegan, P., Rocketdyne, Private Communication.

24. Dykema Owen, Aerospace, Private Communication.

25. Hefner, R. J., "Combustion Stability Development at Aerojet-General, First ICRPG Combustion Instability Conference, CPIA Publ. No. 68, Vol. 1, January 1965, p. 9.

26. Aerojet-General Corporation Report GEMSIP FR-1, SSD-TR-66-2, 31 August 1965.

27. McBride, J. M. and R. J. Hefner, "Combustion Stability Characteristics of the Apollo SPS and Transtage Liquid Rocket Engines," Fourth ICRPG Combustion Conference, CPIA Publ. No. 162, Vol. 1, December 1967, p. 29.

28. Abbe, C. J. and W. L. Putz, "The Bipropellant Combustion Stability Characteristics of Hydrazine and MMH Fuels with Nitrogen Tetroxide for Post-Boost Propulsion Application," Sixth ICRPG Combustion Conference, CPIA Publ. No. 192, Vol. 1, December 1969, p. 93.

29. Abbe, C. J. et al., "Influence of Storable Propellant Liquid Rocket Design Parameters on Combustion Instability," Fourth ICRPG Combustion Conference, CPIA Publ. No. 162, Vol. 1, December 1967, p. 73. Also see J. Spacecraft and Rockets, Vol. 5, No. 5, May 1968, pp. 584-90.

30. Weiss, R. and R. Klopotek, Experimental Evaluation of the Titan III Transtage Engine Combustion Stability Characteristics, AFRPL Report No. TR-66-51, March 1966.

31. Houseman, J., "Jet Separation and Popping with Hypergolic Propellants," Seventh JANNAF Combustion Meeting, CPIA Publ. No. 204, Vol. 1, February 1971, p. 445.

32. Clayton, R. M., "Baffle Performance with High-Impedance Injectors," Seventh JANNAF Combustion Meeting, CPIA Publ. No. 204, Vol. 1, February 1971, p. 797.

33. Bailey, C. R., "Acoustic Liner for the C-1 Engine," Fifth ICRPG Combustion Conference, CPIA Publ. No. 183, December 1968, p. 335.

34. Hoeptner, H. W., "Test Results and Analysis of Pulse Initiated Oscillations in the UTC 8K Engine," Second ICRPG Combustion Conference, CPIA Publ. No. 105, Vol. 1, May 1966, p. 47.

35. Moberg, D. A., "Attentuation of Tangential Combustion Instability in an Ablative, Hypergolic Bipropellant 1750-Pounds-Thrust Rocket Engine," Fourth ICRPG Combustion Conference, CPIA Publ. No. 162, Vol. 1, December 1967, p. 15.

36. Minton, S. J. and E. Z. Zwick, "An Investigation of Manifold Explosions in Rocket Engines," Third ICRPG Combustion Conference, CPIA Publ. No. 138, Vol. 1, February 1967, p. 497.

37. Marquardt Report S-483, *An Investigation of Oxidizer Manifold Explosions in the Apollo SM/RCS Engine*, 1 February 1966.

38. Coultas, T. A. and R. C. Kesselring, "Extension of the Priem Theory and Its Use in Simulation of Instability on the Computer," Proceedings of the Second ICRPG Combustion Conference, CPIA Publication No. 105 Chemical Propulsion Information Agency, Silver Spring Maryland, May 1966, page 163-192.

39. Lambiris, S., L. P. Combs, and R. S. Levine, "Stable Combustion Processes in Liquid Propellant Rocket Engines," *Combustion and Propulsion, Fifth AGARD Colloquium* (MacMillan Co., New York, 1963), pages 569-634.

40. Ingebo, R. E., *Dropsize Distributions for Impinging Jet Breakup in Airstreams Simulating the Velocity Conditions in Rocket Combustors*, NASA TN-4222, National Aeronautics and Space Administration, Washington, D.C., 1958.

41. Priem, R. J. and D. C. Guentert, *Combustion Instability Limits Determined by a Non-Linear Theory and a One-Dimensional Model*, NASA TN D-1409, National Aeronautics and Space Administration, Washington, D.C., October 1962.

42. Culick, F. E. C., *Interactions Between the Flow Field, Combustion and Wave Motions in Rocket Motors*, NWC TP-5349, Naval Weapons Center, China Lake, California, June 1972.

43. Heidmann, M.F., *Amplification by Wave Distortion of the Dynamic Response of Vaporization Limited Combustion*, NASA TND-6287, National Aeronautics and Space Administration, Washington, D.C., May 1971.

44. Heidmann, M. F., *Empirical Characterization of Some Pressure Wave Shapes in Strong Travelling Transverse Acoustic Modes*, NASA TMX-1716, National Aeronautics and Space Administration, Washington, D.C., January 1969.

45. Schuman, M. D. and C. L. Oberg, *Rocketdyne contribution to final report Augmentor Combustion Instability Investigation*, General Electric Company, Evandale, Ohio, June 1974.

46. Priem, R. J. and M. F. Heidmann, Propellant Vaporization as a Design Criterion for Rocket Engine Combustion Chambers, NASA Technical Report R-67, National Aeronautics and Space Administration, Washington, D.C. 1960.

47. Heidmann, M. F. and P. R. Wieber, Analysis of Frequency Response Characteristics of Propellant Vaporization, NASA TND-3749, December 1966.

48. Bell, W. A. and B. T. Zinn, The Prediction of Three-Dimensional Liquid-Propellant Rocket Nozzle Admittances, NASA CR-121129, Georgia Institute of Technology, Atlanta, Georgia, February 1973.

49. Morse, P. M. and K. U. Ingard, "Theoretical Acoustics," McGraw-Hill, New York (1968).

50. Oberg, C. L. et al., Final Report, Evaluation of Acoustic Cavities for Combustion Stabilization, NASA CR-115007, R-8757, Rocketdyne, 1971.

51. Morse, P. M. and H. Feshback, Methods of Theoretical Physics, McGraw-Hill, New York (1953), Vol. I, p. 1108.

52. Becker, M., The Principles and Applications of Variational Methods, MIT Press, Cambridge, Massachusetts (1964).

APPENDIX A

DROPSIZE CORRELATIONS

A number of correlations have been developed for predicting propellant dropsize. Some of these are summarized below.

- Ingebo (Ref. A-1) for like doublets:

$$D_{30} = \frac{2.54 \times 10^4}{2.64 \sqrt{\frac{V}{d}} + K\left(\frac{\rho}{\rho_{ref}}\right)^{1/4} |\Delta V|}$$

where

$$K = 0.97 \left[\left(\frac{\mu_2 \sigma_2}{\rho_2}\right)_{n\text{-Heptane}} \Big/ \left(\frac{\mu_2 \sigma_2}{\rho_2}\right)\right]^{1/4}$$

$\rho_{ref} = 10.7 \times 10^{-4}$ g/cc $\quad V \sim$ fps

$\rho = P_c/RT$ $\quad d \sim$ inch

$|\Delta V| \simeq V_{inj}$ $\quad D_{30} \sim$ microns

D_{30} = mass mean drop diameter

The velocity difference $|\Delta V| = |V_g = V_{inj}|$ may be approximated by neglecting V_g or, when used with a steady-state combustion model, it may be adjusted until the predicted performance equal the measured performance

- Dickerson (Ref. A-2) for like doublets:

$$\overline{D} = 5.84 \times 10^4 \, \frac{d^{0.568}}{V^{0.852}} \quad (\text{PCF})$$

where

$D = 2.2\, D_{30} \sim$ microns

$d \sim$ inches

$V \sim$ ft/sec

$\text{PCF} = 1.54\, \mu_L^{1/3} \sigma_L^{1/2} \rho_L$

$\mu_L \sim$ lb/ft sec

$\sigma_L \sim$ dyne/cm

$\rho_L \sim$ g/cc

- Zajac (Ref. A-3) for like doublets (60-degree impingment angle):

$$\text{Laminar Jet } \overline{D}_{wax} = 4.85 \times 10^4 \; V^{-0.75} \; d^{0.57} \left(\frac{Pc}{Pj}\right)^{-0.52}$$

$$\text{Turbulent Jet } \overline{D}_{wax} = 15.9 \times 10^4 \; V^{-1.0} \; d^{0.57} \left(\frac{Pc}{Pj}\right)^{-0.10}$$

where

$\overline{D} \sim$ microns

$V \sim$ ft/sec

$d \sim$ inches

Pc/Pj = Vel. profile parameter ~ 1

and

$$\overline{D}_\gamma = (1.42 - .0073\gamma)\overline{D}_{60}$$

where

D_{60} = dropsize for 60=degree impingement angle

γ = impingement angle

also

$$\overline{D} = \overline{D}_{wax} \; K$$

where

$$K = \left[\left(\frac{\mu\sigma}{\rho}\right)_L / \left(\frac{\mu\sigma}{\quad}\right)_{wax} \right]^{1/4}$$

APPENDIX A REFERENCES

A-1. Ingebo, R. E., Dropsize Distributions for Impinging Jet Breakup in Airstreams Simulating the Velocity Conditions in Rocket Combustors, NASA TN-4222, National Aeronautics and Space Administration, Washington, D.C., 1958.

A-2. Dickerson, R. A. et al., Correlation of Spray Injector Parameters with Rocket Engine Performance, AFRPL-TR-68-147, R-7499, Rocketdyne Division, Rockwell International, Canoga Park, California, June 1968.

A-3. Zajac, L. J., Correlation of Spray Dropsize Distribution and Injector Variables, R-8455, Rocketdyne, September 1969.

APPENDIX B

RESULTS FROM PRIEM-TYPE STABILITY ANALYSIS

This appendix contains a series of plots of the calculated stability index, A_p, for a variety of conditions. These plots summarize the results from the Priem-type stability analysis.

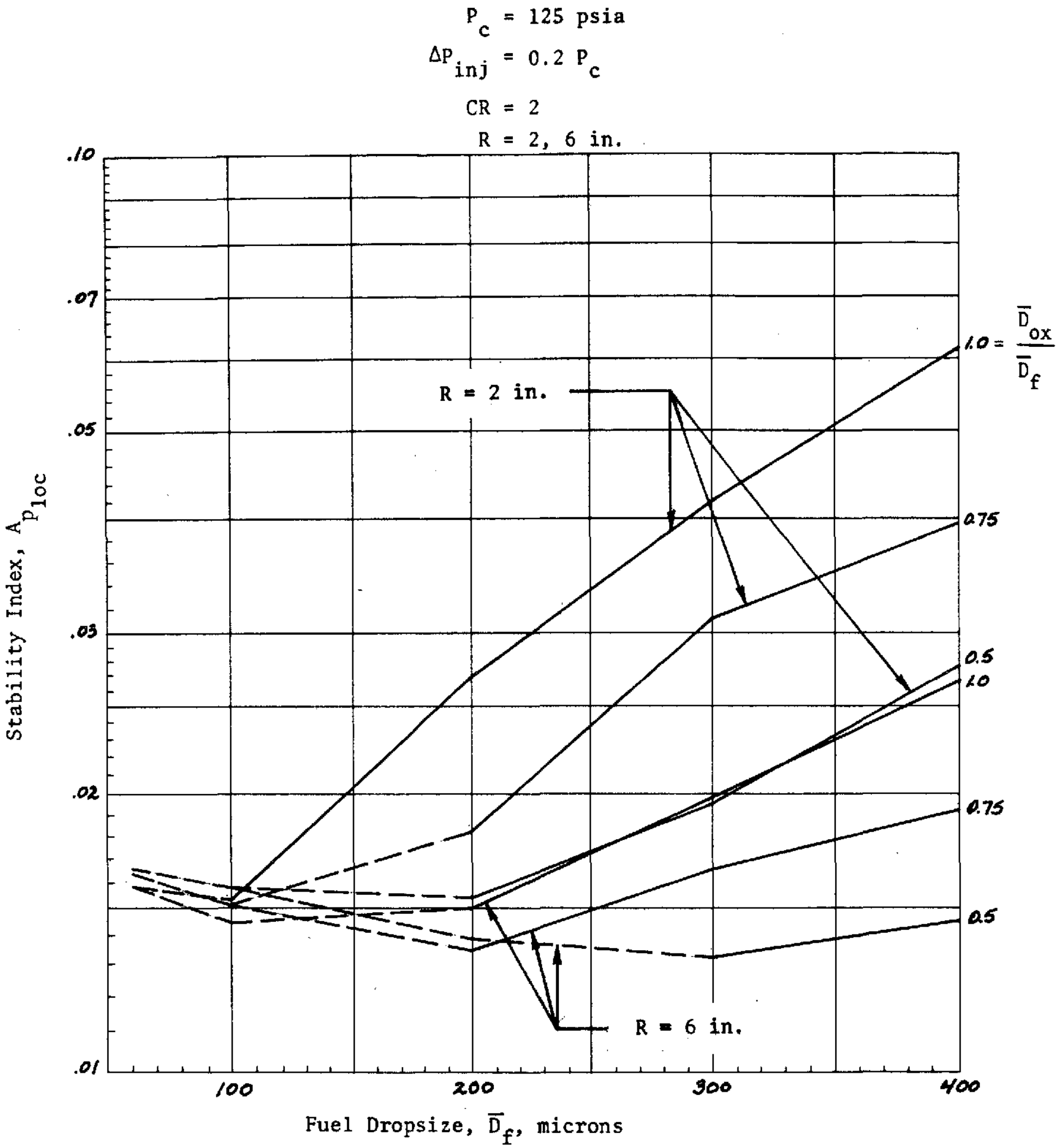

Figure B-1. Local Stability Index as a Function of Dropsize for P_c = 125 psia, $\Delta P_{inj} = 0.2\ P_c$, CR = 2

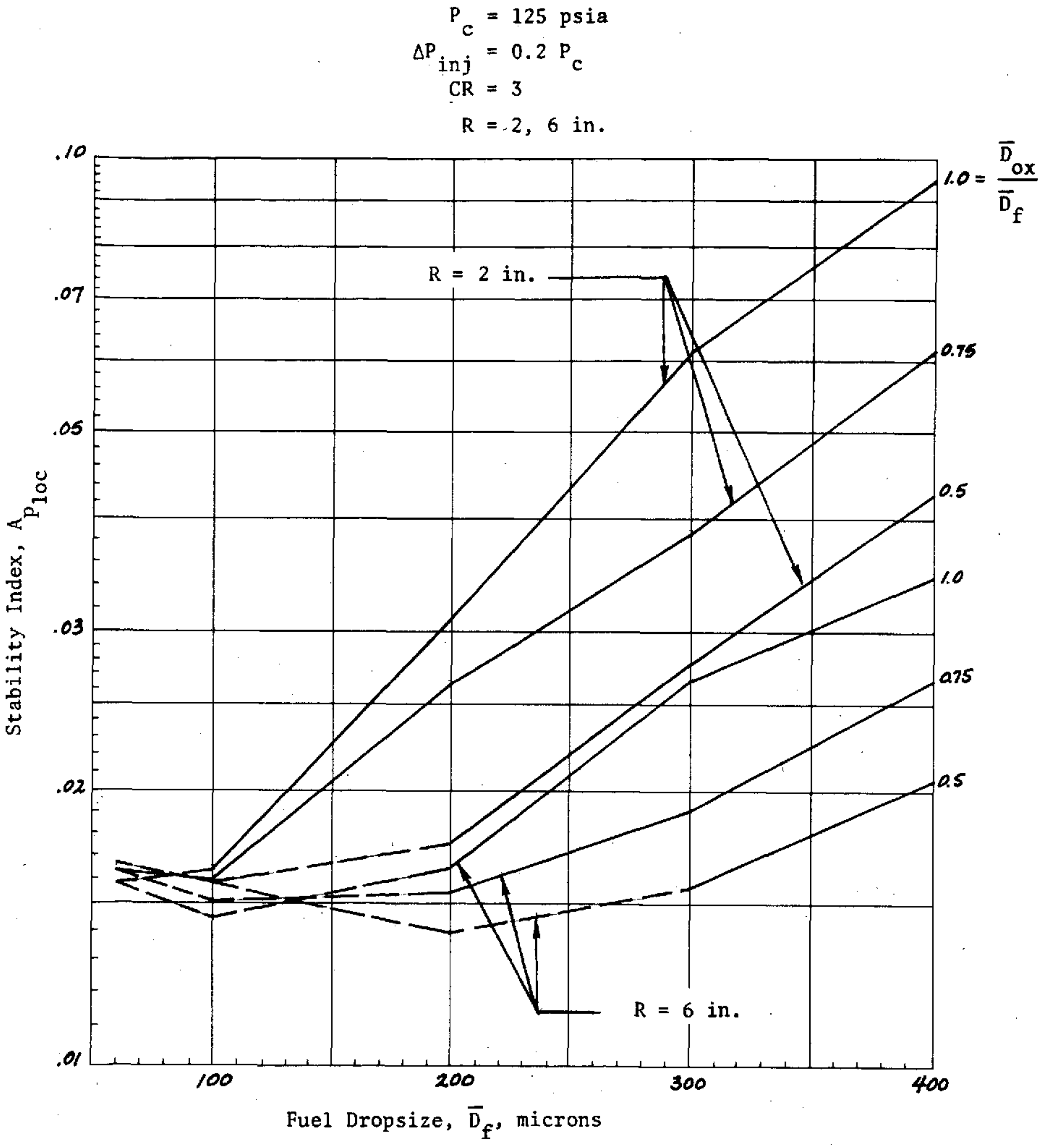

Figure B-2. Local Stability Index as a Function of Dropsize for P_c = 125 psia, ΔP_{inj} = 0.2 P_c, CR = 3

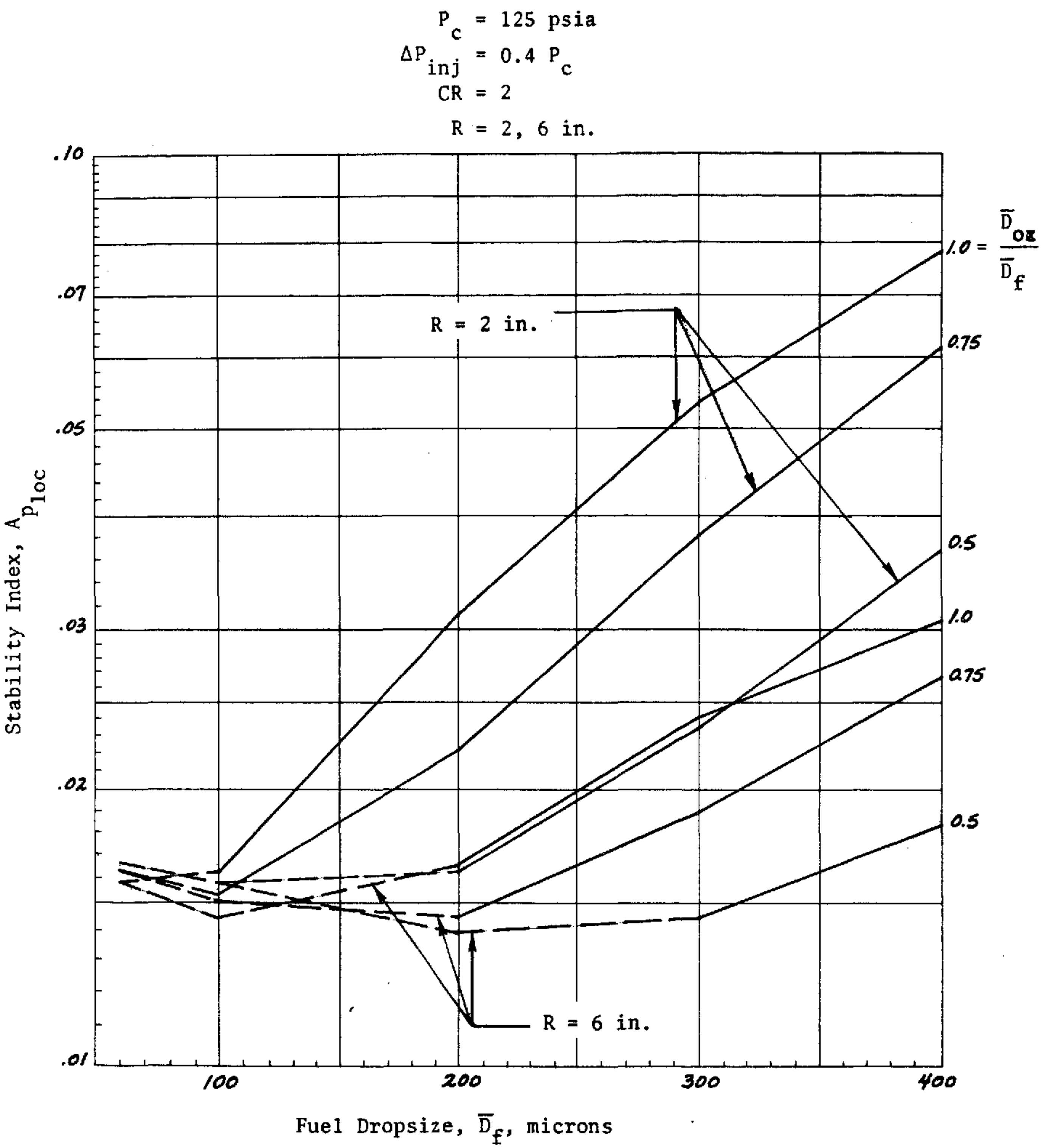

Figure B-3. Local Stability Index as a Function of Dropsize for P_c = 125 psia, ΔP_{inj} = 0.4 P_c, CR = 2

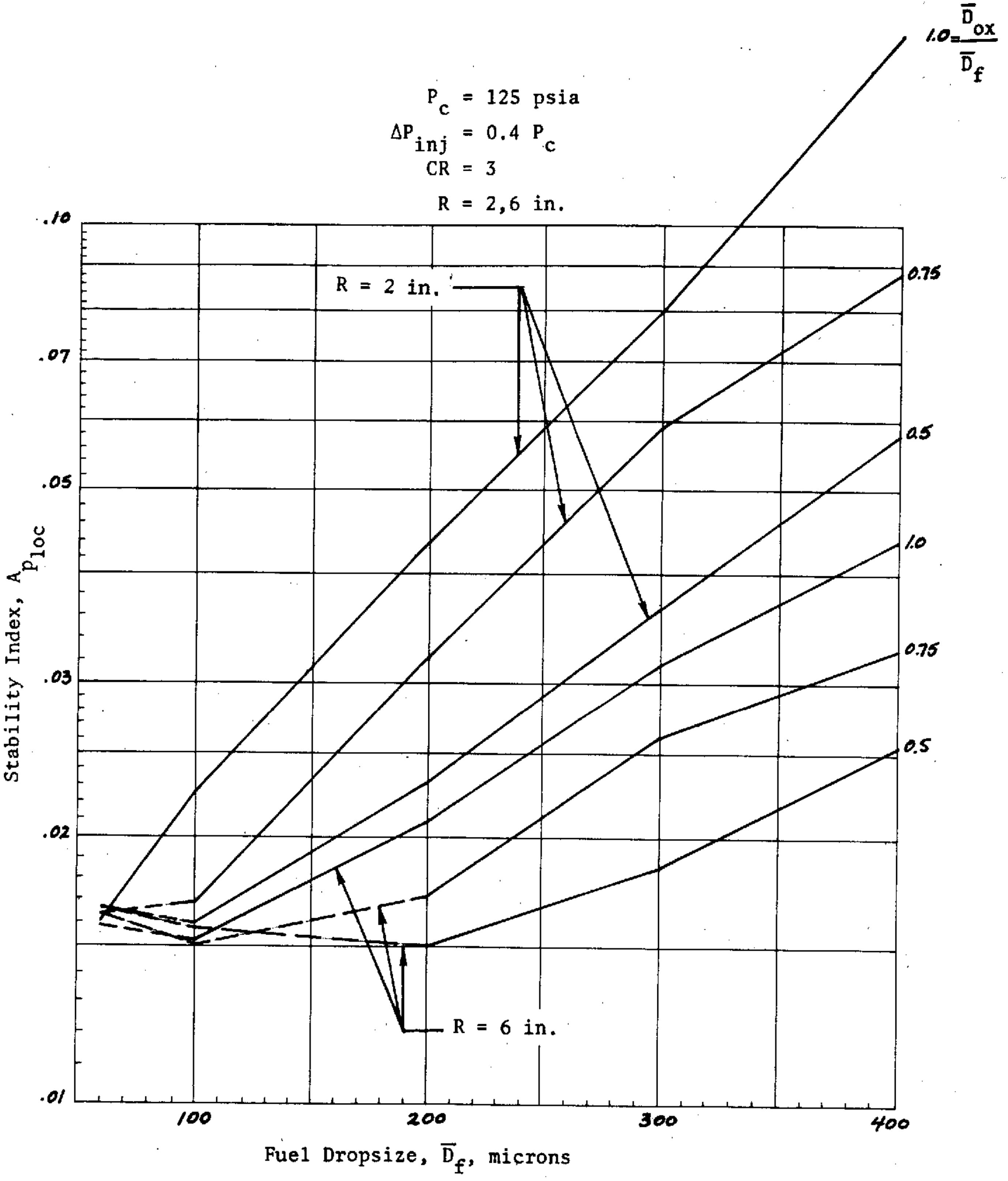

Figure B-4. Local Stability Index as a Function of Dropsize for P_c = 125 psia, ΔP_{inj} = 0.2 P_c, CR = 2

P_c = 200 psia

ΔP_{inj} = 0.2 P_c

CR = 2

R = 2, 6 in.

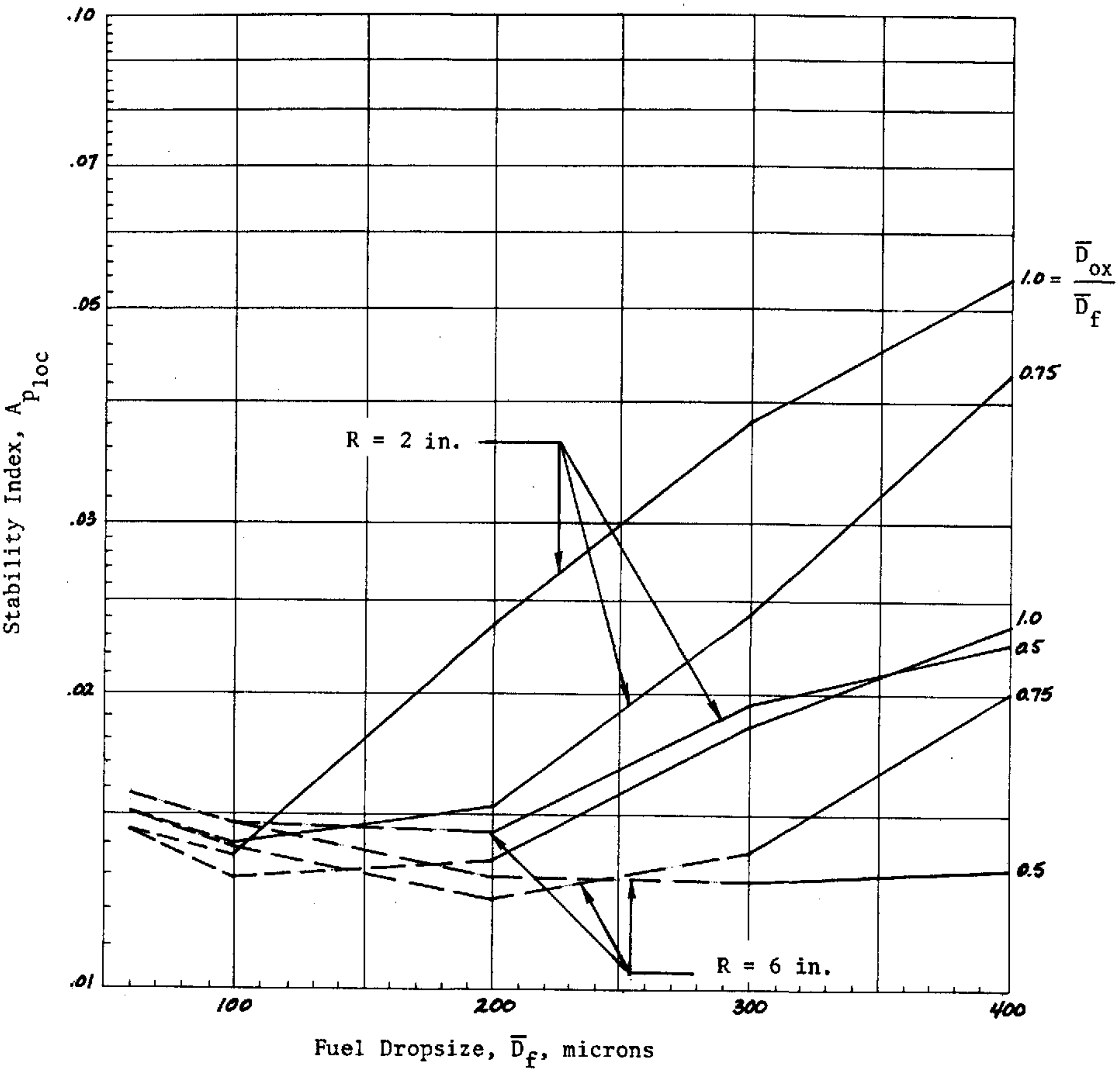

Figure B-5. Local Stability Index as a Function of Dropsize for P_c = 200 psia, ΔP_{inj} = 0.2 P_c, CR = 2

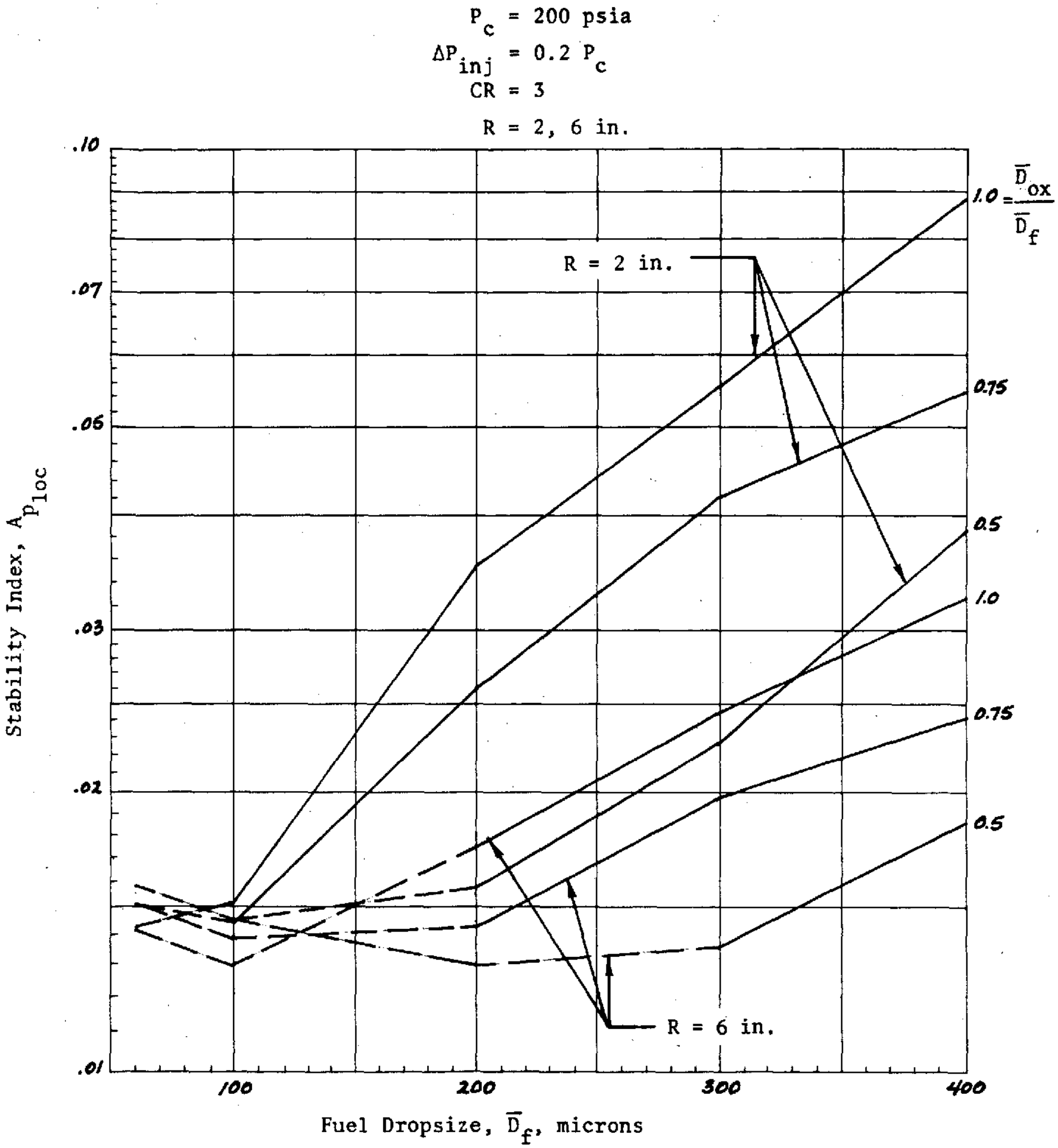

Figure B-6. Local Stability Index as a Function of Dropsize for P_c = 200 psia, ΔP_{inj} = 0.2 P_c, CR = 3

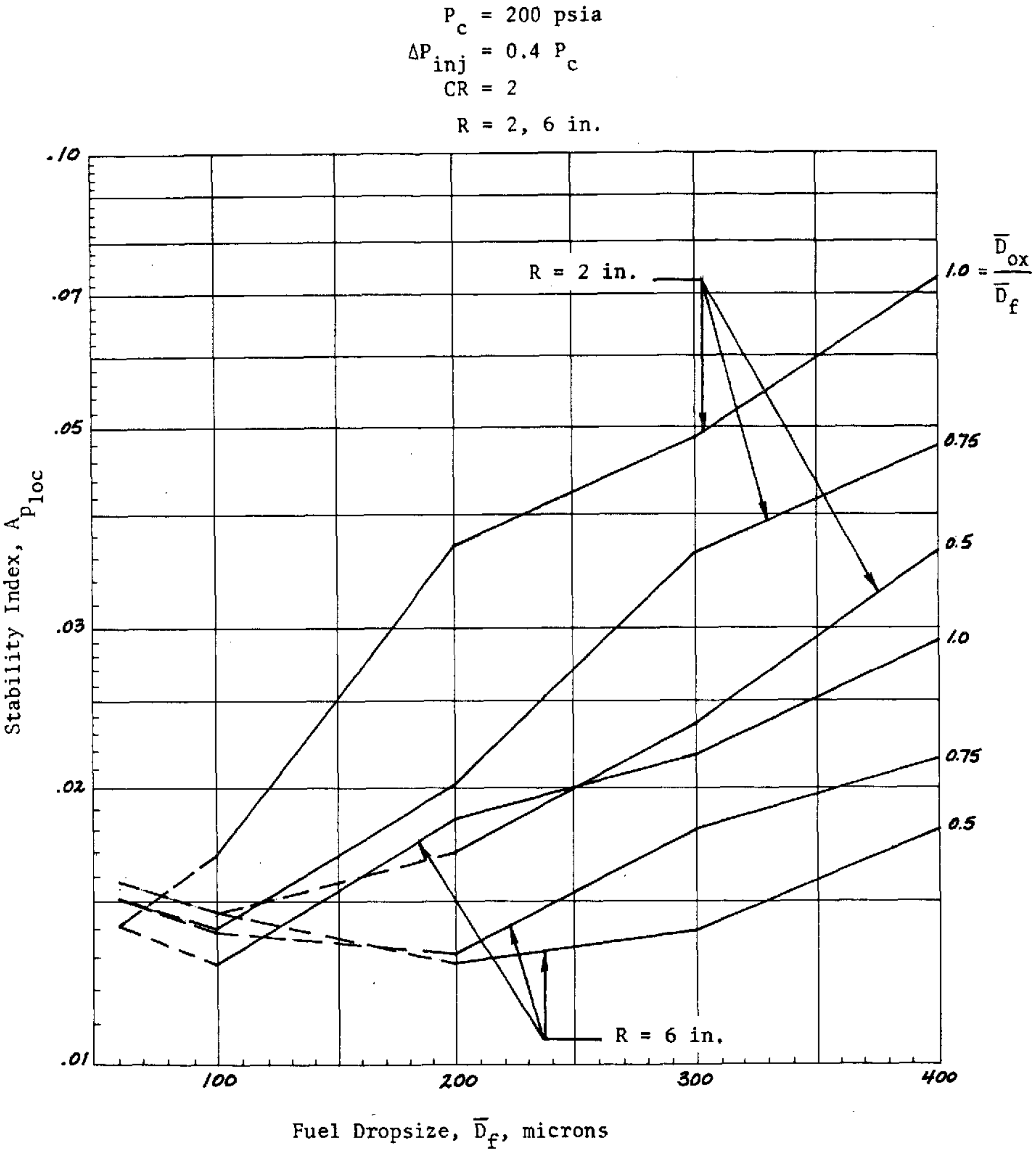

Figure B-7. Local Stability Index as a Function of Dropsize for P_c = 200 psia, ΔP_{inj} = 0.4 P_c, CR = 2

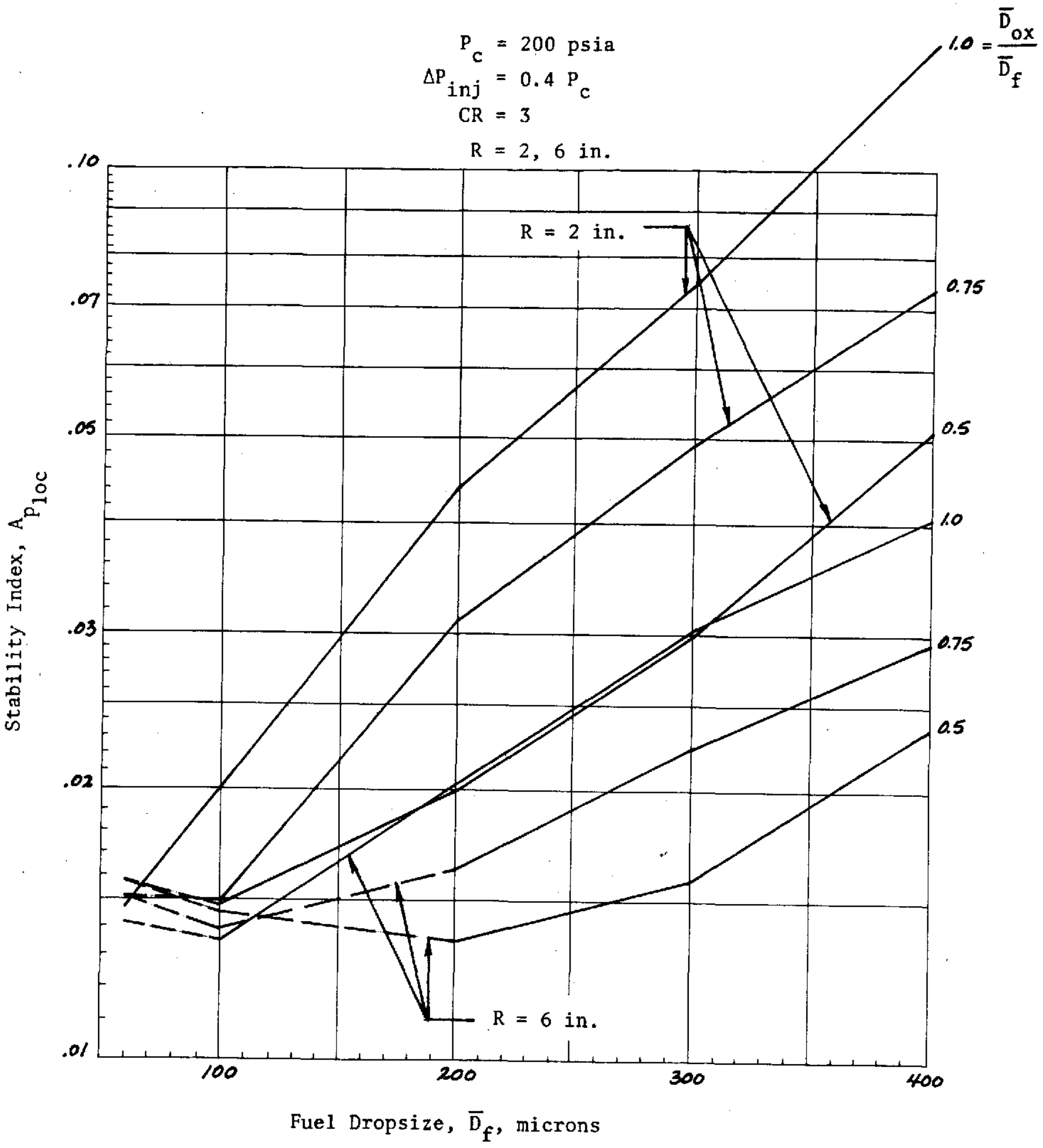

Figure B-8. Local Stability Index as a Function of Dropsize for P_c = 200 psia, ΔP_{inj} = 0.4 P_c, CR = 3

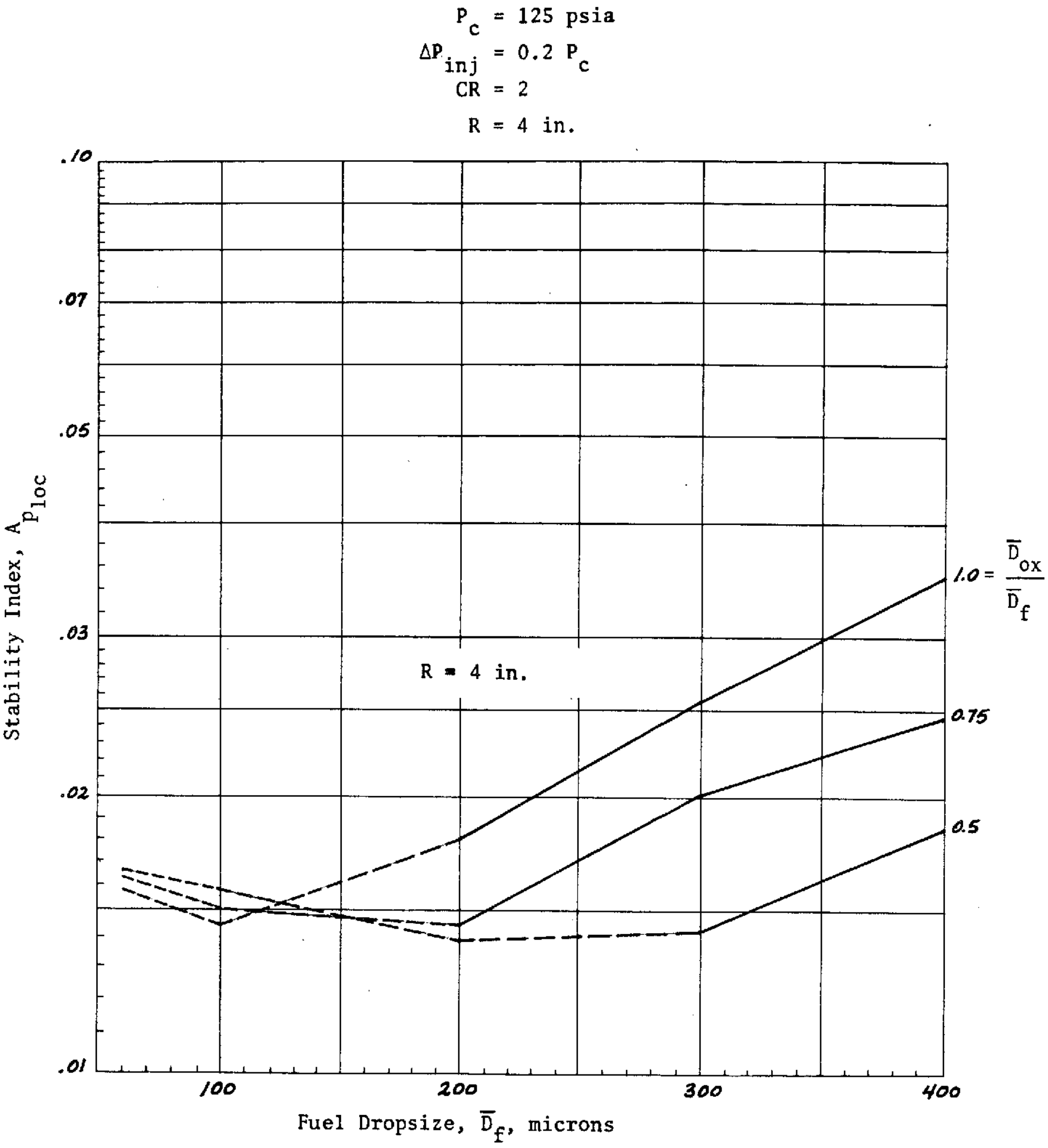

Figure B-9. Local Stability Index as a Function of Dropsize for P_c = 125 psia, ΔP_{inj} = 0.2 P_c, CR = 2

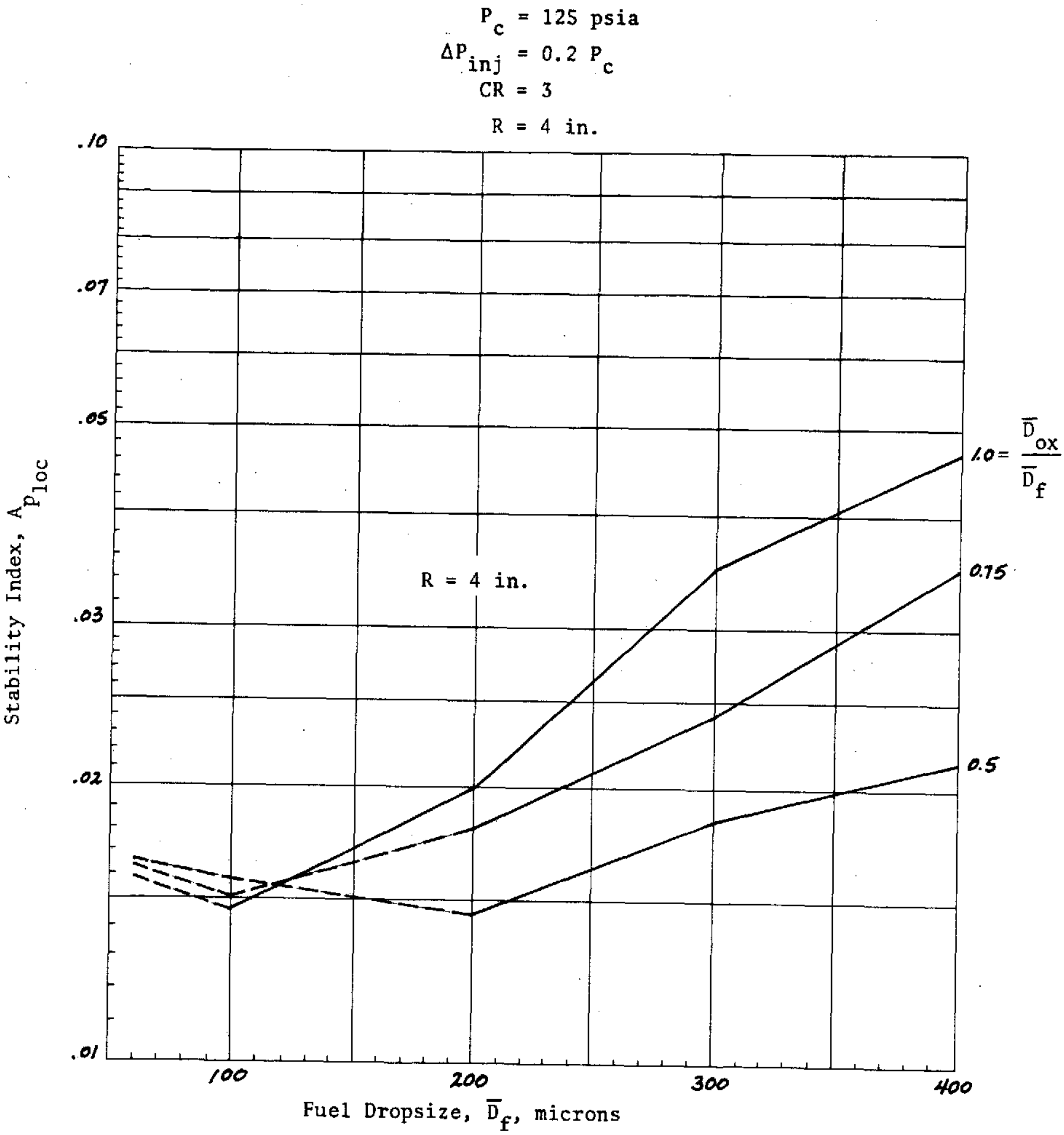

Figure B-10. Local Stability Index as a Function of Dropsize for P_c = 125 psia, ΔP_{inj} = 0.2 P_c, CR = 3

P_c = 125 psia
ΔP_{inj} = 0.4 P_c
CR = 2
R = 4 in.

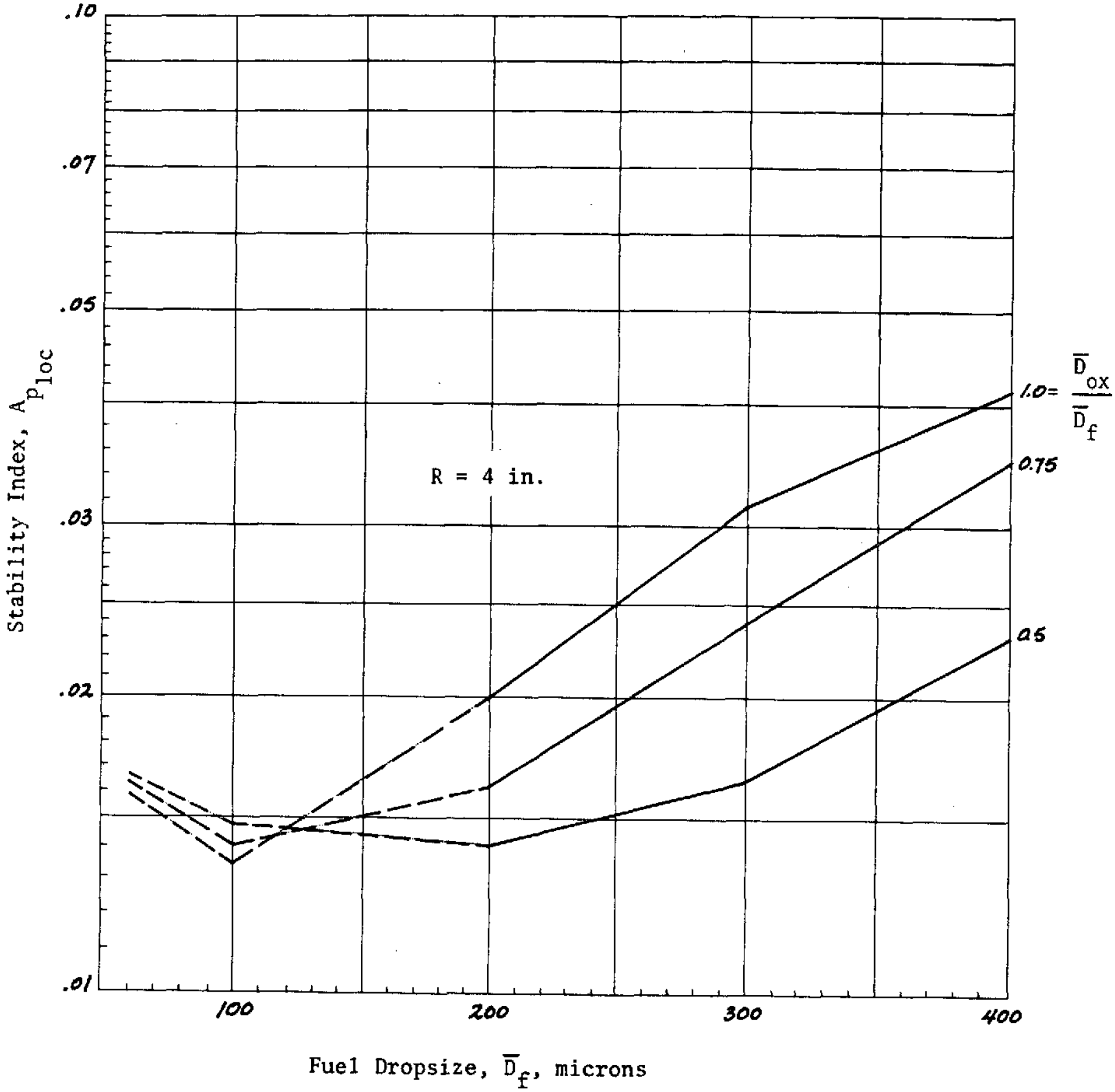

Figure B-11. Local Stability Index as a Function of Dropsize for P_c = 125 psia, ΔP_{inj} = 0.4 P_c, CR = 2

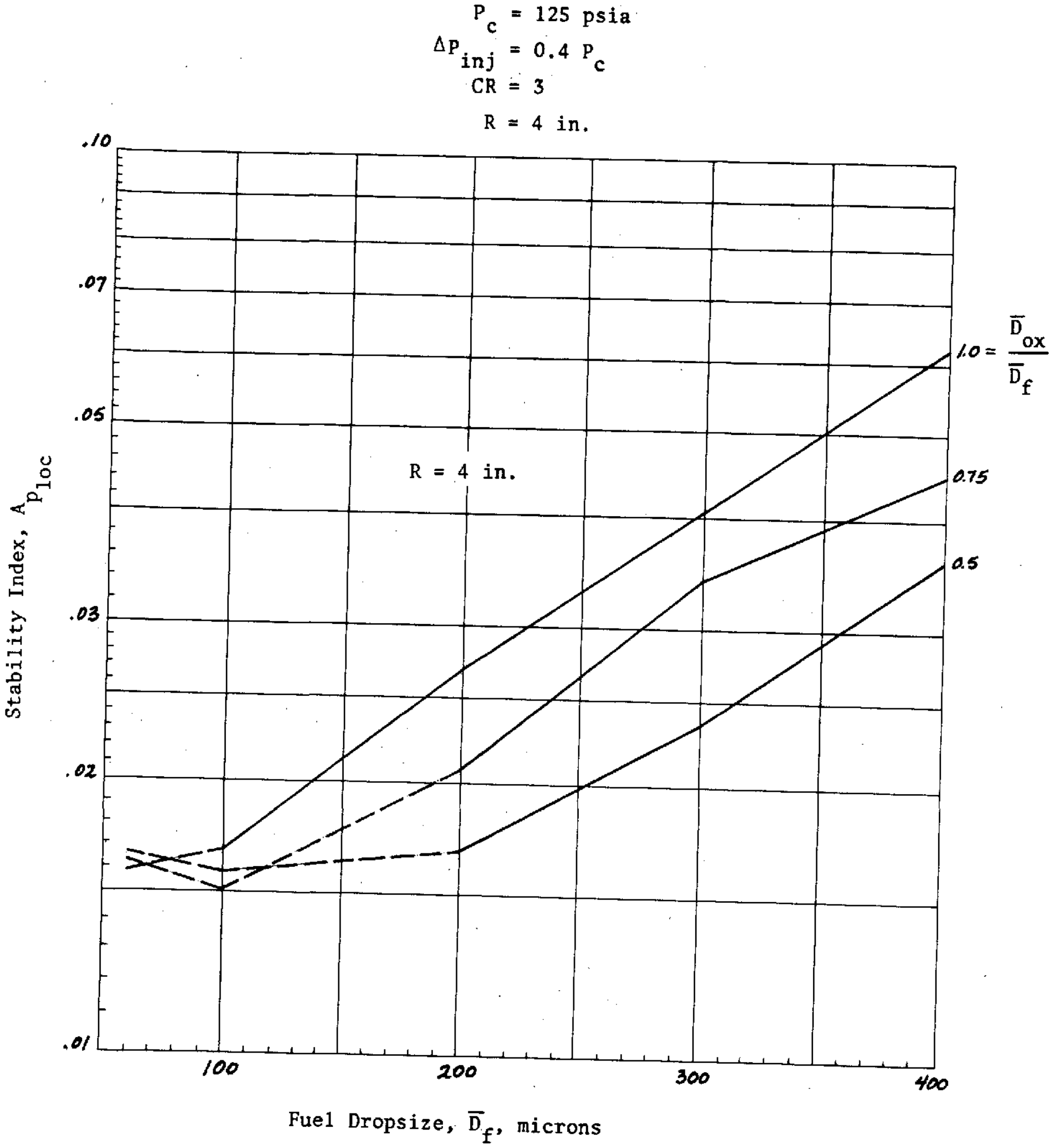

Figure B-12. Local Stability Index as a Function of Dropsize for P_c = 125 psia, ΔP_{inj} = 0.4 P_c, CR = 3

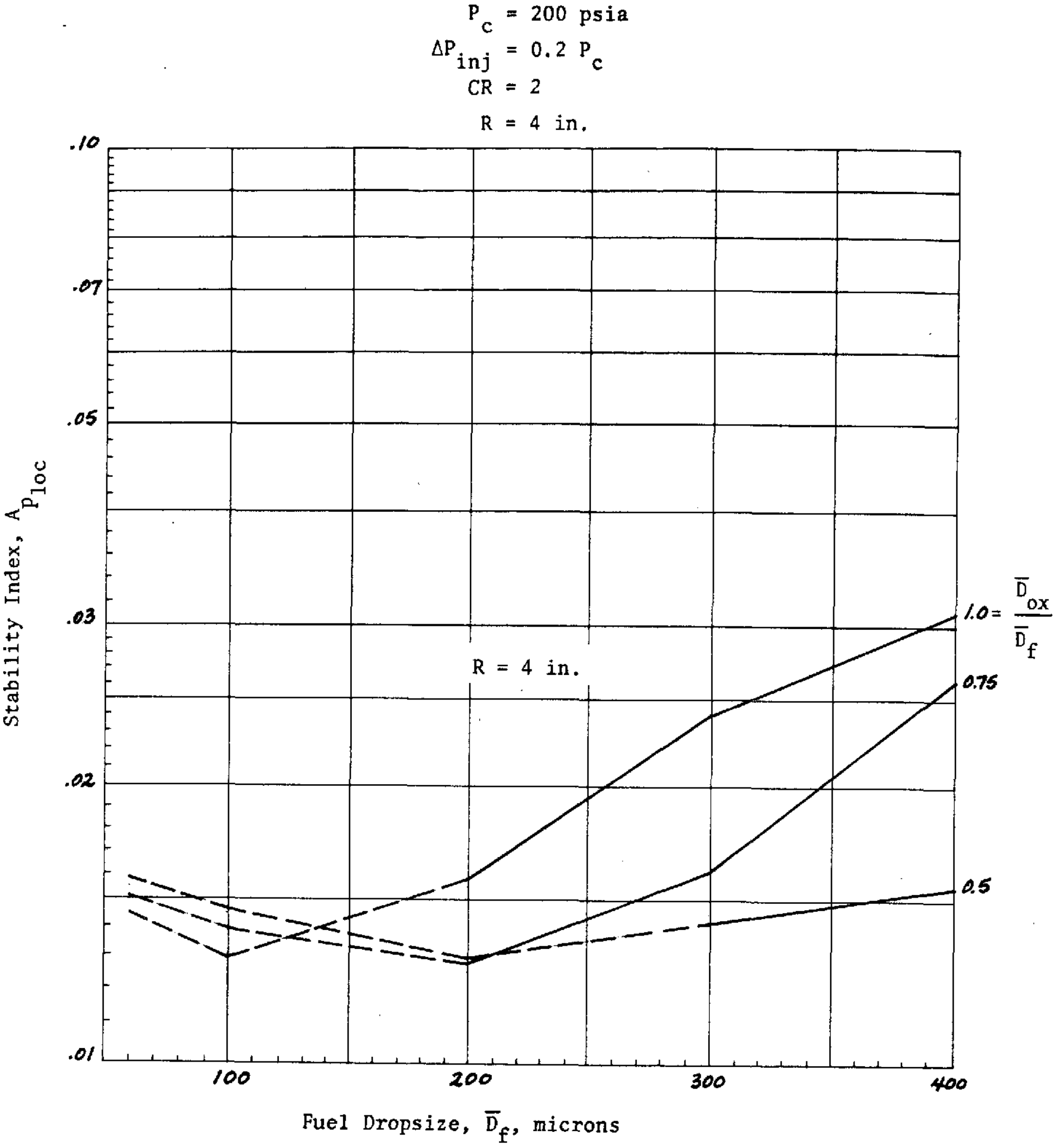

Figure B-13. Local Stability Index as a Function of Dropsize for P_c = 200 psia, ΔP_{inj} = 0.2 P_c, CR = 2

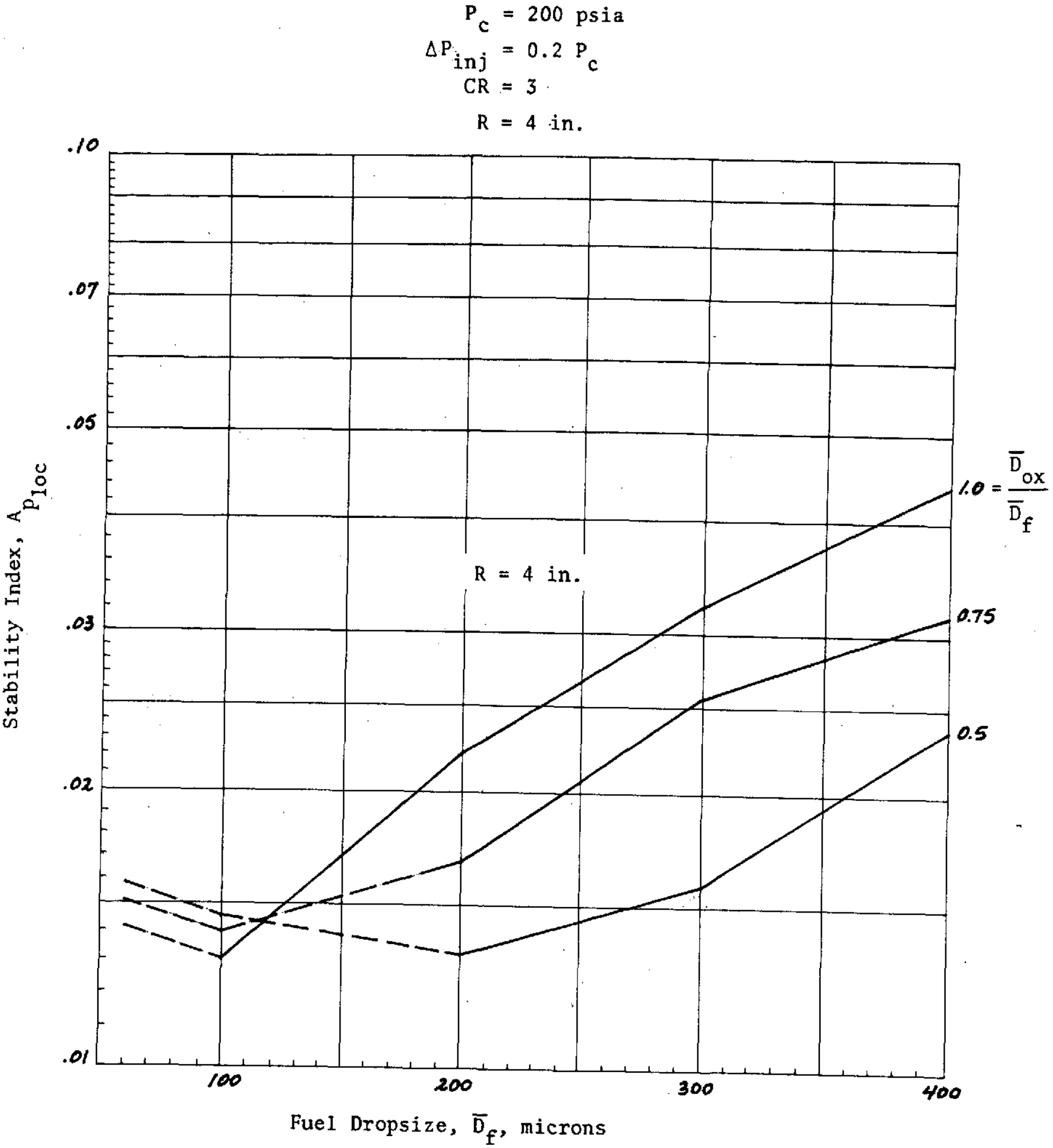

Figure B-14. Local Stability Index as a Function of Dropsize for P_c = 200 psia, ΔP_{inj} = 0.2 P_c, CR = 3

P_c = 200 psia
ΔP_{inj} = 0.4 P_c
CR = 2
R = 4 in.

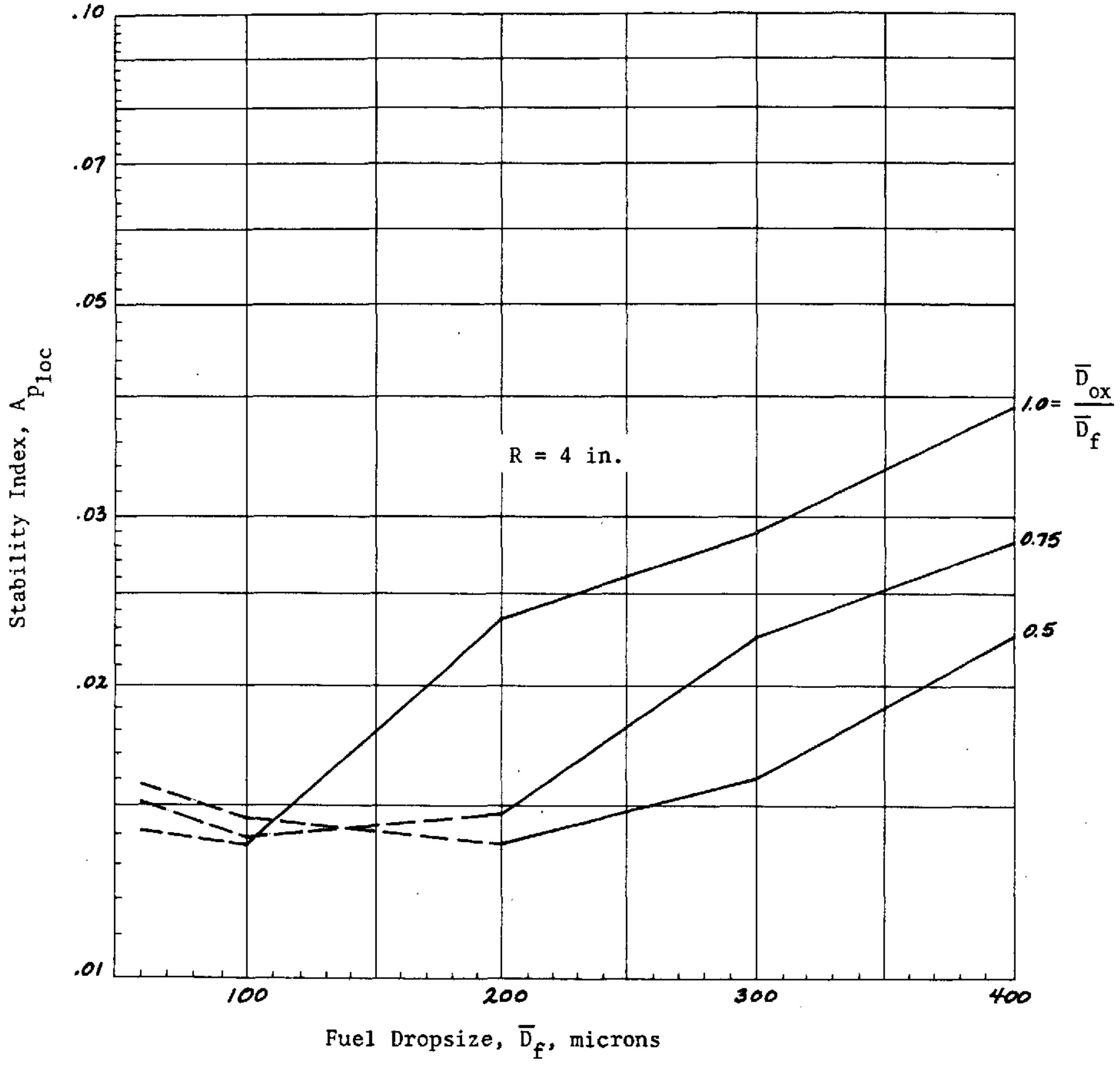

Figure B-15. Local Stability Index as a Function of Dropsize for P_c = 200 psia, ΔP_{inj} = 0.4 P_c, CR = 2

P_c = 200 psia
ΔP_{inj} = 0.4 P_c
CR = 3
R = 4 in.

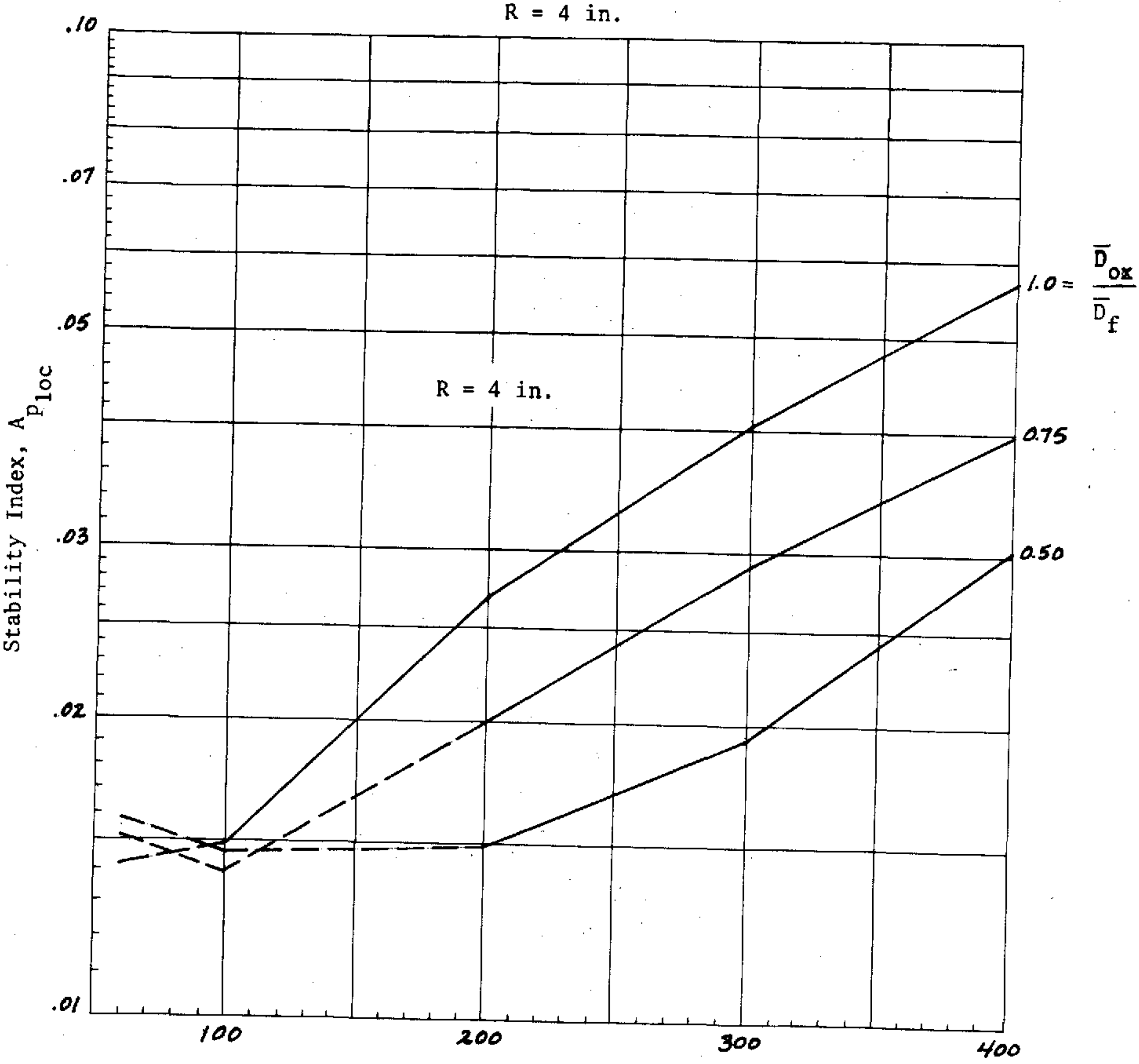

Figure B-16. Local Stability Index as a Function of Dropsize for P_c = 200 psia, ΔP_{inj} = 0.4 P_c, CR = 3

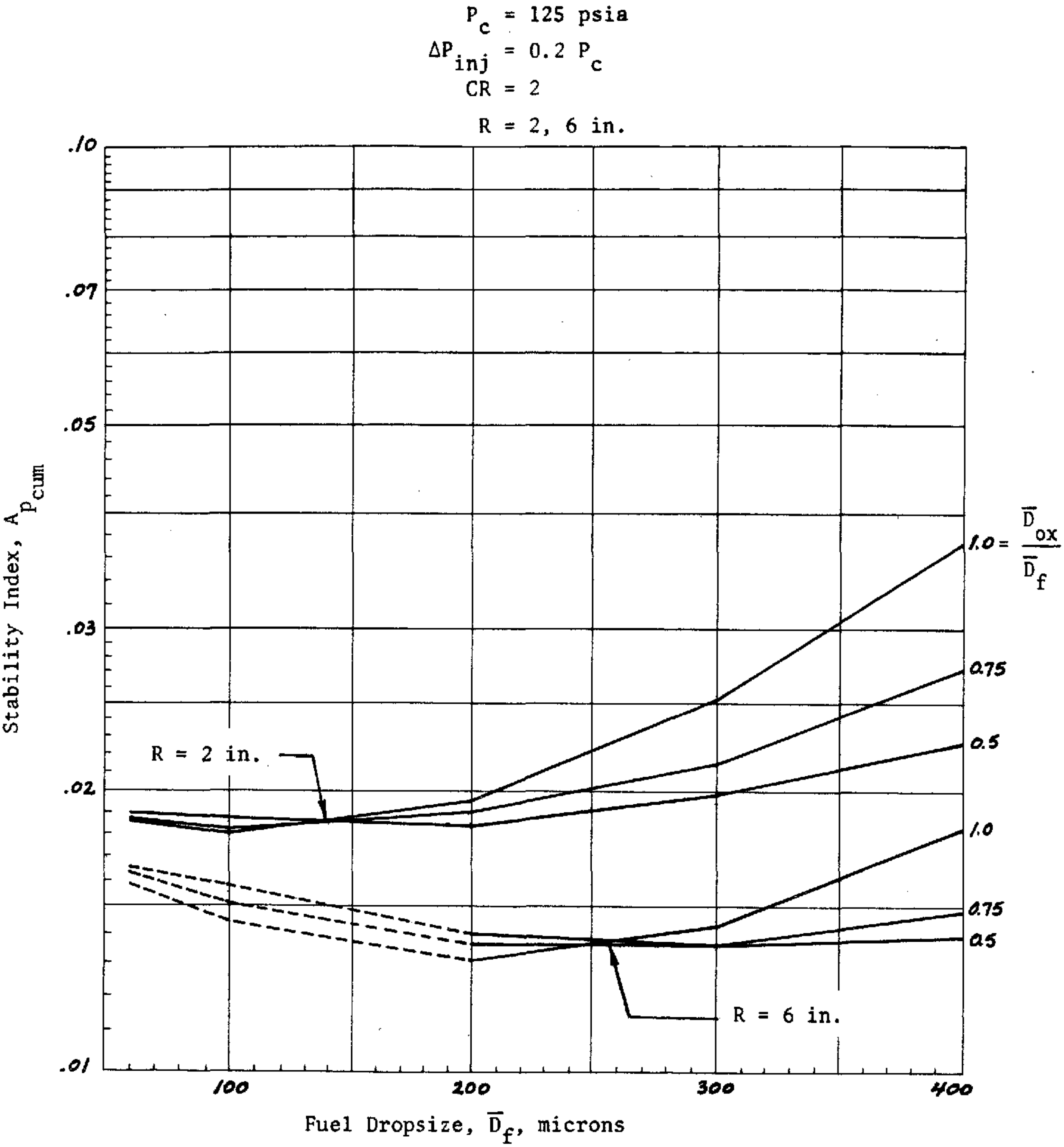

Figure B-17. Cumulative Stability Index as a Function of Dropsize for P_c = 125 psia, ΔP_{inj} = 0.2 P_c, CR = 2

P_c = 125 psia
ΔP_{inj} = 0.2 P_c
CR = 3
R = 2, 6 in.

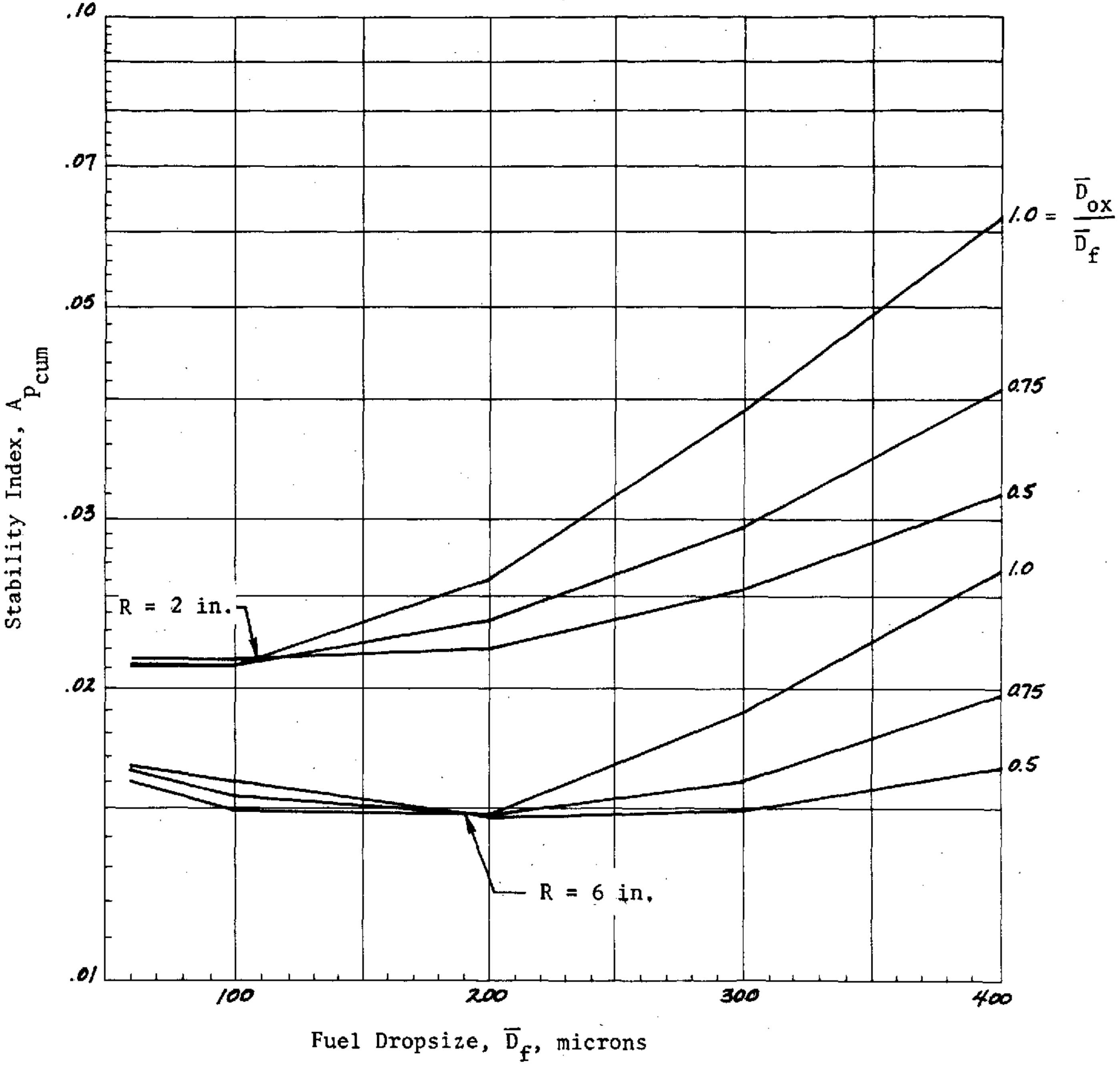

Figure B-18. Cumulative Stability Index as a Function of Dropsize for P_c = 125 psia, ΔP_{inj} = 0.2 P_c, CR = 2

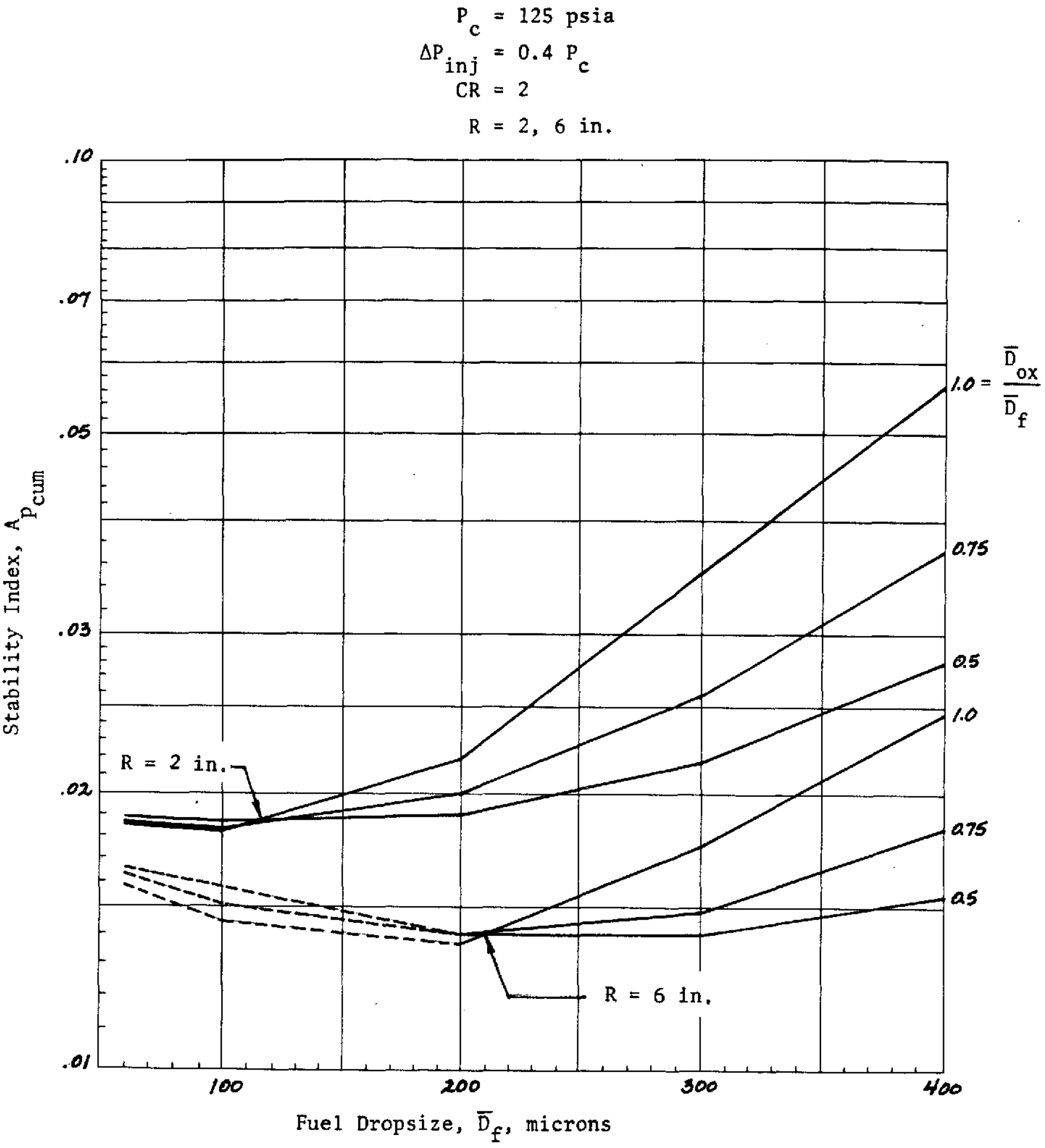

Figure B-19. Cumulative Stability Index as a Function of Dropsize for P_c = 125 psia, ΔP_{inj} = 0.4 P_c, CR = 2

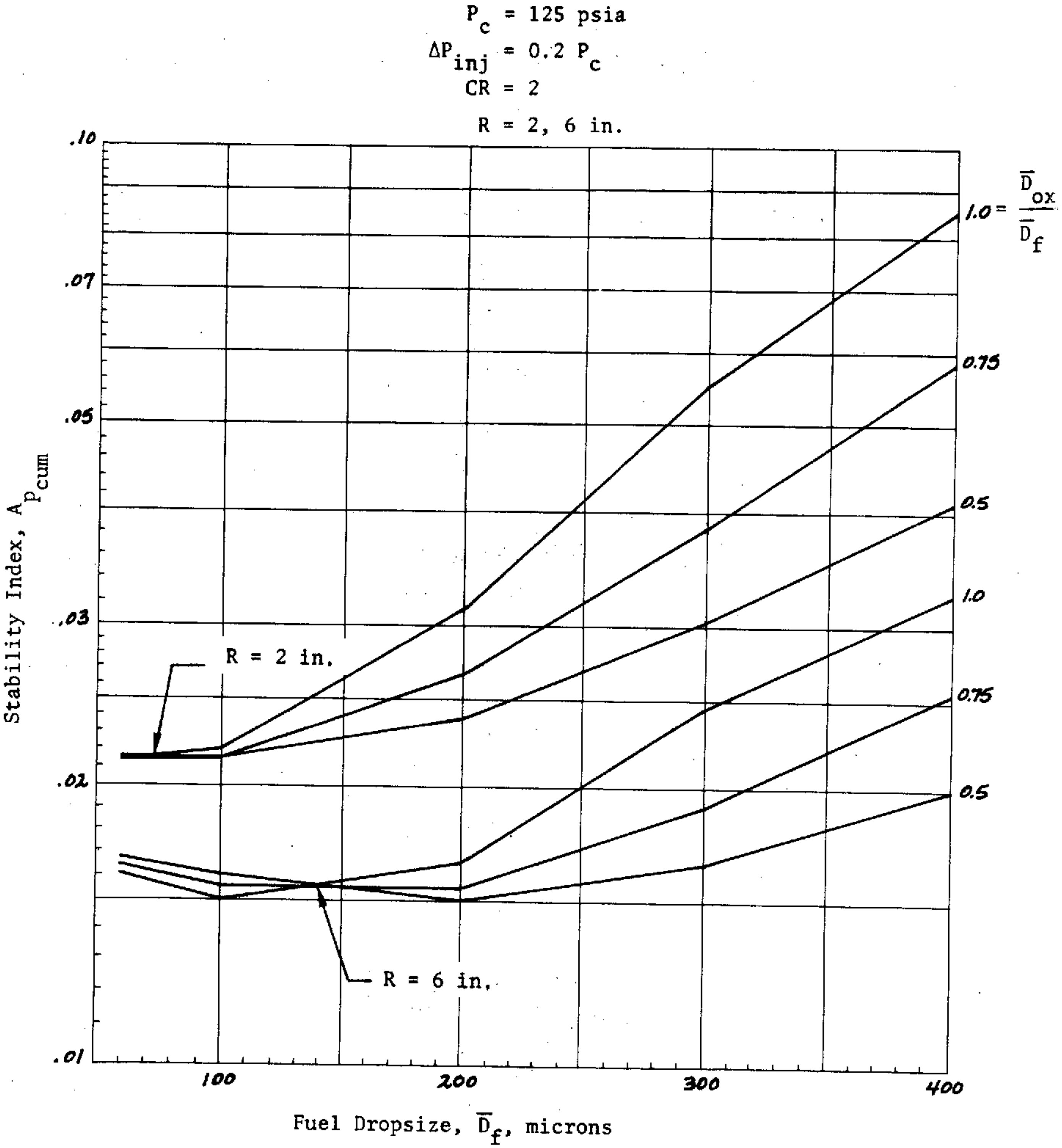

Figure B-20. Cumulative Stability Index as a Function of Dropsize for P_c = 125 psia, ΔP_{inj} = 0.2 P_c, CR = 3

$P_c = 200$ psia
$\Delta P_{inj} = 0.2\ P_c$
CR = 2
R = 2, 6 in.

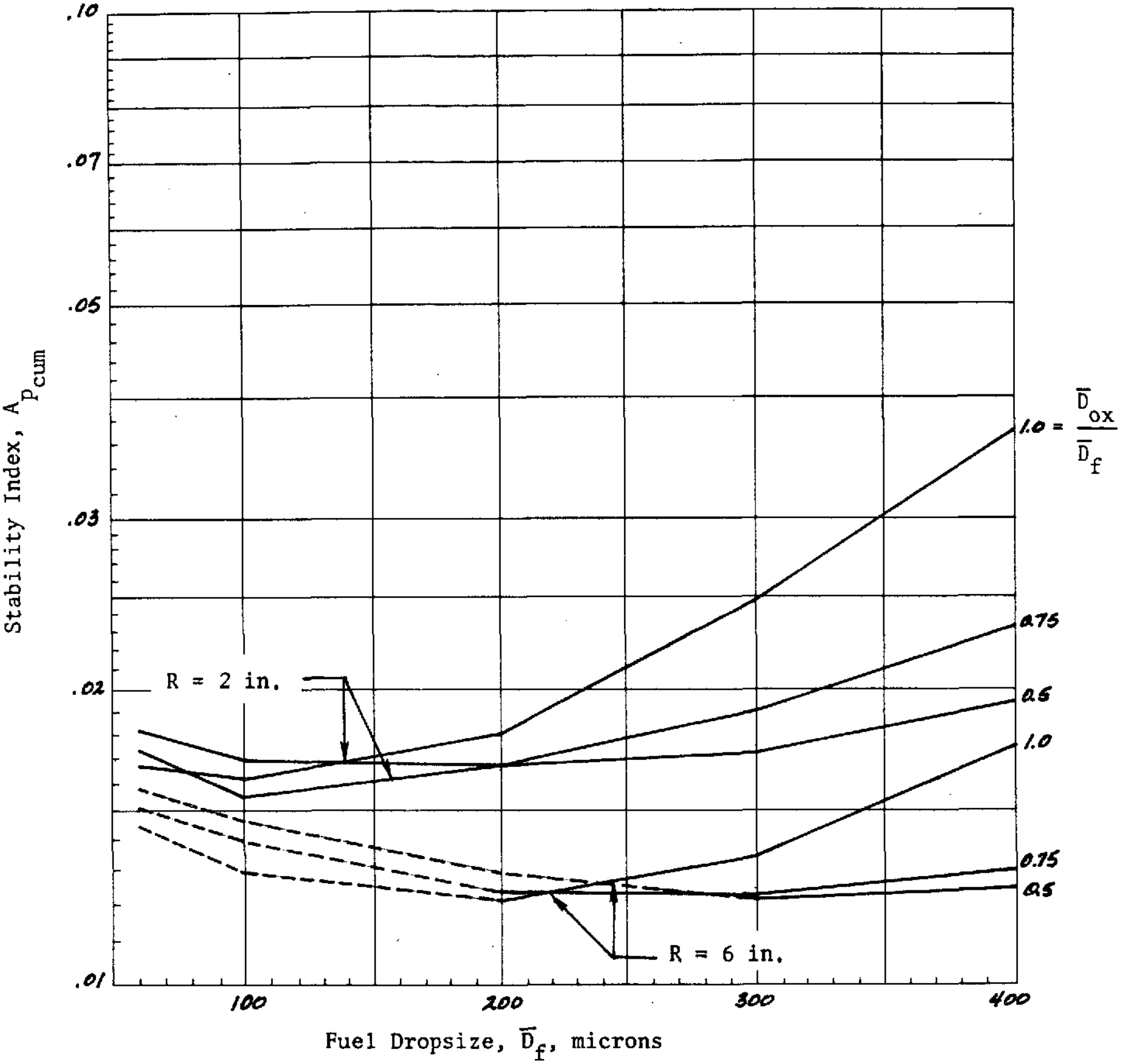

Figure B-21. Cumulative Stability Index as a Function of Dropsize for $P_c = 200$ psia, $\Delta P_{inj} = 0.2\ P_c$, CR = 2

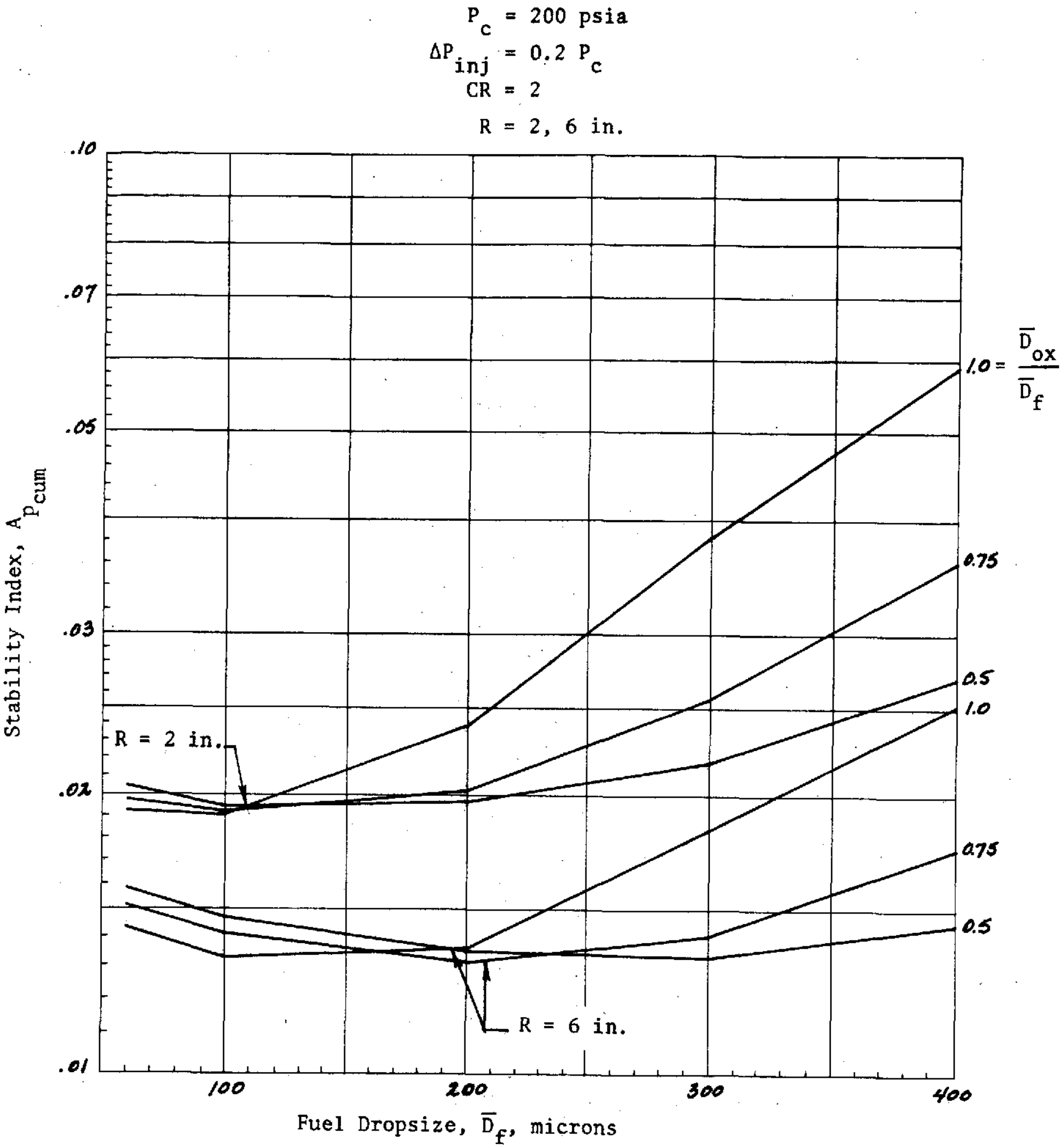

Figure B-22. Cumulative Stability Index as a Function of Dropsize for P_c = 200 psia, ΔP_{inj} = 0.2 P_c, CR = 3

P_c = 200 psia
ΔP_{inj} = 0.4 P_c
CR = 2
R = 2, 6 in.

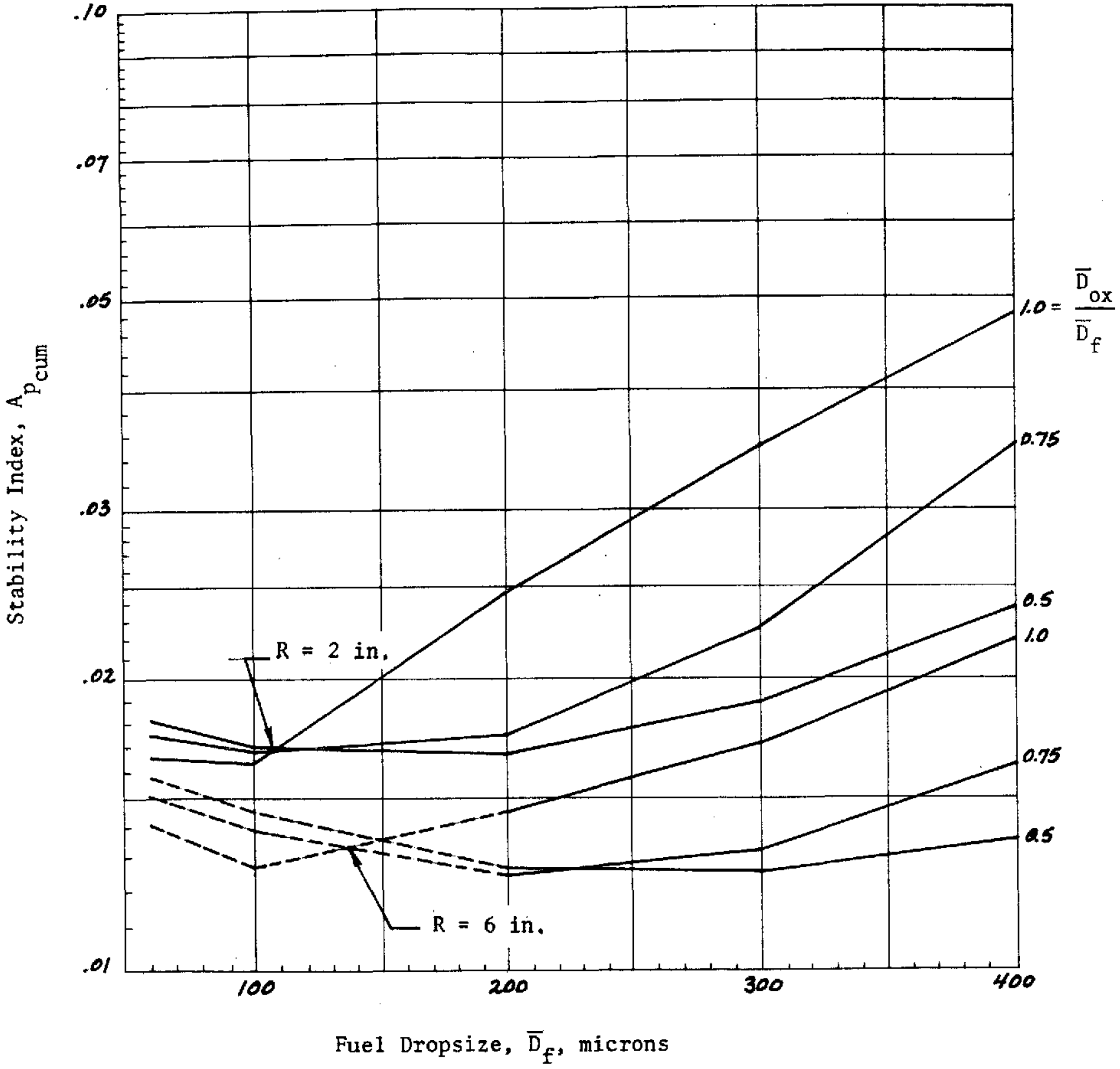

Figure B-23. Cumulative Stability Index as a Function of Dropsize for P_c = 200 psia, ΔP_{inj} = 0.4 P_c, CR = 2

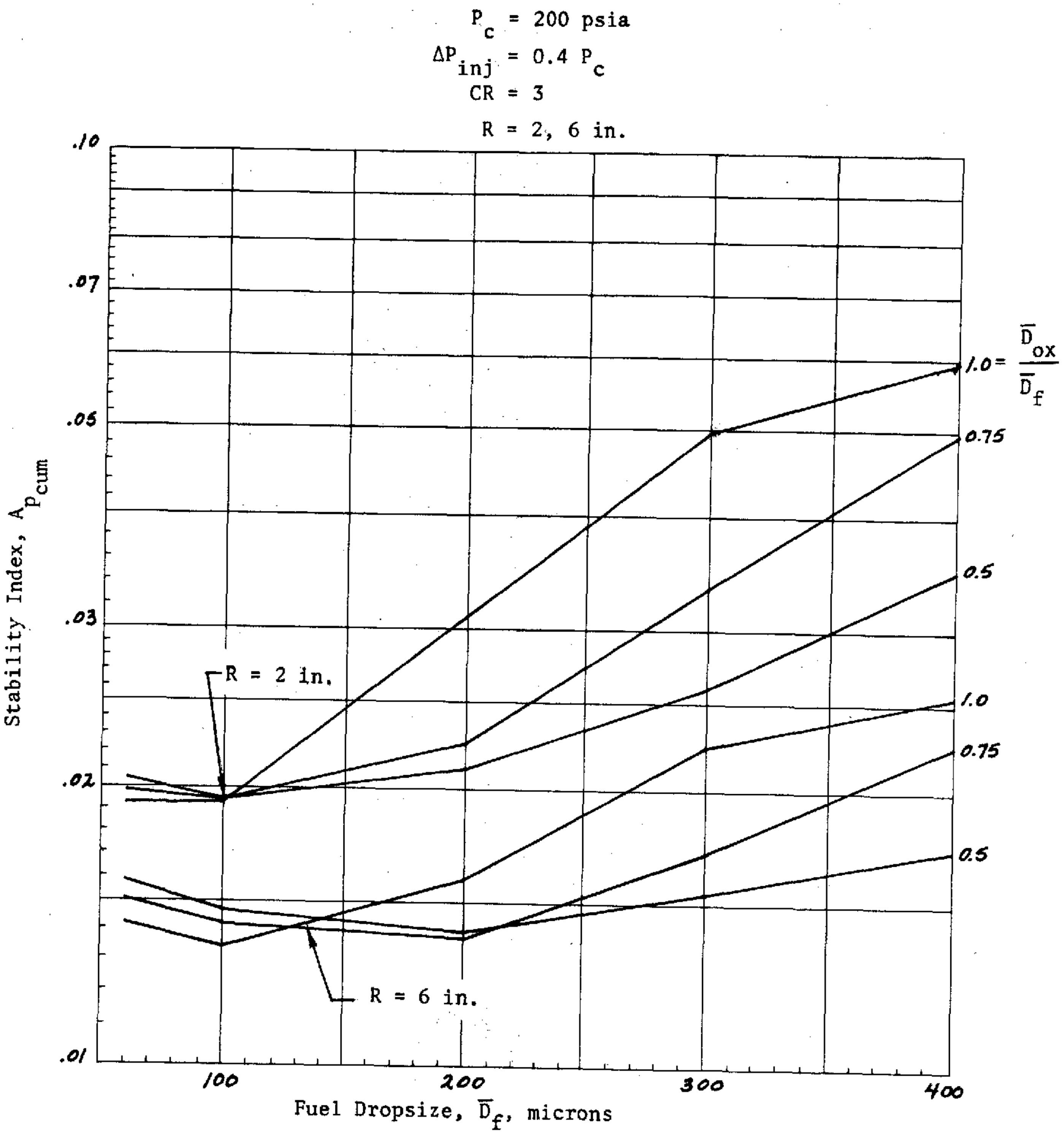

Figure B-24. Cumulative Stability Index as a Function of Dropsize for P_c = 200 psia, ΔP_{inj} = 0.4 P_c, CR = 3

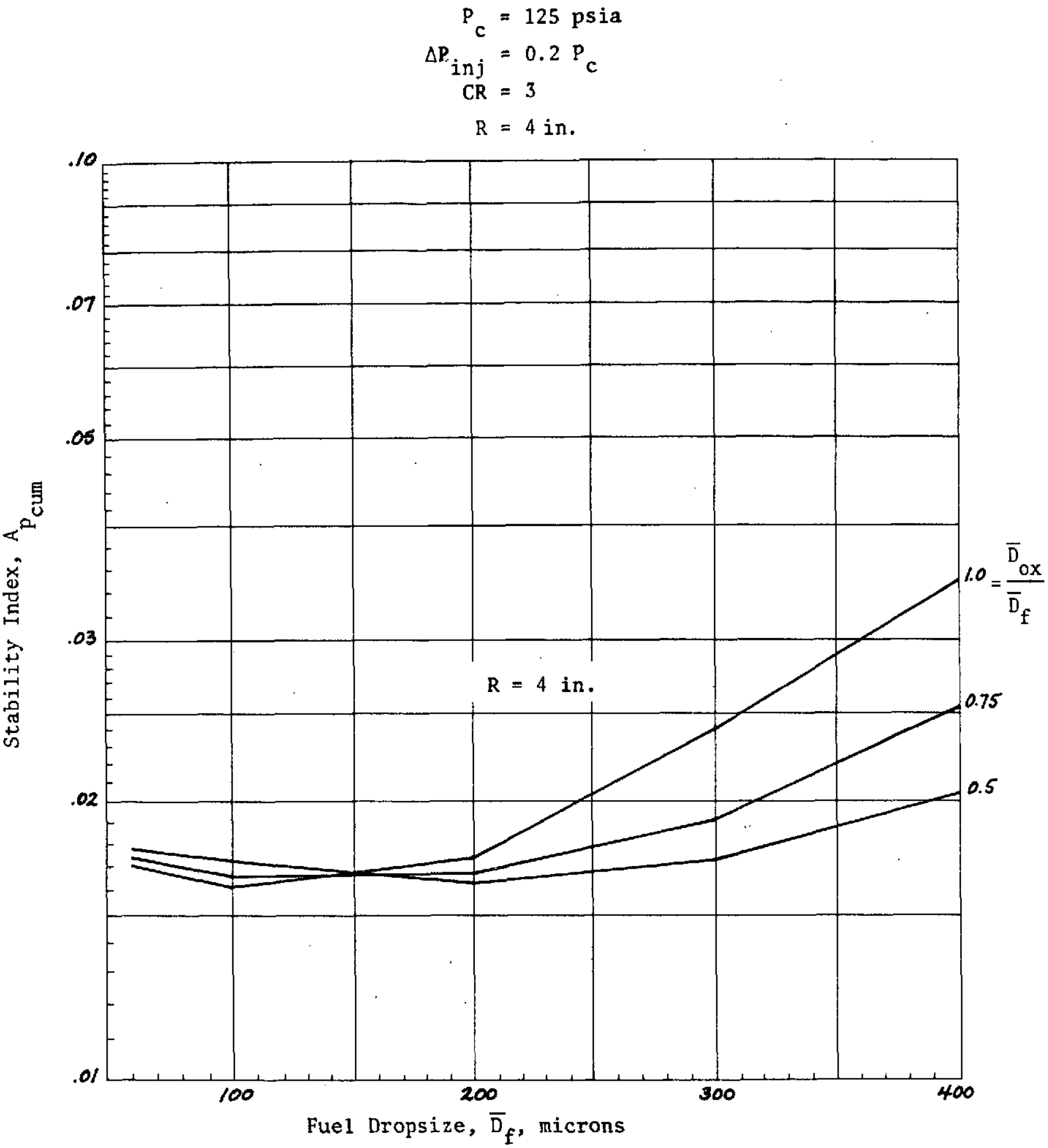

Figure B-25. Cumulative Stability Index as a Function of Dropsize for P_c = 125 psia, ΔP_{inj} = 0.2 P_c, CR = 3

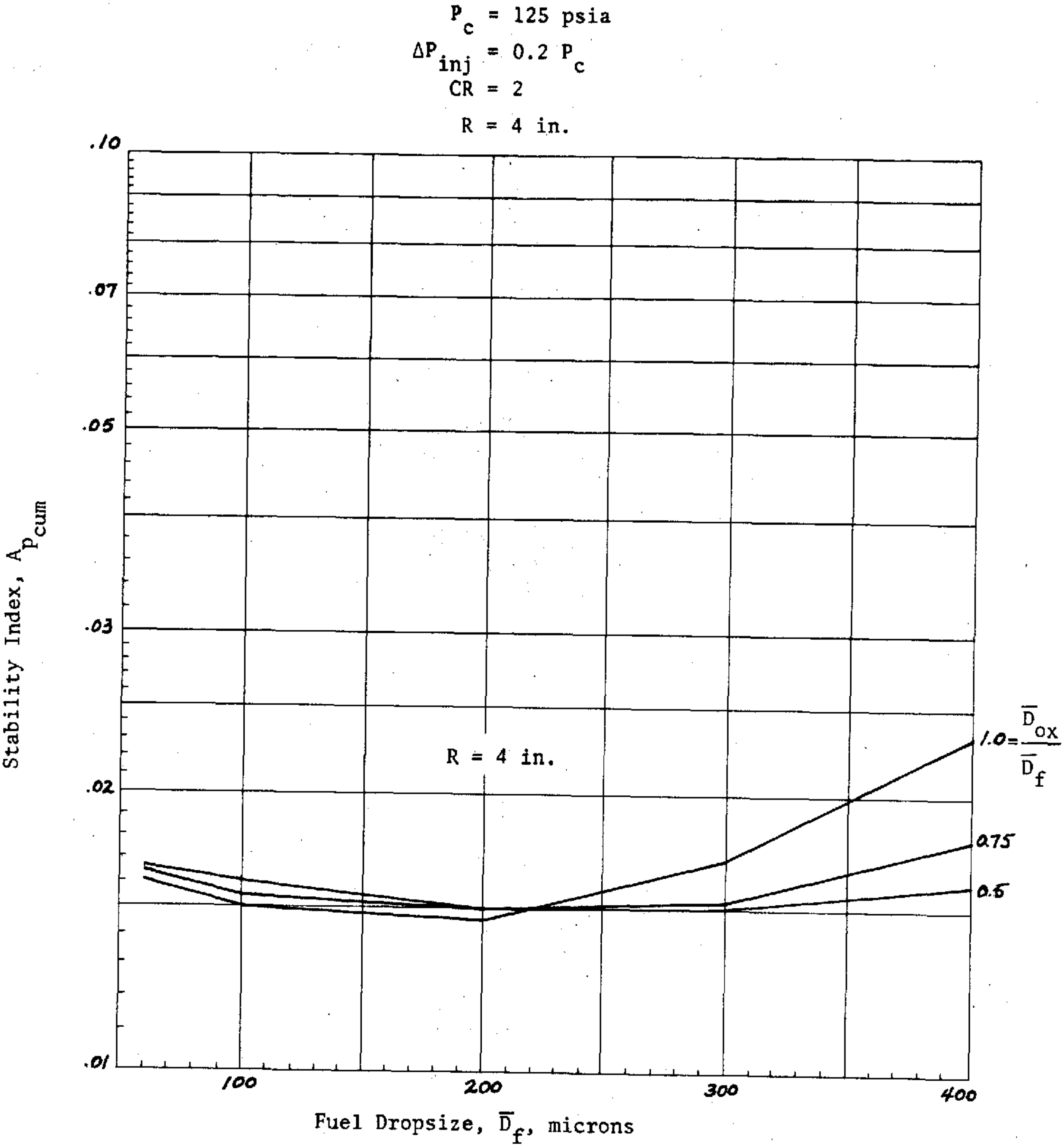

Figure B-26. Cumulative Stability Index as a Function of Dropsize for P_c = 125 psia, ΔP_{inj} = 0.2 P_c, CR = 2

P_c = 125 psia
ΔP_{inj} = 0.4 P_c
CR = 2
R = 4 in.

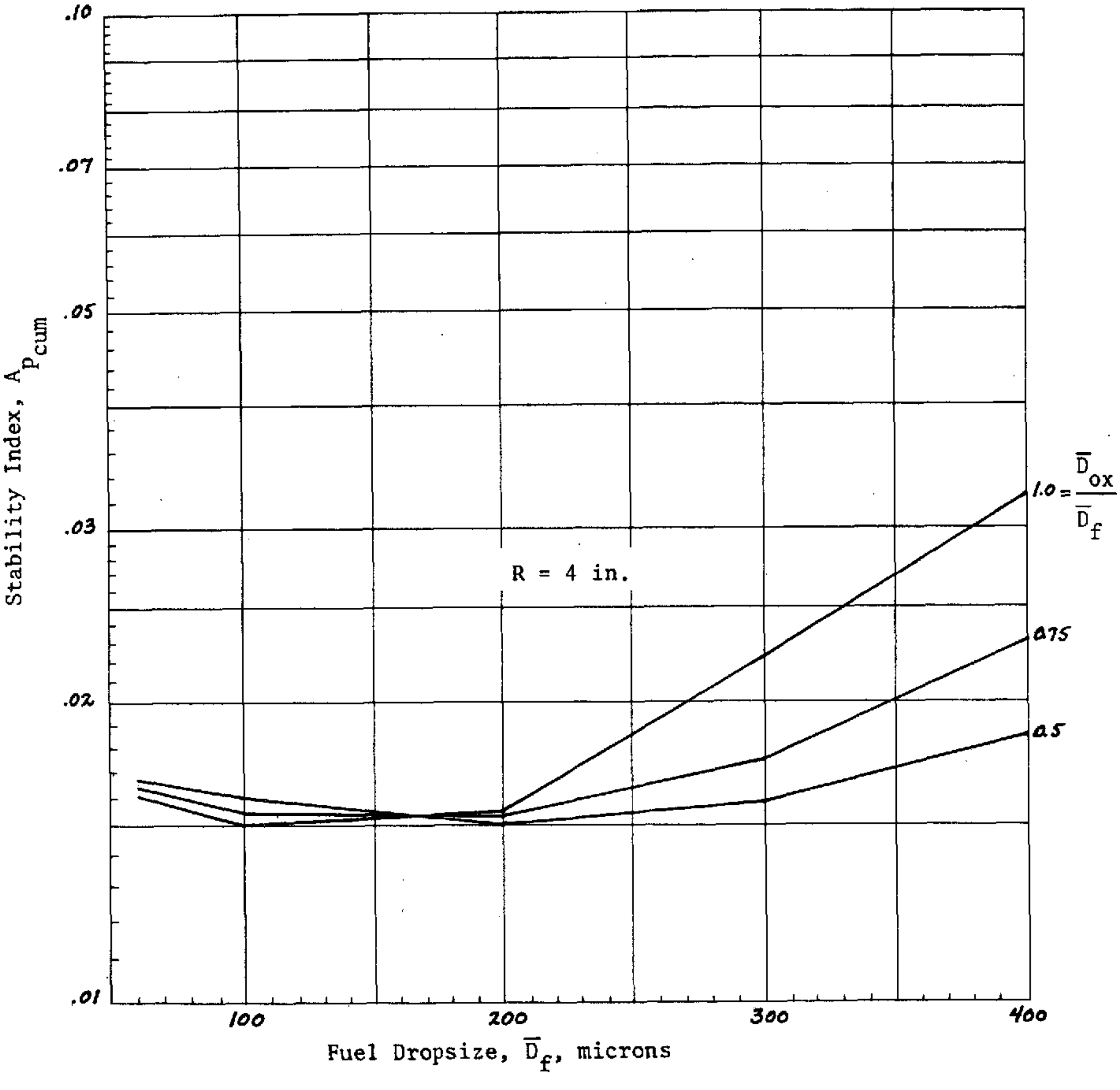

Figure B-27. Cumulative Stability Index as a Function of Dropsize for P_c = 125 psia, ΔP_{inj} = 0.4 P_c, CR = 2

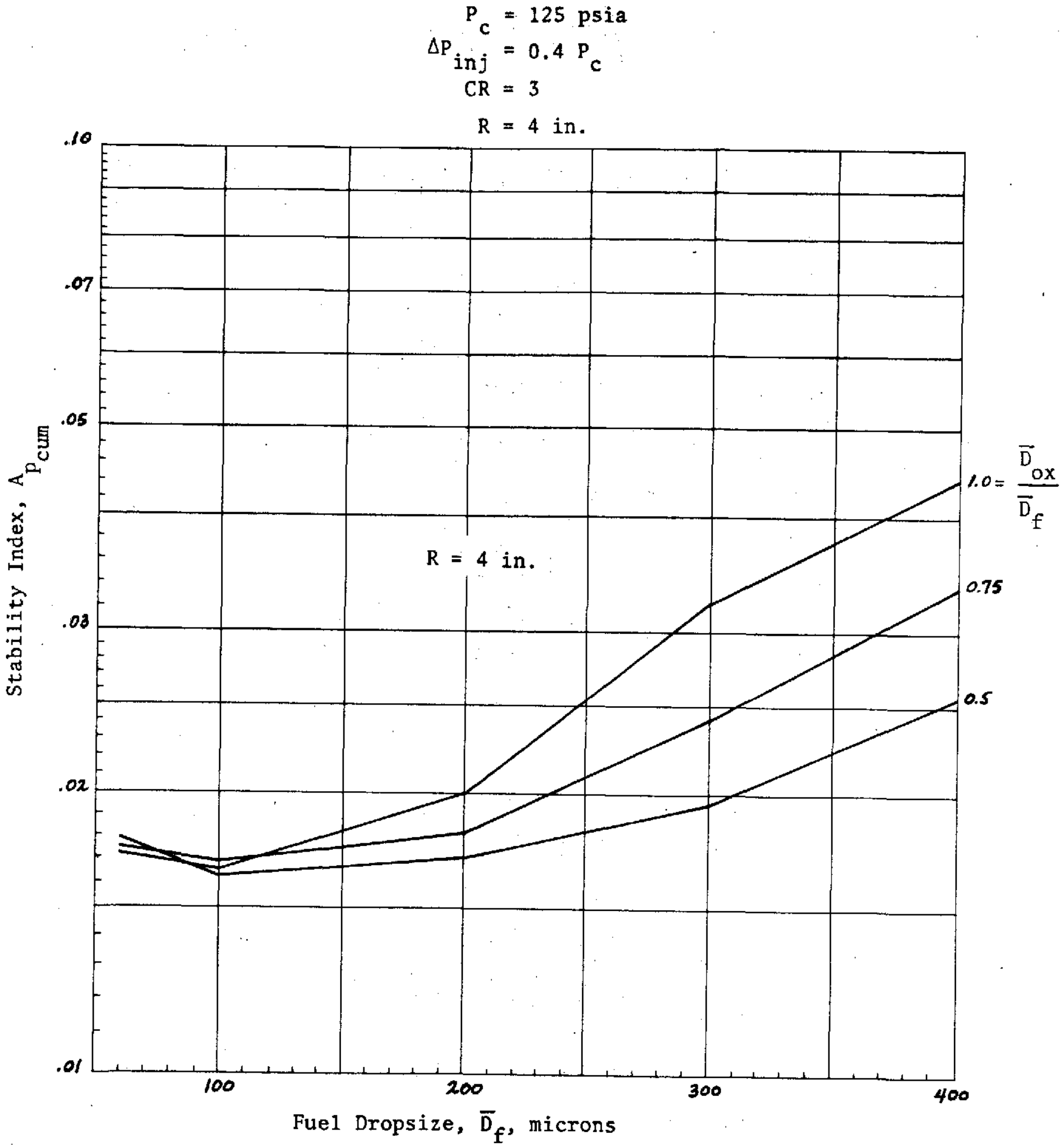

Figure B-28. Cumulative Stability Index as a Function of Dropsize for P_c = 125 psia, ΔP_{inj} = 0.4 P_c, CR = 3

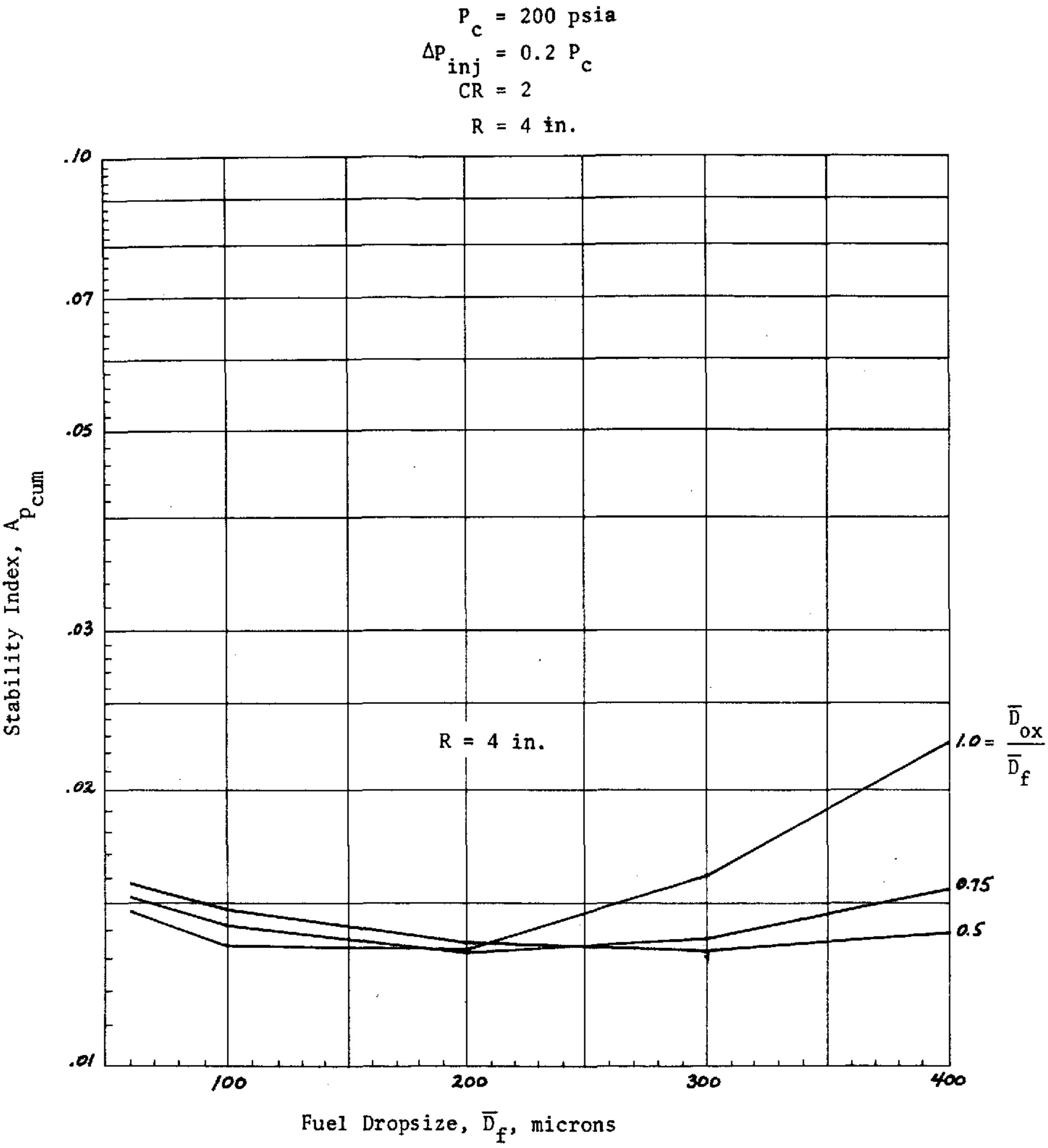

Figure B-29. Cumulative Stability Index as a Function of Dropsize for P_c = 200 psia, ΔP_{inj} = 0.2 P_c, CR = 2

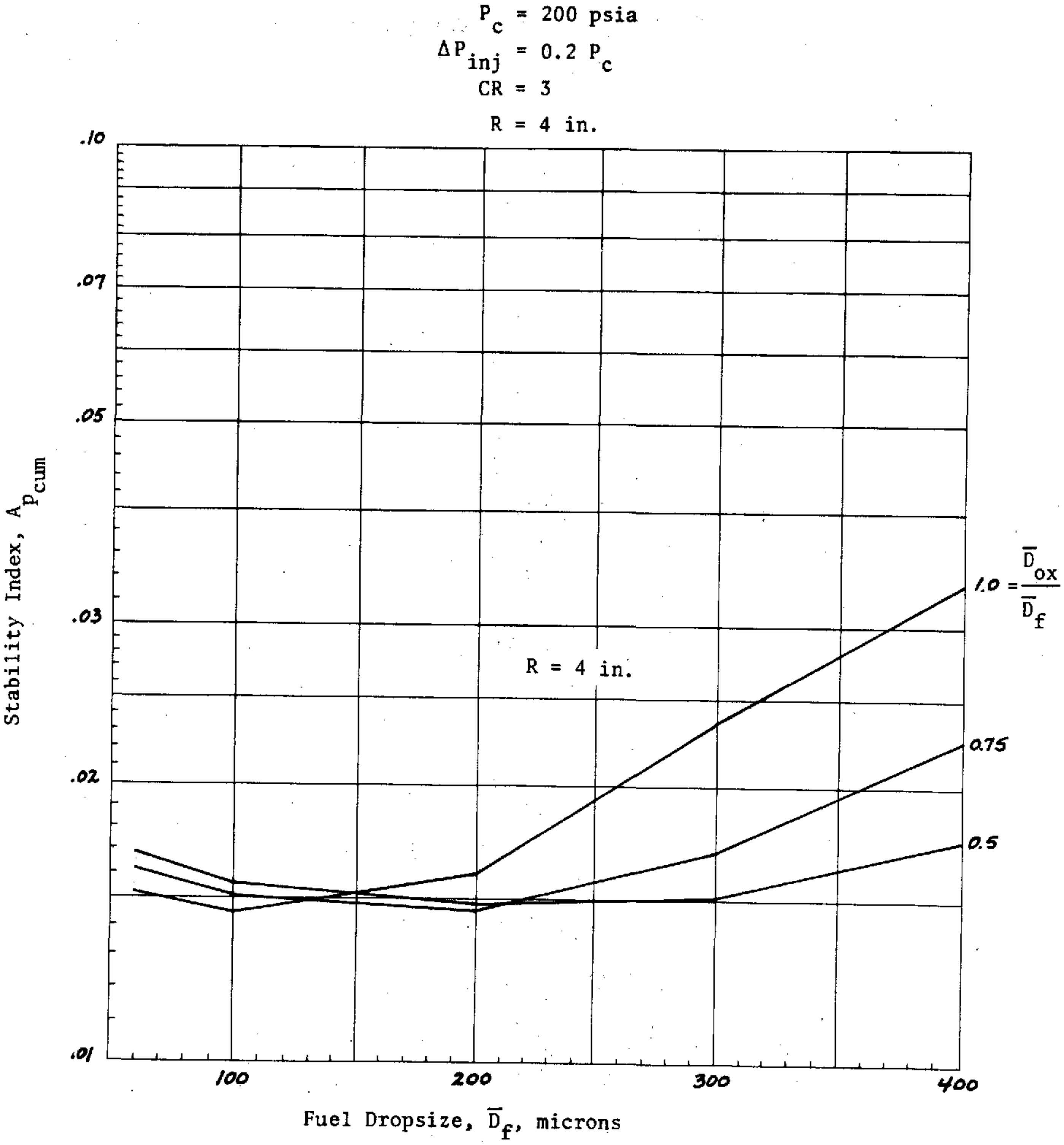

Figure B-30. Cumulative Stability Index as a Function of Dropsize for P_c = 200, ΔP_{inj} = 0.2 P_c, CR = 3

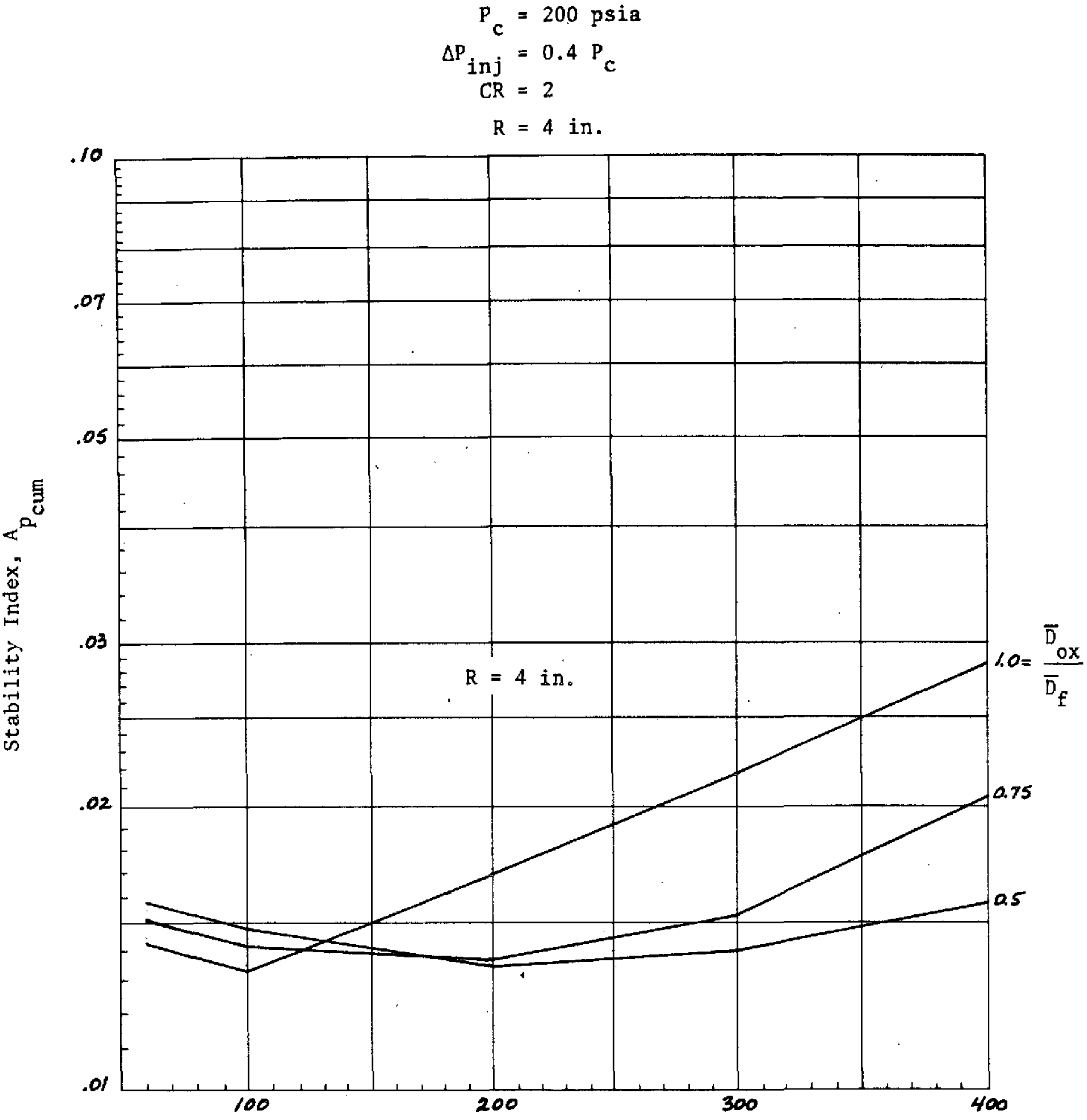

Figure B-31. Cumulative Stability Index as a Function of Dropsize for P_c = 200 psia, ΔP_{inj} = 0.4 P_c, CR = 2

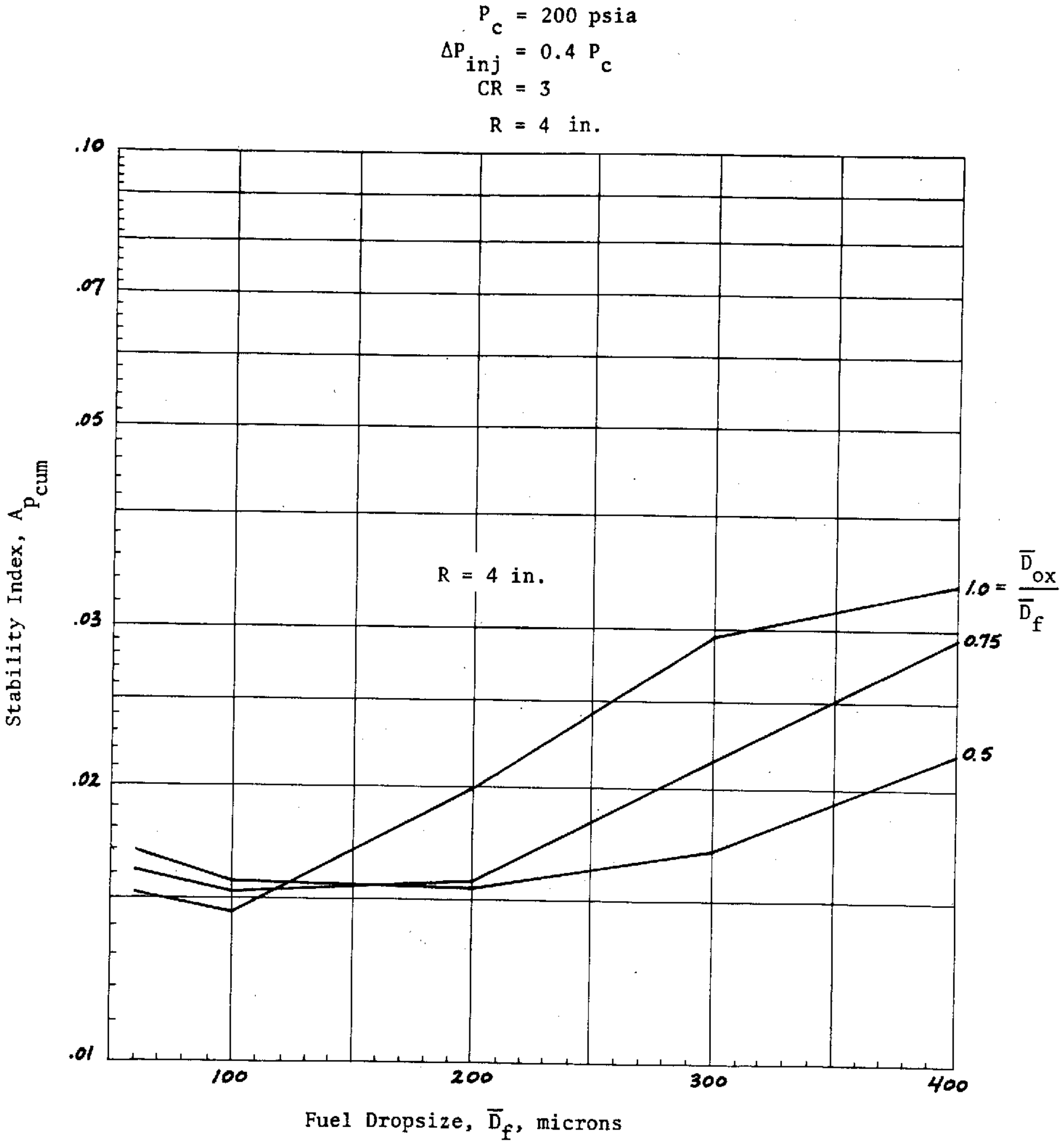

Figure B-32. Cumulative Stability Index as a Function of Dropsize for P_c = 200 psia, ΔP_{inj} = 0.4 P_c, CR = 3